THERMAL TRANSPORT AND THERMAL-MAGNETIC BREAKDOWN IN SUPERCONDUCTING CAVITIES MADE OF HIGH THERMAL CONDUCTIVITY NIOBIUM

A Thesis

Presented to the Faculty of the Graduate School

of Cornell University

in Partial Fulfillment of the Requirement for the Degree of

Doctor of Philosophy

by

Kathleen Rempel Krafft

January 1983

THERMAL TRANSPORT AND THERMAL-MAGNETIC BREAKDOWN IN SUPERCONDUCTING CAVITIES MADE OF HIGH THERMAL CONDUCTIVITY NIOBIUM

Kathleen Rempel Krafft, Ph.D.
Cornell University, 1983

Thermal-magnetic breakdown is the mechanism which ultimately limits field strengths in superconducting cavities whose performance is not affected by multipactoring or field emission. Thermal-magnetic breakdown is thought to arise from localized heating of an isolated lossy area on the cavity surface; at a certain power level the excess heating may cause the temperature near the lossy area to exceed the superconducting critical field and lead to cavity breakdown.

The objective of this investigation was to systematically investigate the two mechanisms of thermal transport in the cavity-cooling bath system: the thermal conductivity of the metal and heat transport across the metal to liquid helium interface.

For this investigation, cavities were prepared with high thermal conductivity Nb; the thermal conductivity of this niobium at 4.2K was over one hundred times higher than that of typical reactor grade niobium.

To investigate the thermal transport processes surface temperature profiles were measured when dc heater power was applied locally to a cavity surface; the experimental results were compared with the equilibrium surface temperatures calculated from functions for the thermal conductivity of the Nb and the thermal boundary resistance between superconducting Nb and liquid He I or superfluid He II; good agreement between the experimental results and the calculations was found when reasonable values for the thermal boundary resistance were used in the calculations.

The microwave performance of the Nb cavities at X-band was found to be considerably improved by the use of high thermal conductivity niobium; the high thermal conductivity Nb cavities sustained field levels over five times higher than for low thermal conductivity Nb cavities, without exhibiting breakdown.

Biographical Sketch

Kathleen Rempel Krafft was born in May 1953 in Palo Alto, California, and grew up in Silicon Valley. She graduated from Awalt High School, Mountain View, California, in 1971. She received the degree of Bachelor of Arts in Physics from Carleton College in Northfield, Minnesota, in June 1975, graduating magna cum laude. While at Carleton she met Dean Blackmar Krafft, whom she married in June 1974. From September 1975 through June 1976 she was employed as an assistant engineer/assistant scientist with the Solar Energy group at Sheldahl, Inc. in Northfield, Minnesota. She entered the Graduate School at Cornell University in 1976, received the degree of Master of Science in Physics from Cornell University in 1979, and completed this thesis in 1982. She has accepted a position as a Postdoctoral Associate with the Department of Applied Physics at Cornell University to study low frequency fluctuations in solids ("1/f" noise).

Acknowledgements

This investigation was made possible with the support of the entire Superconducting RF (SRF) group and the technical staff of the Laboratory of Nuclear Studies (LNS), as well as several visitors who participated in the SRF program; they were always available to help with experimental problems and provide moral support. I sincerely appreciate the help and friendship I have received from all those connected with LNS. I particularly wish to thank Hasan Padamsee and Joe Amato for sharing their expertise in low temperature physics. I also wish to thank John Brawley for sharing the keys to his toolbox; this was especially appreciated on weekends and evenings when I found that my tools had been "borrowed".

I am deeply grateful to my thesis advisor, Maury Tigner, for his guidance and unfailing support during the course of this project; he extensively reviewed the thesis, in several versions, and has made numerous valuable editorial suggestions. I also wish to thank Professors Silsbee and Ambegaokar for serving on my thesis committee, and for the interest they have shown in my work.

The superb job Velma Ray did typing this thesis demonstrates that her reputation as typist extraordinaire is well-deserved. I would also like to thank the LNS drafting room for preparing all of the figures that appear in this thesis.

At a more personal level, I wish to thank Patti, Sparks, and Jim and Loren Archer for their friendships of many years.

My parents, Robert and Janie Rempel, and my in-laws, Sesaly and Frederic Krafft, have strongly supported my desire for a career as a professional physicist. My father in particular, by instructing me in skiing, camping and rock climbing, has taught me confidence and determination.

Finally, I wish to thank my husband Dean for his love and support, as well as for being in charge of vacations, movies, electric blankets and other forms of decadence while we were both in graduate school.

This research was supported by the National Science Foundation.

Table of Contents

Table of Contents

List of Tables

List of Figures

List of Figures (continued)

List of Figures (continued)

Chapter 1

INTRODUCTION

1.1 RF Superconductivity and Objectives of This Investigation

Superconducting cavities are of practical interest because very little microwave power is required to sustain electromagnetic fields in such a resonant cavity. The ultimate goal of much of the research in the field is to routinely achieve the maximum field levels in a cavity, as determined by the superconducting critical fields. The microwave performance of low frequency superconducting cavities (<2 GHz) is limited by electron loading of the cavity. High frequency superconducting cavities (>4GHz) are not affected by electron loading; the maximum field level is determined by the threshold for thermal-magnetic breakdown of the cavity.

Thermal-magnetic breakdown is thought to arise from localized heating of an isolated lossy area on the cavity surface; at a certain power level a local temperature rise may result in the rapid growth of the lossy area and cause a macroscopic region of the cavity surface to become normal conducting. This temperature rise is caused by the interplay of the heat generating processes and the mechanisms that transport heat away from the lossy area or "defect".

The objective of this investigation was to systematically study the two mechanisms of thermal transport in the cavity-cooling bath system: the thermal conductivity of the metal and heat conduction across the metal to liquid helium interface.

1.2 Results and Achievements

The main achievement of this investigation was the experimental verification of a theoretical model of the thermal transport processes in the cavity-cooling bath system. In addition, theoretical calculations indicated that increasing the thermal conductivity of the Nb should raise the threshold of thermal-magnetic breakdown: this was also demonstrated experimentally.

This particular investigation was prompted by the examination of the numerous published results for the low temperature thermal conductivity of Nb in the normal and superconducting states. In particular, the magnitude of the low temperature thermal conductivity of Nb was found to correlate with the sample purity; as will be reported in this thesis, the dependence of the low temperature thermal conductivity of Nb upon the sample purity and temperature may be explained in terms of only a few physical mechanisms.

A technique was developed for the preparation of high purity Nb cavities at X-band (9GHz). The cavities were made of electrodeposited Nb, which has a very low Ta impurity concentration; the Nb was subsequently outgassed at 1900-2200C in a vacuum of 1×10^{-9} torr to reduce the concentration of interstitial impurities below 10 parts per million (atomic). The thermal conductivity of this Nb was in good agreement with expectations, demonstrating that high thermal conductivity Nb may be prepared in a controlled fashion.

Thermal transport in the high thermal conductivity cavities was investigated by measuring the temperatures along a cavity surface with a localized heat source located on the surface. The validity of the

theoretical model for thermal transport in superconducting cavities was demonstrated with these experiments: the theoretical calculations were found to be in good agreement with experiment when reasonable values for the Nb to liquid helium thermal boundary resistance were used in the calculations.

The microwave performance of the Nb cavities at X-band was found to be considerably improved by the use of high thermal conductivity Nb. An unannealed Nb cavity exhibited breakdown at a surface magnetic field below 100 Oersteds; calculations with the theoretical model demonstrated that the low thermal conductivity of this Nb caused large temperature gradients near a defect which resulted in breakdown. The outgassed Nb cavities sustained a peak magnetic field of 500 Oersteds and did not exhibit breakdown; theoretical calculations showed that the microwave performance of the high thermal conductivity was determined by transport of heat across the entire metal-liquid helium surface.

In summary, the theoretical model for thermal transport in the cavity-cooling bath system was found to describe the experimental system. In addition, increasing the thermal conductivity of the Nb was found to raise the peak magnetic field that may be sustained in high frequency superconducting cavities; high thermal conductivity Nb does indeed stabilize the cavity against localized heating at defects on the cavity surface.

1.3 Overview of the Thesis

In Chapter 2 surface resistance and power dissipation in the walls of a resonant cavity will be discussed, as well as the theoretical

model for thermal transport in superconducting cavities. The physics underlying the low temperature thermal conductivity of Nb will be discussed in Chapter 3; Chapter 3 also contains a complete review of the numerous published results since such a review had not previously been performed. The thermal boundary resistance between a metal and liquid He I or superfluid He II will be discussed in Chapter 4. The preparation and characterization of the high thermal conductivity Nb cavities used in this investigation will be described in Chapter 5. In Chapter 6, the results and analysis of an experimental investigation of thermal transport in high thermal conductivity Nb cavities will be presented. Finally, in Chapter 7 the results and analysis of microwave measurements on the high thermal conductivity Nb cavities and several low thermal conductivity Nb cavities will be discussed. Chapter 8 summarizes the results of this investigation and discusses the implications for future research.

Chapter 2

RF SUPERCONDUCTIVITY AND MODELS FOR THERMAL TRANSPORT IN SUPERCONDUCTING CAVITIES

2.1 Surface Resistance in the Normal and Superconducting States

The concept of surface resistance is used to describe energy dissipation within the walls of a resonant cavity for metals in both the normal and superconducting states [2.1-2.3]. The power dissipation occurs within a thin layer near the metal surface because the electromagnetic fields are attenuated exponentially with distance from the surface. The time-averaged power dissipation per unit area of surface is given by the formula

$$\frac{dP_{loss}}{dA} = \frac{1}{2} R_s H_t^2$$

where R_s is the surface resistance and H_t is the tangential magnetic field at the metal surface.

In a good conductor in the normal state the attentuation constant is given by the skin depth δ. R_s is then given by [2.3]

$$R_s = \frac{1}{\sigma\delta} = \left(\frac{\omega\mu}{2\sigma}\right)^{\frac{1}{2}} \qquad \text{(MKS units)}$$

where σ is the DC electrical conductivity of the metal.

Physically, the energy dissipation arises because the electrons suffer collisions as they are driven by the penetrating electromagnetic fields. In the free electron model for normal metals [2.4] the DC electrical conductivity is expressed in terms of the number density of conduction electrons, n, and the total scattering rate for electrons, τ^{-1}, by

$$\sigma = \frac{ne^2\tau}{m} .$$

At room temperature phonons are responsible for scattering electrons; as the temperature is lowered the number of phonons decreases until only point defects in the metal scatter electrons. Consequently, the surface resistance of normal metals is expected to decrease as the temperature is lowered from room temperature. However, when the electron mean free path becomes comparable to the skin depth then the surface resistance of normal metals becomes independent of temperature, a condition known as the "anomalous" skin effect [2.2, 2.5].

Extensive reviews of RF superconductivity have been given by Pierce [2.1] and Hartwig and Passow [2.2]. The microwave surface resistance of metals in the superconducting state may be understood qualitatively in terms of the two fluid model. According to the two fluid model, when the temperature falls below the critical temperature T_c of the metal, then a fraction $n_s(T)/n$ of the total number of conduction electrons condense into Cooper pairs; n_s is zero at T_c and approaches n as the temperature falls well below T_c. The remaining conduction electrons are assumed to behave like "normal" electrons; the fraction $n_n(T)/n$ of "normal" electrons is unity at T_c and approaches zero at temperatures well below T_c. In the presence of electromagnetic fields, the Cooper pairs move cooperatively through the lattice without power dissipation; power is dissipated only by the "normal" electrons in the superconductor. The penetration depth for electromagnetic fields in a superconductor is given by the London penetration depth [2.2]

$$\lambda = \left(\frac{m}{n_s e^2 \mu_o} \right)^{\frac{1}{2}} \quad . \quad \text{(MKS units)}$$

Well below T_c this superconducting penetration depth is much less than

the skin depth for normal conductors. The superconducting state surface resistance determined from Maxwell's equations and the London equation is given by [2.2]

$$R_s \propto \omega^2 \frac{n_n}{n_s^{3/2}} .$$

The superconducting state surface resistance is expected to drop quickly towards zero as the temperature falls well below T_c because n_s increases rapidly while n_n decreases rapidly.

A detailed understanding of the temperature and frequency dependence of the superconducting state surface resistance requires the use of the microscopic theory of superconductivity developed by Bardeen, Cooper, and Schrieffer (BCS) [2.6]. The theory for the BCS surface resistance was developed by Mattis and Bardeen [2.5]; the integral expressions given by Mattis and Bardeen have been evaluated by Turneaure and Weissman [2.7] and by Halbritter [2.8]. For $\hbar\omega$ well below the energy gap $\Delta(T)$ and T below $T_c/2$ then at 9GHz R_s was found to depend upon frequency and temperature according to the relationship

$$R_s(\omega,T) \approx \frac{\omega^{1.7}}{T} \exp^{-0.91\Delta(T)/kT} .$$

The exponent of ω and the factor 0.91 multiplying $\Delta(T)$ vary by about 10% for frequencies between 0.1 and 20 GHz. The exponential term in this expression gives the number density of quasiparticles or "normal electrons" in the superconductor in the BCS formulation.

This approximate expression is in good agreement with the measured surface resistance for Nb below $T_c/2$ (see Figure 7.10 and References [2.7-2.11]). Typical values for the surface resistance of Nb at 9GHz are as follows: in the normal state at room temperature R_s is about

10^{-1} ohms; in the superconducting state R_s is about 10^{-5} ohms at 4.2K and about 10^{-6} ohms at 2.5K.

Experiments show that the superconducting state surface resistance does not continue to fall exponentially as the temperature is lowered. The measured surface resistance always approaches some temperature and frequency indepenedent value due to residual, non-BCS losses. The total surface resistance in the superconducting state is usually described by the equation

$$R_s(T) \approx \frac{A}{T} \exp^{-B\Delta(T)/kT} + R_{res} ,$$

where R_{res} is the residual resistance and the constants A and B are temperature-independent. The sources of this residual resistance are thought to be chemical or morphological imperfections in the cavity surface; the residual losses may be either dielectric or ohmic in nature [2.1-2.2, 2.12-2.13]. In order to minimize the residual losses careful surface preparation, cleanliness in assembling the cavity, and ultra high vacuum techniques are essential.

The dependence of the superconducting state surface resistance upon the magnetic field is not well known. The surface resistance is expected to increase to the normal state value when the surface magnetic field approaches the critical fields for the superconductor. At fields below the critical fields the surface resistance is not expected to depend strongly upon the magnetic field, provided that $\hbar\omega$ is well below $2\Delta(T)$, the energy required to break a Cooper pair. Experimentally the surface resistance has been observed to increase at high field levels; this effect may have been caused by heating of the surface.

Niobium is generally used in superconducting cavities because of its high critical fields and high T_c. For Nb at microwave frequencies the maximum field level is expected to be about 2000 Oersteds [2.7], which is somewhat above the field level at which flux begins to penetrate the Nb.

2.2 Limitations on Cavity Performance

The peak fields observed for Nb cavities fall well below the critical fields of Nb. Four different effects are thought to limit the peak fields achievable in superconducting cavities; these are multipactoring, field emission, magnetic breakdown, and thermal-magnetic breakdown.

Multipactoring is a resonant electronic process which occurs at well-defined field levels in microwave cavities under vacuum [2.14-2.16]. Multipactoring begins when an electron strikes the cavity surface and causes a secondary electron to be emitted at low energy; the secondary electron is accelerated by the cavity fields and may return to strike the surface and generate more secondary electrons; the number of orbiting electrons will increase and "load" the cavity if the secondary electron emission coefficient is greater than one and the electrons return to their starting point in an integral number of RF periods. The field levels at which multipactoring occur scale linearly with frequency for a given cavity shape; thus multipactoring was not expected to affect the microwave performance of the high-frequency (9GHz) cavities used in this investigation [2.14].

Electrons may also limit cavity performance by means of non-resonant electronic phenomena [2.17, 2.18]. These non-resonant

phenomena are not understood in detail but are related to field emission in that above a certain threshold field level the number of electrons present in the cavity increases exponentially with increasing field [2.17]. The effects of these non-resonant electronic phenomena have been observed to decrease as the cavity frequency is increased; thus these phenomena were not expected to significantly influence the performance of X-band (9GHz) cavities.

The performance of high frequency superconducting cavities is limited by cavity breakdown. One suggestion for the cause of the breakdown is that local weak spots with low critical fields are present on the cavity surface [2.13]; the weak spot becomes normal-conducting when the magnetic field exceeds the critical field at the weak spot; the large temperature gradients in the region surrounding the normal-conducting spot may cause magnetic breakdown. Another suggestion for the cause of breakdown is excess heating at localized lossy areas on the cavity surface; as the field level is increased the temperature near the "defect" may exceed the critical temperature of the superconductor and lead to thermal-magnetic breakdown. Finally, in a defect free cavity thermal breakdown may occur, where the high power cavity performance is limited by the large temperature drop across the metal to liquid helium interface.

The experimental evidence indicates that thermal-magnetic breakdown is the effect that usually limits cavity performance at high frequencies. First, networks of thermometers placed on the outside cavity surface demonstrate that localized heating may occur at field levels well below those at which cavity breakdown occurs. Strong evidence for thermal-magnetic breakdown has been reported by Proch [2.19]; Proch made

measurements on 2-cell cavities where breakdown was observed to occur at the same location on the cavity surface in both pass-band modes of the cavities; cavity breakdown was then studied with the two modes excited simultaneously with various relative amplitudes. If the breakdown were magnetic then the sum of the field levels for each mode should be constant at breakdown, independent of the relative amplitudes of the two modes. If the breakdown were thermal in nature then the sum of the power dissipated in each mode should be constant at breakdown. The measurements by Proch for a number of 2-cell cavities at X-band and S-band (3GHz) clearly indicated that the breakdown was thermal in nature for surface magnetic field levels between 130 and 1000 Oersteds.

At frequencies below 2GHz the performance of superconducting Nb cavities is usually limited by electron loading to peak magnetic fields below 500 Oersteds (see References [2.14-2.18] or the review articles by Lengeler [2.20] or Pfister [2.21]); much current research is directed towards the design of low frequency cavities whose performance is not limited by electron loading. Superconducting Nb cavities at frequencies above 4GHz usually exhibit breakdown at magnetic field levels between 200 and 1000 Oersteds [2.22-2.30]; in a very few cases breakdown at a magnetic field level of around 1500 Oersteds has been reported [2.22, 2.24]. In order to routinely sustain peak magnetic fields at the level of the critical fields of Nb the mechanisms of heat generation and thermal transport in superconducting cavities must be understood.

2.3 Calculations of Thermal Transport in Superconducting Cavities

Several models have been developed to compute the equilibrium surface temperatures expected on the inside surface of a cavity as a

function of the magnetic field at the surface. In each of these models the equilibrium temperature distribution is computed from the temperature-dependent functions for the surface resistance and the thermal transport processes: the surface resistance describes the power dissipation in the superconductor; the thermal conductivity determines the temperature gradients within the superconductor; the temperature drop between the outside surface of the cavity and the liquid helium bath is specified by the thermal boundary resistance.

Two of the models, by Hillenbrand et al. [2.24] and Isagawa and Isagawa [2.28] were used to calculate the equilibrium surface temperature for a Nb cavity with no surface defects. The calculations by Lyneis et al. [2.31] included a line defect in the superconductor. The HEAT model and computer program developed by Deniz and Padamsee [2.32] solves for the equilibrium temperature distribution in the vicinity of a small circular defect; this model was used to analyze the microwave performance of the Nb cavities used in this investigation.

2.4 HEAT Program

In the HEAT model a circular defect is located at the center of the top surface of a thin cylindrical disk, as shown in Figure 2.1; the disk radius is chosen to be much greater than the defect radius. A uniform magnetic field is present at the surface of the disk. The power dissipated at the surface of the disk then flows to the side and bottom of the disk, which are in direct contact with liquid helium; the helium bath temperature is specified as an input parameter. Because of the circular symmetry of the disk and defect, heat flows only in the r and z

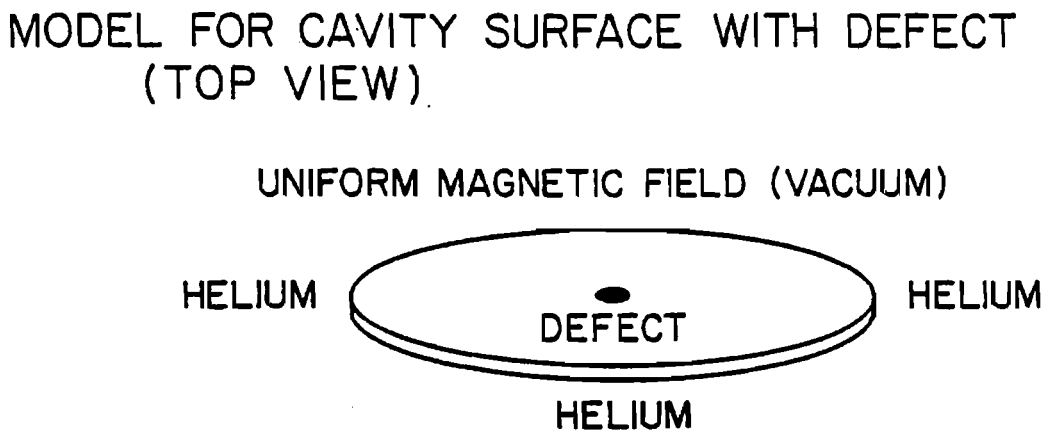

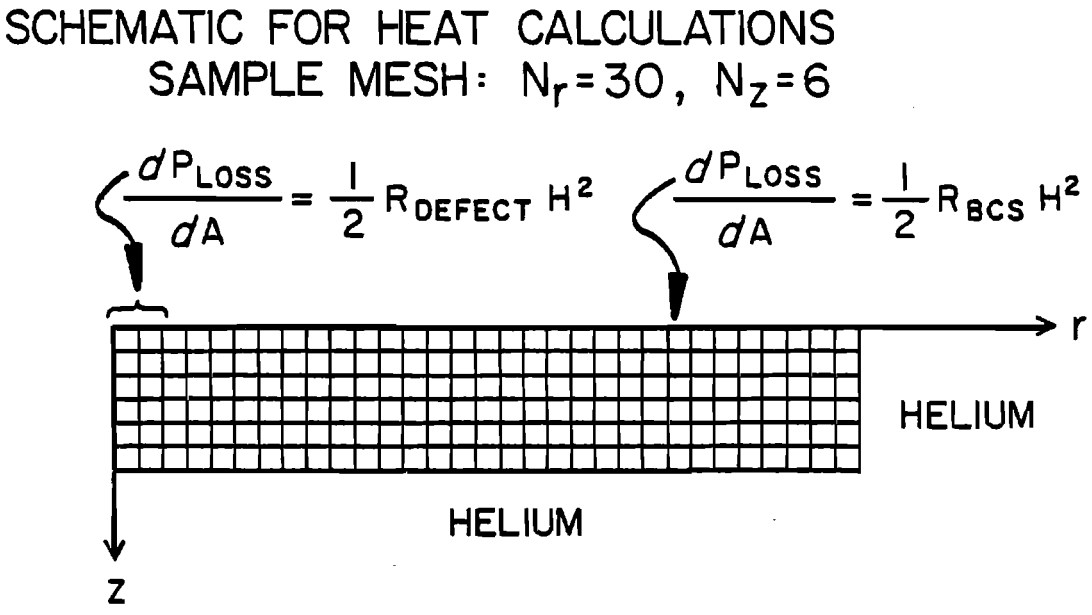

Figure 2.1 Schematic of cavity surface for HEAT calculations.

directions. The disk is therefore divided into N_z slices in the z direction which are further divided into N_r rings of equal width; thus a total of $N_z \times N_r$ mesh elements are used in the calculations. This is illustrated in the bottom of Figure 2.1 for a sample case of a 6×30 mesh.

The surface resistance at the top of the disk is given by BCS surface resistance everywhere except at the location of the defect; the size and resistance of the defect are specified as input parameters. The surface resistance is set equal to the defect resistance when the temperature exceeds the critical temperature corresponding to the surface magnetic field; the dependence of the critical temperature on the magnetic field level is taken to be [2.2]

$$T_c(H) = T_c(0) \times \left(1 - \frac{H}{H_c}\right)^{\frac{1}{2}} .$$

Heat flow within the disk is determined by temperature-dependent functions for the thermal conductivity of the superconductor and the metal to liquid helium boundary resistance; in addition, a maximum heat flux may be chosen (see the discussion of film boiling in liquid helium in Chapter 4).

The HEAT program solves for the temperature at each mesh element by requiring that the heat flowing into the element equals the heat flowing out of the element. In equilibrium, the temperature at each element may be determined from the temperatures of the elements adjacent to it and the temperature-dependent functions for heat generation and transport. The program begins with an initial temperature distribution and computes a new temperature at every mesh element by means of the heat balance equation; at each mesh element the values for the surface resistance, thermal conductivity, and thermal boundary resistance are

recomputed before proceeding to compute a new temperature at the next mesh element; this procedure is repeated until the calculated temperatures have converged to a final solution and the total power dissipated at the surface equals the heat flowing out of the disk. The convergence process is considerably shortened by using the method of over-relaxation.

The HEAT program was checked in several ways. First, the magnetic field was set to zero and an initial temperature distribution was specified that was different from the bath temperature; the program correctly computed that the entire disk should be at the bath temperature. The HEAT program was also modified for comparison with the calculations of Isagawa and Isagawa for a defect free Nb surface [2.28]; the functions for surface resistance and thermal transport were chosen to be the same as for their calculations; heat conduction out the side of the disk was set to zero so that the heat flow would be one-dimensional. Using this modified program and input parameters supplied by Isagawa [2.33] the HEAT program was found to agree with their calculations at low powers. Isagawa and Isagawa also found that as they increased the power the magnetic field rose to some peak value and then began to fall. For a given magnetic field the HEAT program could only solve for the low power solution, even when the initial temperature distribution used in the calculations was much higher than the temperatures found by Isagawa and Isagawa for their high power solution. Thus the HEAT program is useful only in calculating the microwave performance of Nb cavities at low powers.

The physical origin of this double-valued behavior may be understood as follows: as the heat flux is increased the cavity temperature rises due to the thermal boundary resistance; at high heat fluxes the

temperature rise causes the surface resistance to increase very rapidly with increasing power; thus at very high heat fluxes the magnetic field, given by

$$H^2 = 2 \frac{P_{diss}/A}{R_s(T)} ,$$

may actually decrease as the power level increases. This effect is not normally observed because most cavities exhibit breakdown at low heat fluxes. This effect was observed at the high heat fluxes that were sustained with the high thermal conductivity cavities used in this investigation (see Figure 7.9).

Calculations with the HEAT program clearly demonstrate the importance of the thermal transport processes in the performance of superconducting Nb cavities. The breakdown field level was computed for the specific case of a defect of resistance 4×10^{-3} ohms and radius 0.0075 cm located at the center of a disk of radius 0.6 cm and thickness 0.075 cm. The thermal conductivity of Nb in the superconducting state for temperatures between about 3-9K scales linearly with the residual resistivity ratio* (RRR) of the Nb. The computed breakdown fields at 9 GHz for a liquid helium temperature of 2K were 300, 575, 675, and 700 Oersteds for Nb disks with RRRs of 15, 300, 1900, and 33000 respectively. A RRR of 15 is typical for the reactor grade Nb used in most cavities; 33,000 is one of the highest values reported in the literature for a RRR for Nb. Thus the thermal conductivity of the Nb is expected to significantly affect the performance of superconducting Nb cavities. In particular, these

*The residual resistivity ratio of a sample is the ratio of its room temperature resistivity to its normal state resistivity at absolute zero.

calculations indicate that the microwave performance of Nb cavities may be considerably improved by the use of Nb with a RRR of several hundred; the best microwave performance will be obtained with Nb with a RRR of several thousand.

References for Chapter 2

[2.1] J. M. Pierce, in Methods of Experimental Physics, Vol. 11, ed. R. V. Coleman, Academic Press, NY, 1974, pg. 541.

[2.2] W. H. Hartwig and C. Passow, in Applied Superconductivity, Vol. 2, ed. Newhouse, Academic Press, NY, 1975.

[2.3] J. D. Jackson, Classical Electrodynamics, 2nd edition, John Wiley and Sons, NY, 1975.

[2.4] N. W. Ashcroft and N. D. Mermin, Solid State Physics, Holt, Rinehart, and Winston, NY, 1976.

[2.5] D. C. Mattis and J. Bardeen, Phys. Rev. 111, 412 (1958).

[2.6] J. Bardeen, L. N. Cooper, and J. R. Schrieffer, Phys. Rev. 108, 1175 (1957).

[2.7] J. P. Turneaure and I. Weissman, J. Appl. Phys. 39, 4417 (1968).

[2.8] J. Halbritter, Z. Physik 238, 466 (1970) and Z. Physik 266, 209 (1974).

[2.9] A. Philipp and J. Halbritter, IEEE Trans. MAG-17, 951 (1981).

[2.10] P. Wilson, Report No. SLAC-TN-70-35, Stanford Linear Accelerator Center, Stanford, California (Dec. 1970).

[2.11] W. Bauer, S. Giordano, and H. Hahn, J. Appl. Phys. 45, 5023 (1974).

[2.12] B. Piosczyk, P. Kneisel, O. Stoltz, and J. Halbritter, IEEE Trans. NS-20, 108 (1973).

[2.13] W. Schwarz and J. Halbritter, J. Appl. Phys. 48, 4618 (1977).

[2.14] H. Padamsee, M. Banner, and M. Tigner, IEEE Trans. NS-24, 1101 (1977).

[2.15] H. Padamsee and A. Joshi, J. Appl. Phys. 50, 1112 (1979).

[2.16] C. M. Lyneis, H. A. Schwettman, and J. P. Turneaure, Appl. Phys. Lett. 31, 541 (1977).

[2.17] C. Lyneis, Y. Kojima, and J. P. Turneaure, and N. T. Viet, IEEE Trans. NS-20, 101 (1973).

[2.18] Ph. Bernard, G. Cavallari, E. Chiaveri, E. Haebel, H. Heinrichs, H. Lengeler, E. Picasso, and V. Picciarelli, 11th Intnl. Conf. on High Energy Accelerators, Geneva, pg. 878 (1980).

[2.19] H. Padamsee, D. Proch, P. Kneisel, and J. Mioduszewski, IEEE Trans. MAG-17, 947 (1981).

[2.20] H. Lengeler, Cryogenics 18, 465 (1978).

[2.21] H. Pfister, Cryogenics 16, 17 (1976).

[2.22] H. Padamsee, M. Banner, J. Kirchgessner, M. Tigner, and R. Sundelin, IEEE Trans. MAG-15, 602 (1979).

[2.23] N. Krause, B. Hillenbrand, H. Pfister, and Y. Uzel, IEEE Trans. MAG-17, 927 (1981).

[2.24] B. Hillenbrand, H. Martens, K. Schnitzke, and H. Diepers, Proc. 9th Intnl. Conf. High Energy Accelerators, Stanford, pg. 143 (1974).

[2.25] H. Martens, H. Diepers, and B. Hillenbrand, Phys. Lett. 44A, 213 (1973).

[2.26] M. A. Allen, Z. D. Farkas, H. A. Hogg, E. W. Hoyt, and P. B. Wilson, IEEE Trans. NS-18, 168 (1971).

[2.27] P. B. Wilson, Z. D. Farkas, H. A. Hogg, and E. W. Hoyt, IEEE Trans. NS-20, 104 (1973).

[2.28] S. Isagawa and K. Isagawa, Cryogenics 20, 677 (1980).

[2.29] V. Lagomarsino, G. Manuzioi, R. Parodi, and R. Vaccarone, IEEE Trans. MAG-15, 25 (1979).

[2.30] R. W. Meyerhoff, J. Appl. Phys. 40, 2011 (1969).

[2.31] C. M. Lyneis and J. P. Turneaure, IEEE Trans. MAG-13, 339 (1976).

[2.32] A. Deniz and H. Padamsee, Report No. CLNS 79/434, Laboratory of Nuclear Studies, Cornell University, Ithaca, NY (1979).

[2.33] S. Isagawa, KEK National Laboratory for High Energy Physics, Japan, private communication.

Chapter 3

THERMAL CONDUCTIVITY OF NIOBIUM--A SURVEY OF THEORY AND EXPERIMENT

3.1 Introduction

In the normal state at low temperatures the electronic contribution to the total thermal conductivity of Nb is dominant and the phonon contribution is negligible. However, in the superconducting state the electronic contribution decreases rapidly as the temperature T falls below T_c because the electrons condense into Cooper pairs that do not transport any thermal energy. Furthermore, the lattice thermal conductivity increases in the superconducting state because fewer electrons are available to limit the lattice thermal conductivity through scattering of the phonons. Thus in the superconducting state the phonons may give rise to a significant portion of the total thermal conductivity and lead to additional structure in the measured thermal conductivities.

This survey is a compilation of the many measurements of the low temperature thermal conductivity of Nb in the normal and superconducting states [3.1-3.27]*, and a discussion of the physical mechanisms responsible for the observed thermal conductivity of Nb at low temperatures. A discussion of the physics underlying the thermal conductivity of Nb in the normal state will be given first, as this is essential for the discussion of the thermal conductivity of Nb in the superconducting state.

3.2 Normal State Electronic Thermal Conductivity

A representative selection of published results for the low

*Refer to K. R. Krafft, Report No. CLNS 80/468, Laboratory of Nuclear Studies, Cornell University (1980), for details about the measurements performed by each researcher.

temperature thermal conductivity of Nb in the normal state is shown in Figure 3.1. (Because many published graphs are very small in size the curves shown in Figures 3.1 and 3.2a-3.2c are not drawn with a high degree of accuracy; the reader should certainly consult the original publications if a high degree of accuracy is required.)

The range in the measured thermal conductivities of Nb in the normal state arises because of the varying purities of the samples studied. A measure of the sample purity that is particularly useful in understanding the electronic thermal conductivity of a sample is the low-temperature electrical resistivity. At low temperatures the normal state electrical resistivity may be described by $\rho(T) = \rho_o + \rho_{ideal}(T)$. The residual resistivity ρ_o arises because defects such as impurities, vacancies and dislocations (line defects) scatter conduction electrons and limit the electrical conductivity; ρ_o is essentially independent of temperature for $T < T_{Fermi}$, where $T_{Fermi} = 1.1 \times 10^5$K for Nb [3.28]; ρ_o is thought to scale linearly with the impurity concentration for low concentrations of a given impurity (see the discussion in Section 5.2). $\rho_{ideal}(T)$ describes the temperature dependent part of the resistivity arising from electron-electron scattering and electron-phonon scattering [3.29-3.30]. For most Nb samples $\rho_o >> \rho_{ideal}(T)$ for $T \lesssim 10$K; only for very pure samples, with impurity content less than of the order of 1-10 parts per million (atomic), will ρ_{ideal} (4.2K) be comparable to ρ_o. The purity of a sample may therefore be characterized by measuring ρ at room temperature, $\rho(Rm.T)$, and $\rho(4.2K) \simeq \rho_o$; $\rho(Rm.T)$ is constant for Nb (about 14 $\mu\Omega$-cm); thus the higher the residual resistivity ratio (RRR) $\rho(Rm.T)/\rho_o$ is the higher the purity of the sample. The range of RRRs for the Nb samples represented in Figure 3.1 is 5 to 33,000.

Figure 3.1 Thermal conductivity of Nb in the normal state.

KEY

Curve No.	Symbol	Author(s)	Ref. No.	Sample	RRR (see Table 3.1)
1	———	Gladun et al.	[3.6]		33,000
2	— — —	Oota and Masuda	[3.16]	Nb 6300	6,300
3	— — — —	Reiche and Pompe	[3.18]	Nb Z-135	4,910
4	———	Oota and Masuda	[3.16]	Nb 2500	2,500
5	———	Oota and Masuda	[3.16]	Nb 1090	1,090
6	———	Reiche and Pompe	[3.18]	Nb E(u)	396
7	———	Oota and Masuda	[3.16]	Nb 195	195
8	———	Kuhn	[3.9]	Nb I	∿155
9	— · — ·	Kuhn	[3.9]	Nb III DA	∿70
10	———	Kuhn	[3.9]	Nb IV AA	∿40
11	— · — ·	White and Woods	[3.26]	Nb 5	32
12	— — —	Wasim and Zebouni	[3.23]		29
13	— — — —	Merisov et al.	[3.13]		∿27
14	— · — ·	Kes et al.	[3.7]	P1600	24.3
15	———	Klauss	[3.8]		∿20
16	———	Kes et al.	[3.7]	P1400	15.6
17	— — —	Rosenberg	[3.12]	Cb 1	10.4
18	———	Reiche and Pompe	[3.18]	Film #3	7.98
19	— — — —	Kuhn	[3.9]	NbI reannealed	∿6
20	———	Cannelli & Cannelli	[3.27]		20

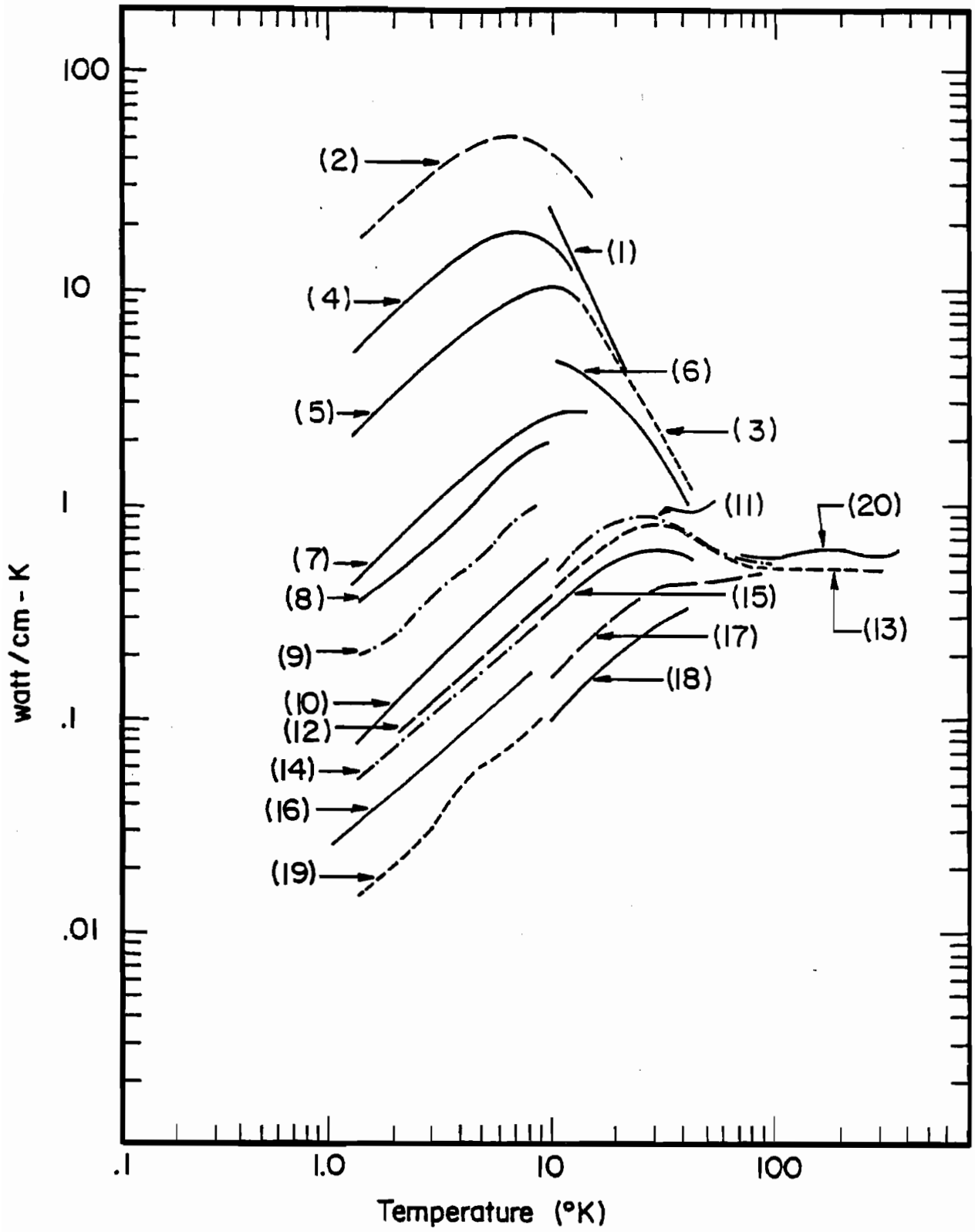
100
10
1
.1
.01
watt/cm - K
.1
1.0
10
100
Temperature (°K)
(1)
(2)
(3)
(4)
(5)
(6)
(7)
(8)
(9)
(10)
(11)
(12)
(13)
(14)
(15)
(16)
(17)
(18)
(19)
(20)

Figure 3.1

The low temperature normal state thermal conductivity of Nb is dominated by the electronic thermal conductivity; the lattice thermal conductivity in the normal state is negligible, as discussed in Section 3.4. Both scattering by defects and scattering by phonons limit the ability of electrons to transport thermal energy. Quantitative formulas may be derived for the expected electronic thermal conductivity at low temperatures, starting from the simple model for thermal conductivity which gives the thermal conductivity $\kappa(T)$ as (see Reference [3.31], for example)

$$\kappa(T) = \frac{1}{3} \times C_v \times v^2 \times \tau \qquad (3.1)$$

where C_v is the specific heat per unit volume, v is the average velocity of the carriers of the thermal energy, and τ^{-1} describes the scattering rate of the carriers. As a first approximation one may assume that the scattering rates due to different scattering mechanisms add linearly. Then the electronic thermal resistivities $W^{el} = (\kappa^{el})^{-1}$ will add together to give

$$W^{el} \simeq W^{el}_{defect} + W^{el}_{phonon} \, . \qquad (3.2)$$

The thermal resistivity due to defects is described theoretically by $W^{el}_{defect} \simeq B/T$ at low temperatures, since $C^{el}_v \propto T$ (see References [3.31-3.33]) while the electronic velocity and the electron-defect scattering rate are approximately temperature independent. B is proportional to the electron-defect scattering rate, and is therefore also proportional to ρ_o. A useful quantity to consider here is

$$L_o = \rho_o/(T \times W^{el}_{defect}) = \rho_o/B \, . \qquad (3.3)$$

The Lorenz number L_o will be independent of both temperature and defect concentration since both ρ_o and B are temperature independent and are proportional to the scattering rate of electrons by defects. In the free electron model L_o is given by the Wiedemann-Franz law as [3.31]

$$L_o = \frac{\pi^2}{3}(k_B/e)^2 = 2.44\times10^{-8} \text{ watt-}\Omega/K^2 . \qquad (3.4)$$

The scattering of electrons by phonons gives rise to a term $W^{el}_{phonon} = AT^2$ for $T \lessapprox \theta_D/10$, where the Debye temperature, θ_D, is approximately 275K for Nb [3.31]. The temperature dependence of W^{el}_{phonon} may be seen as follows: the electronic specific heat is proportional to T, while the scattering rate of electrons by phonons should be proportional to the number of phonons which is in turn proportional to T^3 for $T \lessapprox \theta_D/10$ (see [3.32], pg. 217); thus for $T \lessapprox \theta_D/10$

$$W^{el}_{phonon} \propto C_v^{-1} \times \frac{1}{\tau} \propto T^{-1} \times T^3 \propto T^2 .$$

A similar argument may be used to predict that at higher temperatures W^{el}_{phonon} should become approximately constant. For $\theta_D \gtrsim T \gtrsim \theta_D/10$ the total number of phonons increases linearly with temperature (see [3.32], pp. 202-3); thus

$$W^{el}_{phonon} \propto C_v^{-1} \times \frac{1}{\tau} \propto T^{-1} \times T \sim \text{constant} .$$

This is in agreement with the experimental results for Nb for $100K \lessapprox T \lessapprox 1000K$ [3.34].

An exact calculation of the effectiveness of phonons in limiting electronic thermal conduction is difficult to perform. The theoretical expression given by J. M. Ziman ([3.33], Eq. (9.10.18)) for W^{el}_{phonon} leads to, for $T < \theta_D/10$,

$$W^{el}_{phonon} \times T^{-2} = A = \frac{95.3\ N_{eff}^{2/3}}{\kappa_\infty \theta_D^2}\ , \qquad (3.5)$$

where N_{eff} is the effective number of conduction electrons per ion and κ_∞ is the high temperature value of κ^{el} (using $\rho_\theta = L_o\theta/\kappa_\infty$ and Reference [3.31], Eqs. (2.21) and (23.22)). Using $N_{eff} = 5$, the nominal valence of Nb, $\theta_D = 275$K, and $\kappa_\infty \simeq 0.6$ watt/cm-K [3.27] gives $A = 6\times10^{-3}$ cm/watt-K in Eq. (3.5).

Thus the total low temperature electronic thermal resistivity for Nb in the normal state is predicted to be given by

$$W^{el} = AT^2 + B/T \qquad (3.6)$$

with $A = 6\times10^{-3}$ cm/watt-K and $B = \rho_o/L_o$. Furthermore, the maximum value of the low temperature electronic thermal conductivity, κ_{max}, should be given by

$$\kappa_{max} = \frac{2^{2/3}}{3} A^{-1/3} B^{-2/3} \propto \rho_o^{-2/3}\ , \text{ at } T_{max} = \left(\frac{B}{2A}\right)^{1/3} \propto \rho_o^{1/3}\ . \qquad (3.7)$$

The measured curves of the low temperature electronic thermal conductivity in Figure 3.1 are in good qualitative agreement with these theoretical predictions: at low temperatures the measured thermal conductivities decrease linearly as the temperature is decreased due to electron-defect scattering; at higher temperatures the measured thermal conductivities decrease in proportion to T^{-2} as the temperature is increased due to electron-phonon scattering.

Tables 3.1 and 3.2 provide a quantitative comparison of the experimental results and theoretical predictions. Table 3.1 presents a summary of the values of A and B obtained by using the published curves

Table 3.1 Normal State Thermal Conductivity of Nb--Summary of Experimental Results

Ref.	Sample	$\frac{\rho(Rm.T)}{\rho(T)}$	T	A	B	ρ_o	B/ρ_o
			K	$\frac{10^{-3}cm}{watt-K}$	$\frac{cm-K^2}{watt}$	$\mu\Omega$-cm	$\frac{K^2}{watt-\mu\Omega}$
[3.6]		33,000	0	.49*	<.02	$4.2x10^{-4}$	<48
[3.16]	Nb 6300	6,300	4.2	.16*	.080	$1.8x10^{-3}$[b]	44
[3.18]	Z-Nb 135	4,910	0	.48*	.38	$3.14x10^{-3}$	120
[3.16]	Nb 2500	2,500	4.2	.42*	.23	$5.6x10^{-3}$	41
[3.15]	Nb I	1,900	0	.64*	.25	$6.9x10^{-3}$	36
[3.19]	Nb I	1,570	4.2	--	.36	--	40[e]
[3.25]	Nb H2	1,200	0	∿.62*	∿.45	--	∿39[e]
[3.16]	Nb 1090	1,090	4.2	.40*	.58	$1.3x10^{-2}$	45
[3.22]	B	700	4.2	--	1.05	--	53[e]
[3.5]		397		.6*	--	--	--
[3.18]	Nb E(u)	396	0	.54*	1.72	$3.51x10^{-2}$	49
[3.25]	Nb H1	350	0	∿1.0*	∿1.5	--	∿38[e]
[3.24]		300	0	∿1.0*	∿1.6	--	∿34[e]
[3.25]	Nb K6	250	0	∿.62	∿1.0	--	∿18[e]
[3.18]	Nb E(m)	240[c]	0	.57	2.4	--	--
[3.16]	Nb 195	195	4.2	.83	2.79	$7.2x10^{-2}$	39
[3.25]	Nb K10	185	0	∿.94*	∿3.0	--	∿40[e]
[3.9]	Nb I	155[d]	0	∿1	3.8	.09	42
[3.10]	Nb III	120	0	--	∿4.5	--	∿39[e]
[3.9]	Nb III DA	70[d]	0	--	∿8.2	.21	∿39
[3.19]	Nb II	61	4.2	--	10	--	44[e]
[3.10]	Nb II	60.5	0	--	∿11	--	∿48[e]

Table 3.1 (continued)

Ref.	Sample	$\frac{\rho(Rm.T)}{\rho(T)}$	T K	A $\frac{10^{-3}cm}{watt-K}$	B $\frac{cm-K^2}{watt}$	ρ_o $\mu\Omega$-cm	B/ρ_o $\frac{K^2}{watt-\mu\Omega}$
[3.9]	Nb IV B	60[d]	0	--	9.3	.22	42
[3.20]		45	0	--	14	--	45[e]
[3.21]		44	10	--	13	--	41[e]
[3.10]	Nb I	40[c]	0	--	15	--	--
[3.9]	Nb IV AA	~40[d]	~0	--	16	.38	42
[3.26]	Nb 5	32	0	.55*	19	.47	40
[3.22]	A	30[c]	~0	--	19	--	--
[3.23]		29	0	2	20.8	.52	40
[3.13]		27[d]	0	~.5*	23	.52	44
[3.7]	P1600	24.3	4.2	1.5	27.5	.68	40
[3.19]	monocrystal	22.5	10	--	29	--	--
[3.7]	N-0	21.1	4.2	1.7	30.2	.74	41
[3.8]		20[c]	~0	.6*	29	--	--
[3.7]	N-319	16.2	4.2	1.4	37.4	.95	39
[3.7]	P1400	15.6	4.2	4.1	46.6	1.08	43
[3.18]	PC	11.4	0	.70	54	1.33	41
[3.12]	Cb 1	10.4	20	.4-.5*	~60	--	~45[e]
[3.11]		8[c]		--	~70[a]	--	--
[3.18]	Film #3	7.98	0	.6	82	2.15	38
[3.18]	Film #49	6.92	0	~.4	90	2.53	36
[3.9]	Nb I-reanneal	~6[d]	~0	--	~95	2.48	~38

Table 3.1 (continued)

*Denotes that $\kappa(T)$ was measured at high temperatures where $\kappa(T)$ decreases with increasing temperature.

[a]Estimated by setting $B = 10\ K/\kappa(10\ K)$.

[b]$\rho(4.2\ K) = 2.2 \times 10^{-3}\ \mu\Omega$-cm for this sample. The results of Alekseyevskiy et al. [3.30] imply that $\rho_o \sim 1.8 \times 10^{-3}\ \mu\Omega$-cm.

[c]The value of the residual resistivity ratio is inferred from the value of B using the Wiedemann-Franz law, and an average value of $\rho(Rm.T)$ of $14\mu\Omega$-cm.

[d]The value of the residual resistivity ratio is estimated from the value of ρ_o taking $\rho(Rm.T) = 14\mu\Omega$-cm.

[e]The value of ρ_o is estimated using the residual resistivity ratio and and an average value of $\rho(Rm.T)$ of $14\mu\Omega$-cm.

Table 3.2 Normal State Thermal Conductivity--Experimental Results for κ_{max} and T_{max}

Ref.	Sample	ρ_o $\mu\Omega$-cm	κ_{max} watt/cm-K	T_{max} K	$\kappa_{max}\,\rho_o^{2/3}$ watt$(\mu\Omega\text{-cm})^{2/3}$/cm-K	$T_{max}/\rho_o^{1/3}$ K/$(\mu\Omega\text{-cm})^{1/3}$
[3.16]	Nb 6300	1.8×10^{-3}[a]	49	~6.2	.73	51
[3.16]	Nb 2500	5.6×10^{-3}	19	~6.5	.60	37
[3.16]	Nb 1090	1.3×10^{-2}	10	~9.4	.55	40
[3.18]	Nb E(m)	--	3.5	~12	--	--
[3.25]	Nb K10	.08[b]	2.7	12	.50	28
[3.26]	Nb 5	.47	.88	25	.53	32
[3.13]		.52	.89	33	.58	41
[3.8]		--	~.62	25	--	--
[3.12]	Cb1	1.3[b]	.67	23	.80	21
Average Value					.6±.1	36±9

[a] $\rho(4.2K) = 2.2\times10^{-3}\mu\Omega$-cm for this sample. The results of Alekseyevskiy et al. [3.30] imply that $\rho_o = 1.8\times10^{-3}\mu\Omega$cm.

[b] The value of ρ_o is estimated from the residual resistivity ratio, taking an average value for ρ(Rm.T) of 14$\mu\Omega$-cm.

of $\kappa(T)$ to plot $W(T)\times T$ against T^3; the results are listed in order of decreasing sample purity. Table 3.2 presents a summary of the values of κ_{max} and T_{max} for those curves of $\kappa(T)$ that were measured over a sufficiently large temperature range to exhibit a maximum.

First consider the defect scattering term in the electronic thermal resistivity. The Wiedemann-Franz law predicts that $B/\rho_o = 41\ K^2/\text{watt-}\mu\Omega$. This is in good agreement with the results for B/ρ_o listed in the last column of Table 3.1 for samples whose residual resistivities spanned more than three orders of magnitude. Hence the defect scattering term in the electronic thermal resistivity is in reasonable agreement with the theoretical predictions.

The phonon scattering term in the measured electronic thermal resistivities varies with the sample measured, and is not in good agreement with the prediction for the magnitude of $A = W^{el}_{phonon} \times T^{-2}$. From Eq. (3.5) A was predicted to be 6×10^{-3} cm/watt-K, whereas values from 0.2×10^{-3} to 4×10^{-3} cm/watt-K are reported in Table 3.2. In part, this lack of agreement between theory and experiment may be due to the uncertainties in fitting the high temperature part of the curves; many of the thermal conductivities are not even measured for temperatures up to $T = T_{max}$ where the phonon scattering term becomes significant; also for the relatively impure samples the phonon scattering of electrons only becomes important for $T > \theta_D/10$, where the theory is no longer valid. More consistent results for A are obtained by considering only those samples that were measured at high temperatures where the strength of the phonon scattering of electrons was sufficient to cause $\kappa(T)$ to decrease with increasing temperature. For these entries in Table 3.1

(marked with a *) the experimental values for A ranged from $0.2\text{-}1.0\times10^{-3}$ cm/watt-K; the mean value of A for these samples was $0.6\pm0.2\times10^{-3}$ cm/watt-K. One may postulate that N_{eff}, the effective number of conduction electrons per ion, is smaller than five, which is the nominal valence of Nb; Eq. (3.5) with $A = 0.6\times10^{-3}$ cm/watt-K gives an extremely low value for N_{eff} of 0.16 electrons per ion. Thus it appears that Eq. (3.5) must overestimate the strength of the electron-phonon scattering.

A final comparison between experimental results and theoretical predictions is provided in Table 3.2; $\kappa_{max}\rho_o^{2/3}$ and $T_{max}/\rho_o^{1/3}$ are approximately constant for a range of ρ_o of three orders of magnitude; this result is consistent with the predictions given in Eq. (3.7).

Lastly, no significant changes in the normal state thermal conductivities were observed for samples that were deliberately strained (see References [3.10, 3.24, and 3.25] and the discussion in Section 5.2). The normal state thermal conductivity of samples that were irradiated with neutrons decreased slightly [3.4, 3.7, and 3.9]; most likely, this decrease is due to an increase in the density of point defects [3.7].

In summary, the low temperature thermal conductivity of Nb in the normal state may be understood as arising from thermal conduction by electrons that are scattered by impurities and phonons. The theory discussed here describes the observed behavior of the normal state low temperature thermal conductivity of Nb quite well, although there are some discrepancies between the theoretical predictions and the experimental observations.

3.3 Superconducting State Electronic Thermal Conductivity

A selection of measurements of the thermal conductivity of Nb in the superconducting state are shown in Figures 3.2a-3.2c; for clarity, the measurements are grouped according to the relative purities of the samples.

The theoretical description of the electronic thermal conductivity in the superconducting state is quite complicated because the electrons are not independent; rather, the electronic behavior must be treated in terms of many-body physics. In the normal state relatively simple arguments could be used to predict the temperature behavior of the electronic thermal conductivity. In the superconducting state one must deal with approximate solutions that yield integral equations which must be solved numerically. These equations have been solved by others, and results published in the literature giving the ratio of the electronic thermal conductivity in the superconducting and normal states. Both Bardeen, Rickayzen and Tewordt [3.35] (BRT) and Kadanoff and Martin [3.36] (KM) have published curves for $\kappa_s^{el}/\kappa_n^{el}$ as a function of T/T_c for the case where only electron scattering by defects is limiting the electronic thermal conductivity. Calculations of $\kappa_s^{el}/\kappa_n^{el}$ in the case where only electron scattering by phonons is important were performed by KM and later refined by Tewordt [3.37]; Ambegaokar and Tewordt [3.38] also performed a theoretical calculation in this case for strong coupling superconductors. KM also calculated $\kappa_s^{el}/\kappa_n^{el}$ for the case where the scattering is due to both phonons and defects, in terms of a parameter

$$a_c = \frac{W_{phonon}^{el}\ (T_c)}{W_{defect}^{el}\ (T_c)} = \frac{AT_c^3}{B} \qquad (3.8)$$

Figures 3.2a-3.2c Thermal conductivity of Nb in the superconducting state.

KEY

Curve	Symbol	Author(s)	Ref.	Sample	RRR
1	—··—··	Gladun et al.	[3.6]	sandblasted	33,000
2	— — —	Oota and Masuda	[3.16]	Nb 6300	6,300
3	———	Oota and Masuda	[3.16]	Nb 2500	2,500
4	— — —	Anderson and Smith	[3.1]	A-sandblasted	2,000
5	———	Muto et al.	[3.15]		1,900
6	———	Wasserbach	[3.25]	H2-undeformed	1,200
7	———	Reiche and Pompe	[3.18]	Nb E(u)	396
8	—···—···	Wasserbach	[3.24]		300
9	—— —	Anderson and Smith	[3.1]	B(before annealed, sandblasted)	196
10	———	Kuhn	[3.9]	NbI-before irradiation and reannealing	155
11	— — —	Anderson and Smith	[3.1]	C-sandblasted	135
12	—·—·	Connolly and Mendelssohn	[3.10]	Nb III	120
13	— — —	Kuhn	[3.9]	Nb IVB	60
14	———	Kuhn	[3.9]	Nb IVAA	40
15	—— —	Wasim and Zebouni	[3.23]		29
16	— — —	Anderson and Smith	[3.1]	D-sandblasted	26
17	—···—··	Kes et al.	[3.7]	N-0	21.1
18	— — —	Kes et al.	[3.7]	N-319(irradiated)	16.2
19	———	Kes et al.	[3.7]	P1400	15.6
20	— — — —	Kuhn	[3.9]	NbI-reannealed after irradiation	6
21	———	Phillips	[3.17]	Annealed	-

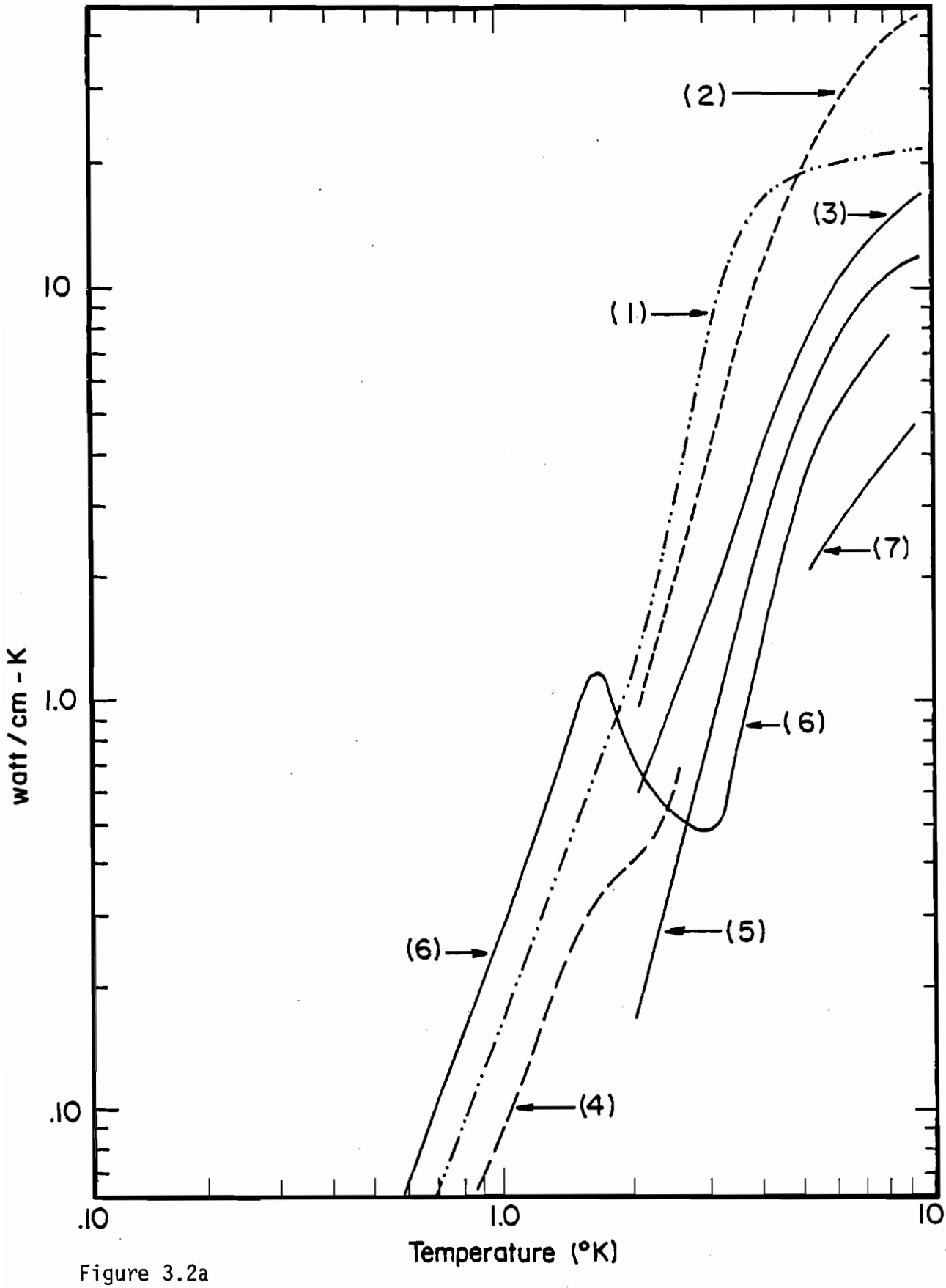

Figure 3.2a

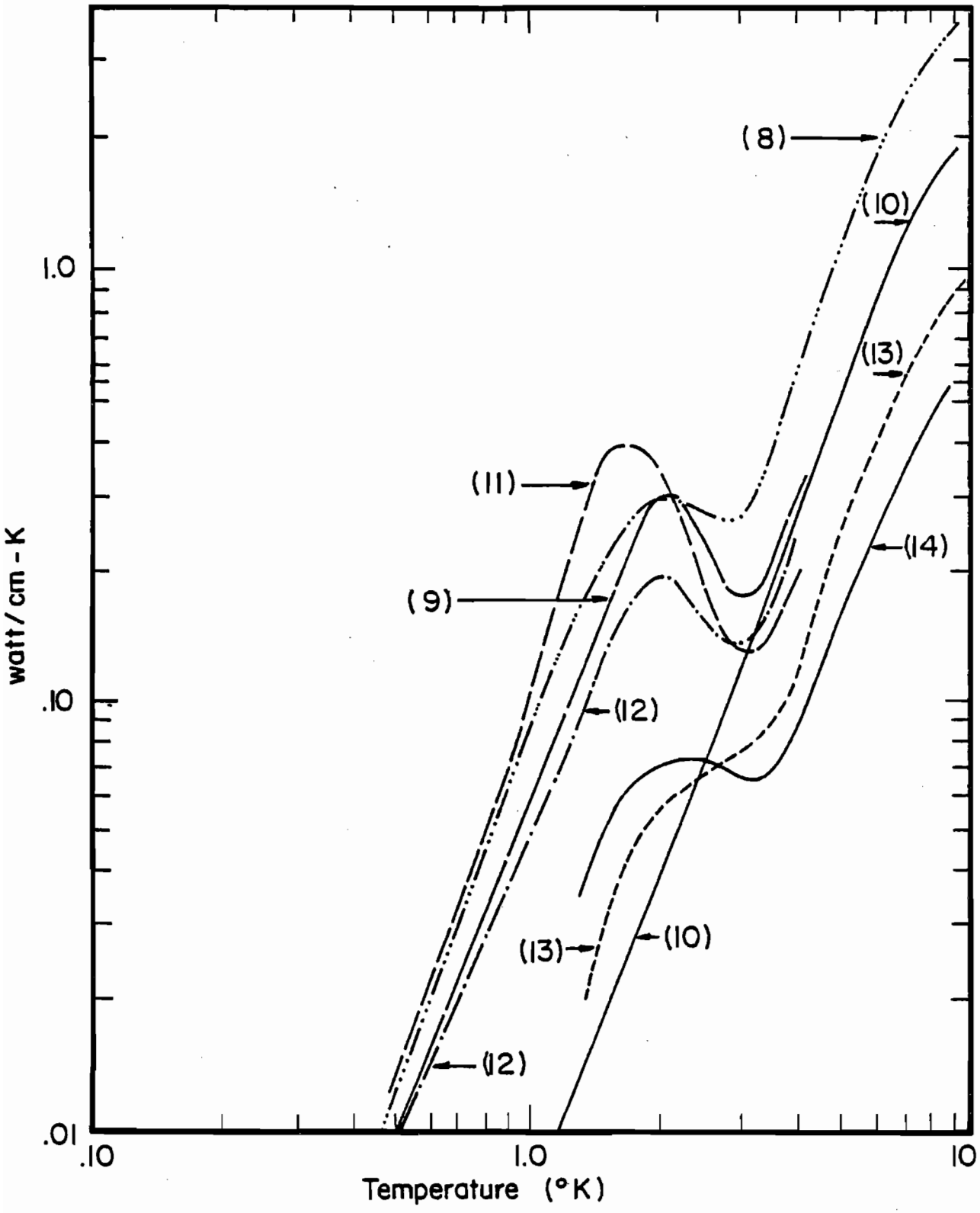

Figure 3.2b

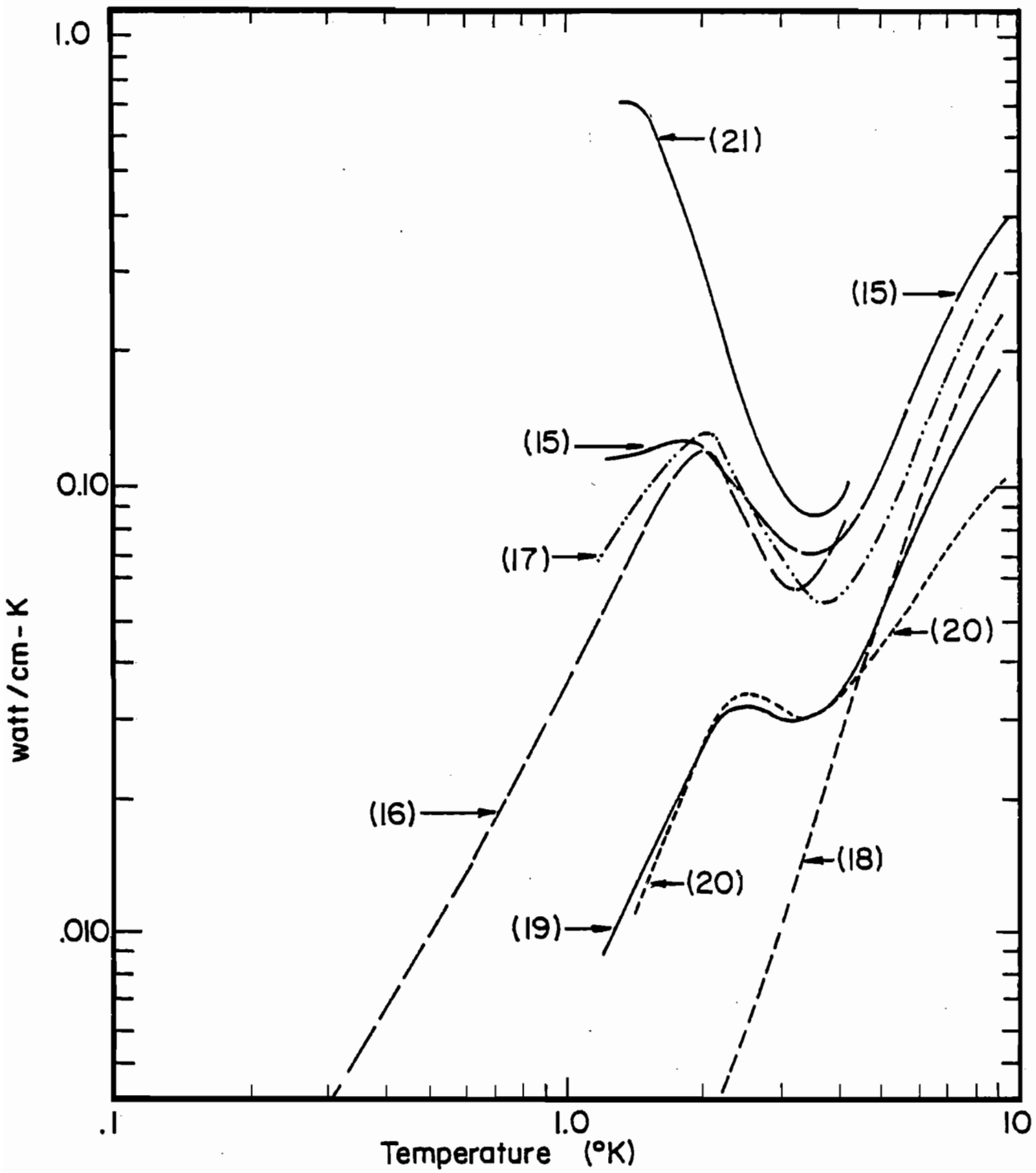
1.0
0.10
.010
watt/cm-K
.1
1.0
10
Temperature (°K)
(21)
(15)
(15)
(17)
(20)
(16)
(18)
(20)
(19)

Figure 3.2c

which measures the ratio of the phonon scattering to defect scattering of electrons at $T = T_c$. Figure 3.3 shows the theoretical predictions of KM for the cases where defect scattering dominates ($a_c = 0$), phonon scattering dominates ($a_c = \infty$), and for an intermediate case where phonons and defects scatter equally at $T = T_c$ ($a_c = 1$). All three curves in Figure 3.3 are very similar in appearance: $\kappa_s^{el}/\kappa_n^{el}$ decreases from 1.0 as T decreases from T_c and the electrons condense into Cooper pairs. A feature to be noted in Figure 3.3 is the slope of the curves at $T = T_c$; for defect scattering alone the slope of $\kappa_s^{el}/\kappa_n^{el}$ at $T = T_c$ is zero, while if phonon scattering takes place the slope is non-zero.

This predicted behavior for $\kappa_s^{el}/\kappa_n^{el}$ is confirmed experimentally. Figures 3.4a-3.4c show measured values of κ_s/κ_n and theoretical calculations for $\kappa_s^{el}/\kappa_n^{el}$ for samples where a_c ranges from 1.4 (in Figure 3.4a) to zero (in Figure 3.4c). The agreement between theory and experiment at high temperatures is very good; the deviations at low temperatures arise because in the superconducting state the lattice thermal conductivity becomes significant; the low temperature deviations are largest for the lower purity samples with low electronic thermal conductivities.

For Nb of very high purity the BRT and KM expressions for $\kappa_s^{el}/\kappa_n^{el}$ are not in good agreement with experiment at the higher temperatures where electron scattering by phonons is important. The results of both Oota and Masuda [3.16] for their sample of RRR = 6300 (shown in Figure 3.4a) and Gladun et al. [3.6] for their sample of RRR = 33,000 lie below the KM expression for $\kappa_s^{el}/\kappa_n^{el}$ derived for weak coupling superconductors for $T/T_c \gtrapprox 0.5$; however, these experimental results for $\kappa_s^{el}/\kappa_n^{el}$ lie closer to, but somewhat above, the curve calculated on the basis of the

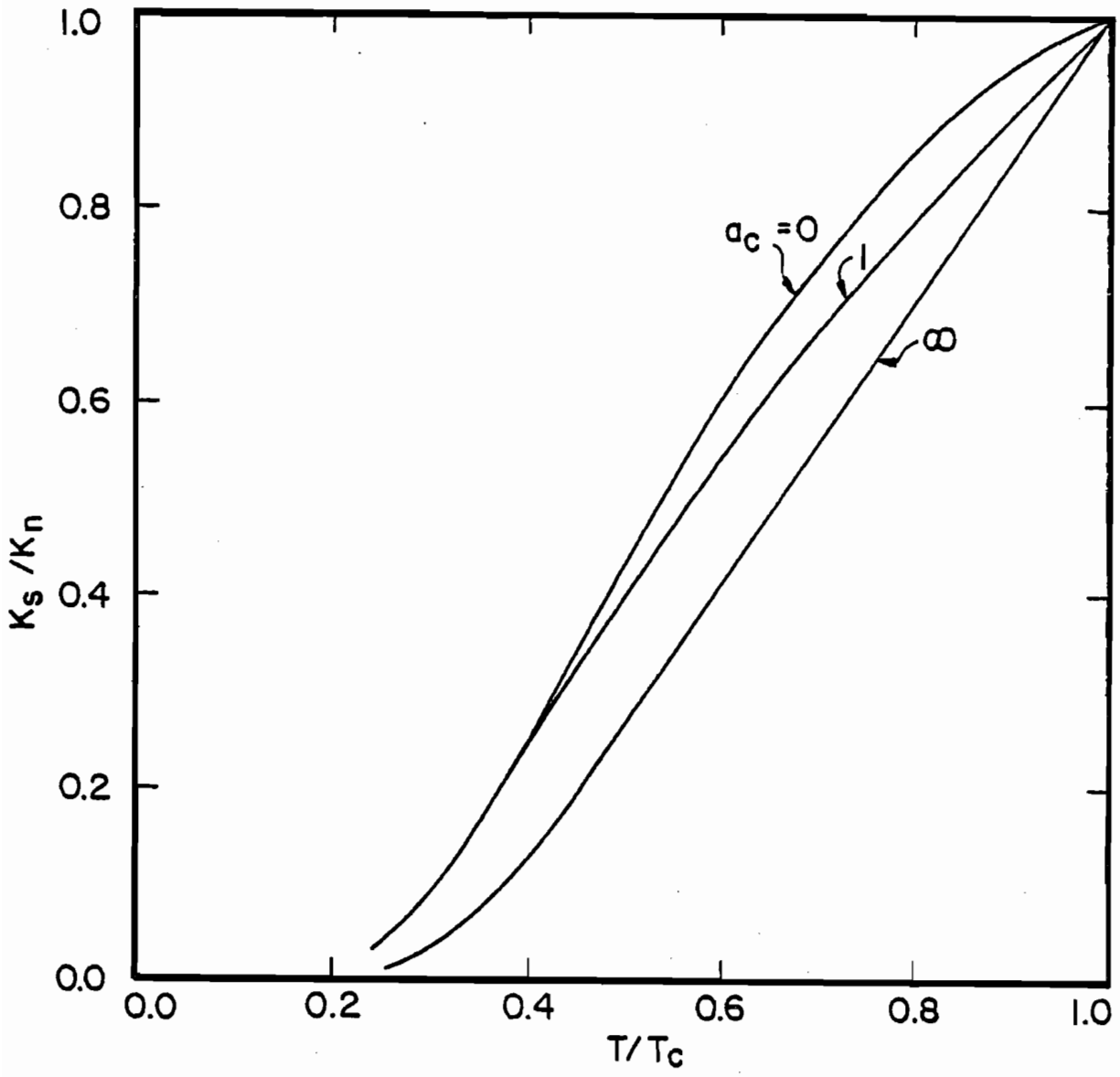

Figure 3.3 Theoretical predictions of Kadanoff and Martin [3.36] for the ratio $\kappa^{el}{}_s/\kappa^{el}{}_n$. The parameter a_c is defined in Eq. (3.8).

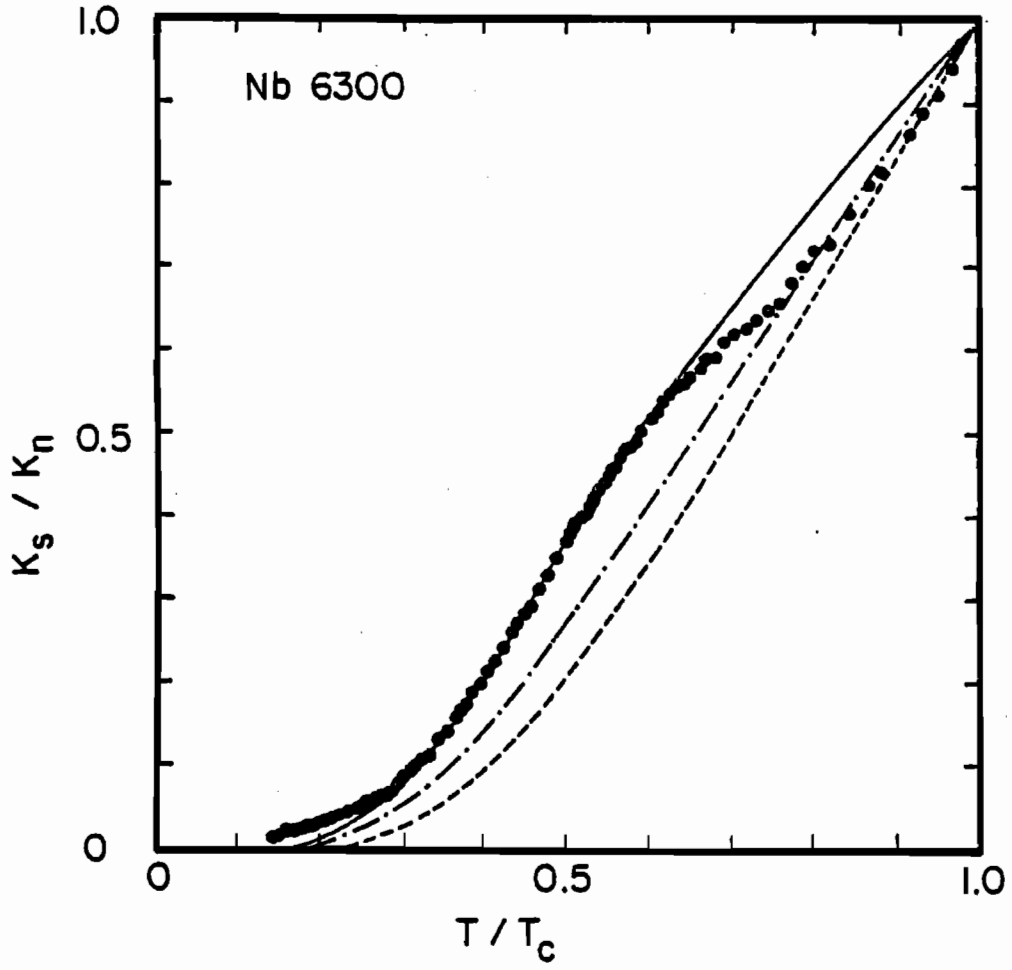

Figure 3.4a Measured curve for κ_s/κ_n for a sample of RRR = 6300 [3.16]. —— gives the KM theoretical prediction for $\kappa^{el}{}_s/\kappa^{el}{}_n$ with $a_c = 1.41$ and $\Delta(0)/k_BT_c = 1.75$. ----- gives the KM theoretical prediction for $\kappa^{el}{}_s/\kappa^{el}{}_n$ with $a_c = 1.41$ and $\Delta(0)/k_BT_c = 2.25$. —·—· gives the KM theoretical prediction for $\kappa^{el}{}_s/\kappa^{el}{}_n$ with $a_c = \infty$ and $\Delta(0)/k_BT_c = 1.75$.

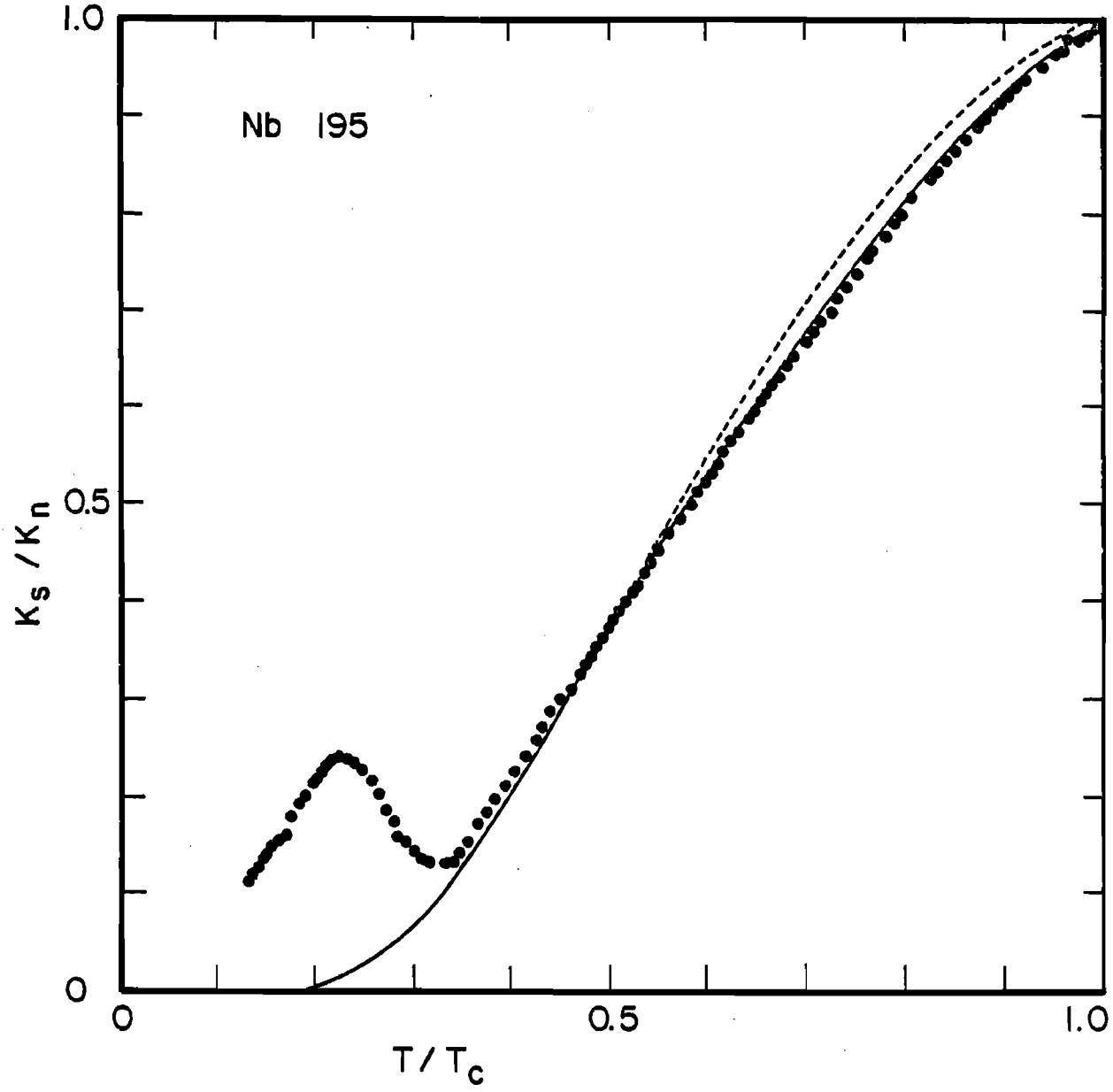

Figure 3.4b Measured curve for κ_s/κ_n for a sample of RRR = 195 [3.16]. ——— gives the KM theoretical prediction for $\kappa^{el}{}_s/\kappa^{el}{}_s$ with $a_c = 0.22$ and $\Delta(0)/k_BT_c = 1.85$. ----- gives the BRT theoretical prediction for $\kappa^{el}{}_s/\kappa^{el}{}_n$ with $\Delta(0)/k_BT_c = 1.85$.

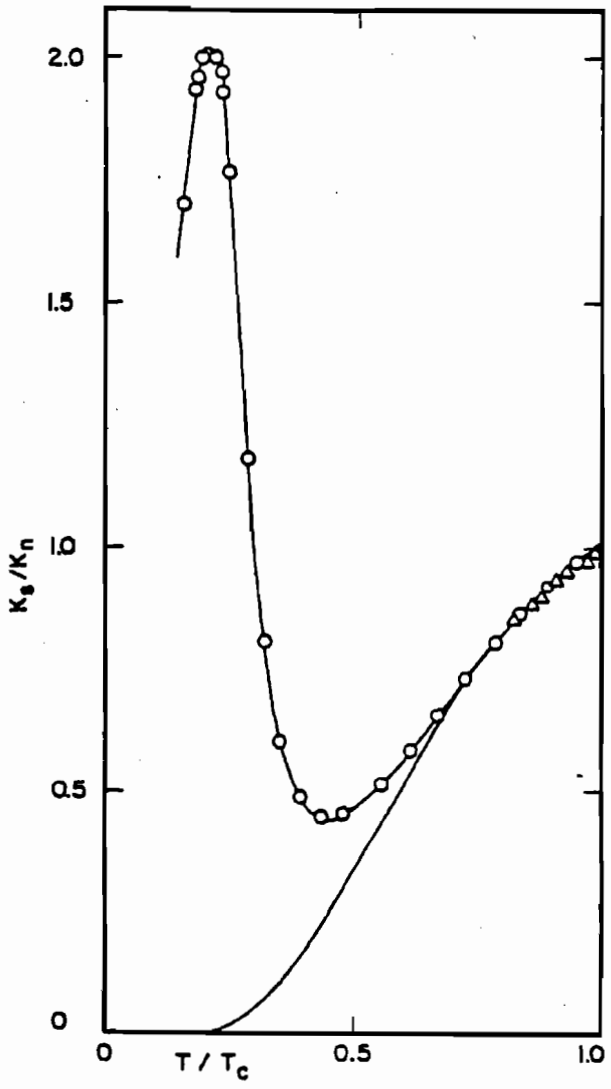

Figure 3.4c Measured curve for κ_s/κ_n for a sample of RRR = 21 [3.7]. The lower curve is the BRT theoretical calculation for $\kappa^{el}{}_s/\kappa^{el}{}_n$ with $\Delta(0)/k_BT_c$ = 1.90.

theory of Ambegaokar and Tewordt for strong coupling superconductors; hence Nb appears to exhibit behavior intermediate between that expected for weak and strong coupling superconductors. In conclusion, one should note that not all authors have actually computed the expected values for $\kappa_s^{el}/\kappa_n^{el}$ for their particular samples; those authors that have computed values for $\kappa_s^{el}/\kappa_n^{el}$ for their samples based on the theories discussed here have found reasonable agreement between their theoretical predictions and their experimental results for the electronic thermal conductivity of Nb in the superconducting state.

The thermal conductivity of Nb is also a function of the direction and magnitude of the applied magnetic field for magnetic fields above H_{c_1}; flux penetration into the superconductor leads to an increase in the electronic heat conduction because Cooper pairs are broken. Comprehensive experimental studies of the mixed state thermal conductivity of Nb have been performed by Kes et al. [3.7], Noto [3.15], Oota et al. [3.16], Schmidbauer et al. [3.19], Umlauf [3.19], Lowell and Sousa [3.22], and Wasim and Zebouni [3.23].

3.4 Lattice Thermal Conductivity

In the normal state the total thermal conductivity of Nb for $T \gtrsim 1K$ is entirely dominated by the electronic contribution; only in the superconducting state does the electronic thermal conductivity diminish sufficiently to allow measurement of the low temperature lattice thermal conductivity. The established theories for the electronic thermal conductivity in the superconducting state may be used to subtract the electronic contribution from the total measured thermal conductivity in the superconducting state to arrive at the lattice thermal conductivity in

the superconducting state.

Theoretical calculations of the low temperature lattice thermal conductivity in either the normal or superconducting states are difficult to perform. This is in part because many mechanisms may scatter phonons including point defects, dislocations, grain boundaries, sample walls, and electrons. (Phonon-phonon scattering is only important in non-metals.) Furthermore, the effectiveness of these various mechanisms in scattering phonons depends upon the phonon wavelength. Thus the lattice conductivity generally may not be computed using $\kappa = \frac{1}{3} C_v \times v^2 \times \tau$ where τ^{-1} is the total scattering rate of phonons from the different scattering mechanisms. Instead, the more general relationship must be used, giving

$$\kappa^{ph} = \frac{1}{3} \int \frac{C_v(\omega) \; v^2(\omega) \, d\omega}{\sum_{\substack{\text{scattering} \\ \text{mechanisms}}} \tau^{-1}(\omega)} \tag{3.9}$$

where $C_v(\omega)\, d\omega$ is the specific heat per unit volume for phonons of frequency ω. If the total scattering rate is independent of ω, then Eq. (3.9) simplifies to

$$\kappa^{ph} = \frac{1}{3} \times C_v \times v^2 \times \tau = \frac{1}{3} \times \frac{12\pi^4}{5} N k_B \times \left(\frac{T}{\theta_D}\right)^3 \times v^2 \times \tau \tag{3.10}$$

at low temperatures using the Debye model for the lattice specific heat [3.31], where N is the number of ions per unit volume in the crystal.

In the normal state at low temperatures the scattering of phonons by electrons is responsible for limiting the lattice thermal conductivity. The scattering rate of phonons by electrons at low temperatures should vary approximately as T since only a fraction T/T_{Fermi} of the total number of electrons are excited thermally. Thus when electron scattering dominates

the scattering of phonons, the lattice thermal conductivity should vary as $\kappa^{ph}_{electron} \propto T^2$. An actual estimate of $\kappa^{ph}_{electron}$ was performed by Klemens, who predicted that (see Reference [3.39], Eq. (15.4))

$$\kappa^{ph}_{electron} = 313 \times \kappa^{el}_{phonon} \times \left(\frac{T}{\theta_D}\right)^4 \times N_{eff}^{-4/3} \quad . \tag{3.11}$$

Using Eq. (3.5) again with $N_{eff} = 5$, $\theta_D = 275K$, and $\kappa_\infty = 0.6$ watt/cm-K gives $\kappa^{ph}_{electron} = 1.0\times10^{-6}T^2$ watt/cm-K^3; using the experimentally determined value for $\kappa^{el}_{phonon} = (0.6\times10^{-3})^{-1}T^{-2}$ watt-K/cm (Section 3.2) in Eq. (3.11) gives $\kappa^{ph}_{electron} = 1.1\times10^{-5}T^2$ watt/cm-K^3. According to Zimmerman [3.40], at very low temperatures $\kappa^{ph}_{electron}$ should become linear in T rather than quadratic in T; for Nb $\kappa^{ph}_{electron}$ should become linear in T for $T \lessapprox \rho_o/10$, where ρ_o is expressed in $\mu\Omega$-cm.

The phonon-electron scattering rate is lower in the superconducting state than in the normal state because the electrons condense into Cooper pairs that move cooperatively through the lattice. Bardeen, Rickayzen and Tewordt [3.35] have calculated $\kappa^{ph}_s/\kappa^{ph}_n$ when scattering of phonons by electrons dominates the lattice thermal resistivity. Their results are shown in Figure 3.5.

Experimental verification of these predictions for κ^{ph}_n and $\kappa^{ph}_s/\kappa^{ph}_n$ is difficult because κ^{ph}_n is only a very small part of the total normal state thermal conductivity at low temperatures. Thus one is most likely to be able to study κ^{ph}_n and κ^{ph}_s for relatively impure samples that have low electronic thermal conductivities in the normal state. By carefully analyzing their results for three fairly impure samples, Kes et al. [3.7] were able to compute κ^{ph}_n and κ^{ph}_s. They conclude that for their samples $\kappa^{ph}_{el,n} \approx (1\text{-}2)\times10^{-5}T^2$ watt/cm-K^3; in addition, their results for κ^{ph}_s gave

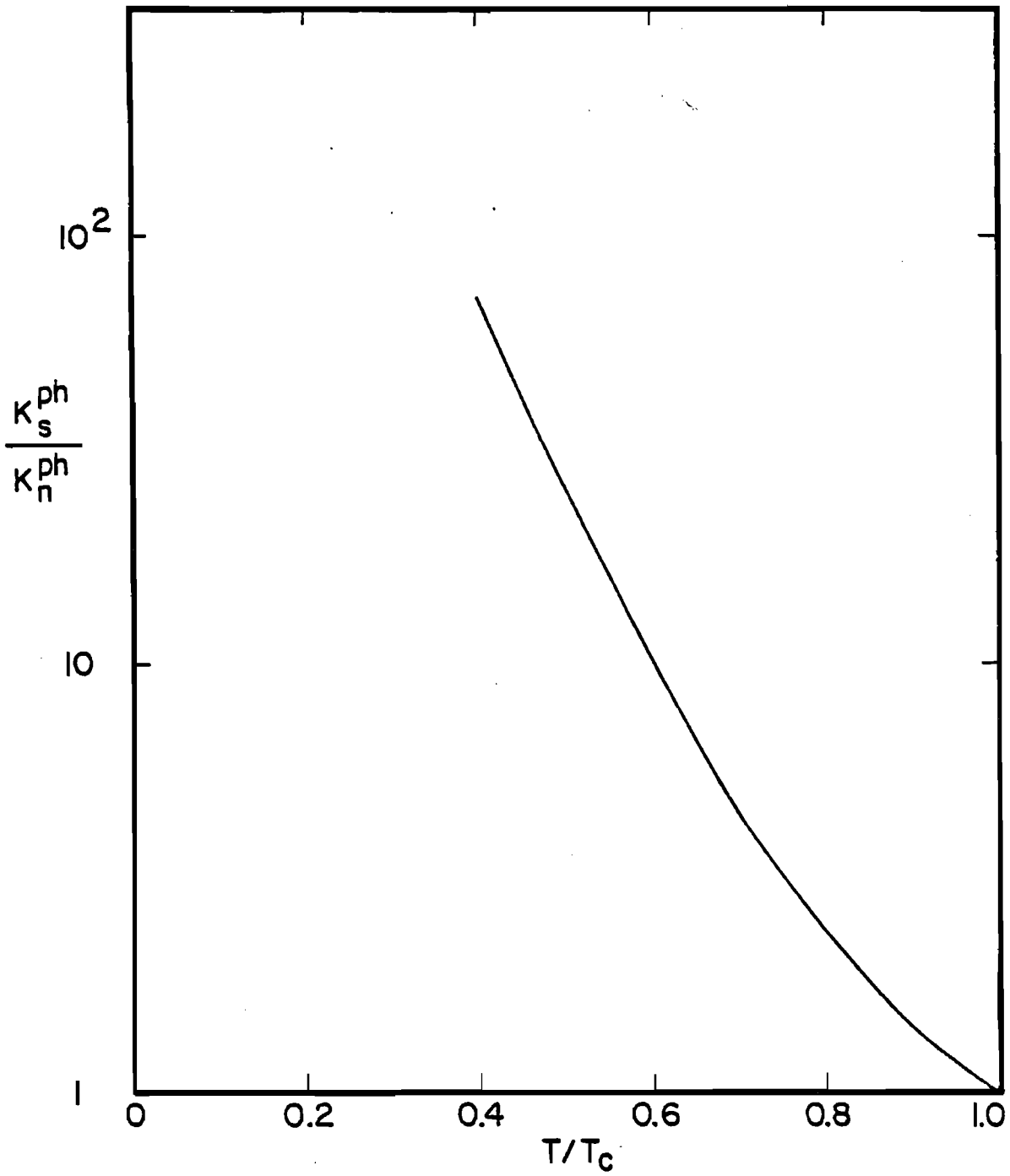

Figure 3.5 Theoretical predictions of Bardeen, Rickayzen, and Tewordt [3.35] for the ratio $\kappa^{ph}{}_s/\kappa^{ph}{}_n$ when electron scattering of phonons is predominant.

$\kappa_{el}^{ph},n \simeq (1\text{-}2)\times10^{-5}T^2$ watt/cm-K^3; in addition, their results for κ_s^{ph} give excellent agreement with the BRT theory for $\kappa_{el}^{ph},s/\kappa_{el}^{ph},n$ for $0.3 \lesssim T/T_c \lesssim 1$. Anderson and O'Hara [3.1] and Sousa [3.22] found that their results for κ_s^{ph} also gave excellent agreement with the BRT theory if they took $\kappa_n^{ph} = aT^2$ with $a = 3\text{-}4\times10^{-5}$ watt/cm-K^3. Thus κ_{el}^{ph},n is consistent with the prediction of Eq. (3.11) using the experimental value for $\kappa_{phonon}^{el}(T)$. Furthermore, the BRT theory for $\kappa_{el}^{ph},s/\kappa_{el}^{ph},n$ correctly describes the observed behavior of κ_{el}^{ph},s in the superconducting state above $\sim$2.8K. Thus one may conclude that scattering of phonons by electrons is responsible for the measured lattice thermal conductivity of Nb in the superconducting state for $2.8K \lesssim T \lesssim T_c$, and that below $\sim$2.8K other scattering mechanisms must also become important in scattering phonons.

The unusual behavior shown in Figures 3.2b and 3.2c for the thermal conductivity of Nb in the superconducting state for $2K \lessapprox T \lessapprox 4K$ may thus be explained as follows: as T falls well below T_c the electronic contribution to the thermal conductivity diminishes rapidly while the lattice contribution actually rises because the phonon-electron scattering rate is decreasing faster than the lattice specific heat. The very pure samples shown in Figure 3.2a do not demonstrate this rise in the thermal conductivity as T decreases because, for these samples, the electronic thermal conductivity is still important in this temperature range.

Scattering of phonons by defects, dislocations, grain boundaries and sample walls must be responsible for limiting the ability of the phonons to carry thermal energy at temperatures below $\sim$2.8K. Scattering of phonons by point defects such as impurities is insignificant for all of these samples. Kuhn [3.9] measured the thermal conductivity for a sample of Nb with $\rho(Rm.T)/\rho_o = 6$. Using the theory developed by Klemens

[3.39] for phonon-defect scattering, Kuhn predicted that phonon-defect scattering alone should give rise to a lattice thermal resistivity given by $W^{ph}_{defect} \simeq 3.5\times10^{-4}T$ cm/watt for this sample; this is five orders of magnitude below the lattice thermal resistivity measured by Kuhn for this sample. Clearly then phonon-defect scattering is not important as far as the low temperature lattice thermal conductivity of Nb in the superconducting state is concerned.

The remaining phonon scattering mechanisms, dislocations, sample boundaries and grain boundaries, are all significant in limiting the lattice thermal conductivity of Nb in the superconducting state below 2.8K. The expected lattice thermal resistivity due to each of these scattering mechanisms will be discussed first; then the experimental results will be compared with these predictions.

In the case where the static strain field associated with randomly distributed dislocations is the only important scattering mechanism, Klemens has predicted that (Reference [3.39], Eq. (11.3))

$$W^{ph}_{dislocation} = 2.4\times10^{-3}h^2 v \gamma^2 b^2 D T^{-2}/k_B^3 \qquad (3.12)$$

where γ is the Gruneisen parameter, b is the Burgers vector and D is the number of dislocations intersecting a unit area. Klemens also stated that the thermal resistivity is probably larger than his estimate by a factor of 15 or so ([3.39], page 92); in fact, the value frequently cited in the literature for $W^{ph}_{dislocation}$ is 15-16 times that of Eq. (3.12). Ackerman [3.41] has also argued that Klemens' result should be increased further by a numerical factor of 4.2. J. M. Ziman derived a result for $W^{ph}_{dislocation}$ identical to Eq. (3.12) except for an increase in magnitude

of $W^{ph}_{dislocation}$ by a factor of 17 ([3.33], Eq. (8.9.18)). Both Carruthers [3.42] and Ohashi [3.43] have also predicted that $W^{ph}_{dislocation} \propto DT^{-2}$; each of these calculations require knowledge of the anharmonic coefficient g (which is the third derivative of the unstrained lattice potential evaluated at the equilibrium nearest neighbor distance). Eckhardt and Wasserbach [3.44] also conclude that the scattering of phonons by the local strain field around a dislocation should give rise to a lattice thermal resistivity proportional to DT^{-2}. In addition, however, they predict that "global scattering" of phonons will also occur due to the spatial variation of the crystal orientation; the lattice thermal resistivity due to this global scattering is predicted to be proportional to T^{-3}. The relative importance of the local and global scattering of phonons depends upon the types of dislocations present in the sample. Finally, for very large dislocation densities, deviations from $W^{ph}_{dislocation} \propto DT^{-2}$ are expected at low temperatures when the average phonon wavelength becomes large compared to the average separation between the dislocations; according to Ackerman and Klemens [3.45], deviations from $W^{ph}_{dislocation} \propto DT^{-2}$ should occur for $T < 3\times10^{-6}\ D^{\frac{1}{2}}$ cm for Nb.

The lattice thermal conductivity at very low temperatures ultimately becomes limited by scattering of phonons at the sample walls: the scattering rate τ^{-1} decreases as the temperature falls until the phonon mean free path $v\tau$ becomes comparable to the size of the sample; the phonon mean free path will remain at a value approximately equal to the sample dimension as the temperature is lowered further due to scattering at the sample walls. In this case then $v\tau$ is constant and

$$\kappa^{ph}_{boundary} \simeq 1/3 \times C_v \times v \times (v\tau) \simeq 0.6 \times (v\tau) \times T^3 \text{ watt/cm}^2\text{-K}^4 , \qquad (3.13)$$

using Eq. (3.10) with $N = 0.54\times10^{23}$/atoms/cm^3, $v = 2.2\times10^5$ cm/sec [3.1], and $\theta_D = 275$K. Casimir [3.46] has treated this problem carefully for the case of diffuse boundary scattering in cubic crystals and gets this same result except for an increase in Eq. (3.13) of a factor of $3\pi/8$. Winternheimer and McCurdy [3.47] predict deviations of 10-20% in $\kappa^{ph}_{boundary}$ for Nb, depending upon the direction of the heat conduction in the crystal.

The final phonon scattering mechanism is grain boundary scattering. If grain boundaries limit the phonon mean free path in the same manner as sample boundaries then at very low temperatures

$$W^{ph}_{grain\,boundary} \propto T^{-3} \times (\text{grain boundary size})^{-1} \quad . \tag{3.14}$$

Alternatively, a grain boundary may be regarded as an array of dislocations, in which case

$$W^{ph}_{grain\,boundary} \propto T^{-2} \times (\text{grain boundary size})^{-1} \quad . \tag{3.15}$$

Klemens has estimated the magnitude of the thermal resistance in the case where grain boundaries are regarded as arrays of dislocations ([3.39], Eq. (5.29) gives the phonon lifetime τ for this case).

The experimentally observed behavior of the lattice thermal conductivity of Nb in the superconducting state at very low temperatures is summarized in Table 3.3; the lowest temperature measured, $T_{minimum}$, the functional form of $\kappa(T)$ at $T_{minimum}$, and the sample diameter (all these samples were cylindrical rods) are all recorded in Table 3.3; finally, the ratio of $\kappa(T)$ to the sample diameter is recorded in the last column of Table 3.3. At very low temperatures, $\kappa^{ph}(T)$ should be given by $\kappa(T) \cong 0.7 \times (\text{sample diameter}) \times T^3$ watt/cm^2-K^4 due to scattering of

Table 3.3 Superconducting State Lattice Thermal Conductivity of Nb at Very Low Temperatures

Ref.	Sample	$T_{minimum}$ K	$\kappa(T)$ at $T_{minimum}$ $\frac{watt}{cm/K}$, T in K	Sample Diameter cm	$\frac{\kappa(T) \text{ at } T_{minimum}}{\text{Sample Diameter}}$ $\frac{watt}{cm^2-K}$, T in K
[3.1]	A*	∿.045	$.19T^{2.9}$	.30	$.63T^{2.9}$
[3.1]	B*	∿.045	$.18T^{2.8}$	.46	$.39T^{2.8}$
[3.1]	C*	∿.045	$.19T^{2.7}$	.64	$.30T^{2.7}$
[3.1]	D*	∿.045	$.17T^{2.9}$	.32	$.53T^{2.9}$
[3.6]	Nb*	.05	$\sim.15T^{2.7}$	.41	$\sim.37T^{2.7}$
[3.2]	Nb-outgassed*	.10	$\sim.20T^{2.6}$	1.1	$\sim.18T^{2.6}$
[3.2]	H added*	.05	$\sim.017T^{2.4}$	1.1	$\sim.015T^{2.4}$
[3.2]	D added*	.05	$.022T^{2.6}$	1.1	$.020T^{2.6}$
[3.10]	Nb III	.25	$.047T^{2.5}$	.22	$.21T^{2.5}$
[3.10]	Nb II	.26	$.020T^{2.5}$	.40	$.050T^{2.5}$
[3.24]		.3	$.090T^{2.9}$	.30	$.30T^{2.9}$
[3.25]	NbH2 unstrained	.3	$.29T^{2.95}$	.32	$.91T^{2.95}$
[3.25]	NbH2-8% strain	.3	$.011T^{2.1}$	.32	$.034T^{2.1}$
[3.25]	NbH1 unstrained	.3	$.088T^{2.8}$	.32	$.28T^{2.8}$
[3.25]	NbH1-8% strain	.3	$.032T^{2.9}$	.32	$.10T^{2.9}$
[3.25]	NbK6 unstrained	.3	$.15T^{2.7}$	.39	$.38T^{2.7}$
[3.25]	NbK6-15% strain	.3	$.0069T^{2.1}$	.39	$.018T^{2.1}$
[3.25]	NbK10 unstrained	.3	$.12T^{2.9}$	.40	$.30T^{2.9}$
[3.25]	NbK10-22% strain	.3	$.0030T^{2.0}$	.40	$.0075T^{2.0}$
[3.12]	Cb 1	.4	$\sim.015T^{3}$	.47	$\sim.03T^{3}$
[3.10]	Nb I unstrained	1.0	$.0089T^{3.0}$	--	$\propto T^{3}$

Table 3.3 (continued)

Ref.	Sample	$T_{minimum}$	$\kappa(T)$ at $T_{minimum}$	Sample Diameter	$\frac{\kappa(T) \text{ at } T_{minimum}}{\text{Sample Diameter}}$
		K	$\frac{watt}{cm/K}$, T in K	cm	$\frac{watt}{cm^2-K}$, T in K
[3.10]	Nb I-5% strain	1.0	$.0062T^{2.7}$	--	$\propto T^{2.7}$
[3.10]	Nb I-13% strain	1.0	$.0045T^{2.4}$	--	$\propto T^{2.4}$
[3.10]	Nb I-20% strain	1.0	$.0037T^{2.35}$	--	$\propto T^{2.35}$

*Surface sandblasted

phonons at the sample walls. From the results given in Table 3.3 it appears that at temperatures below $\sim$0.3K $\kappa(T)$ approached the boundary scattering limit for the unstrained samples. The effect of deliberately straining a sample was to lower the magnitude of $\kappa(T)$ and change the temperature dependence of $\kappa(T)$ to T^n where n approached 2 for the severely strained samples. Thus dislocations were probably responsible for limiting the lattice thermal conductivity to values below the sample boundary scattering limit.

Additional measurements relevant to understanding boundary scattering of phonons were performed by Anderson and Smith [3.1] and Gladun et al. [3.6]. Anderson and Smith compared the lattice thermal conductivity of samples with sandblasted surfaces and surfaces that were subsequently electropolished. The sandblasted samples exhibited a low temperature thermal conductivity in the superconducting state that, as reported in Table 3.3, approached the boundary scattering limit below $\sim$0.1K; after electropolishing the samples exhibited an increased thermal conductivity given by $\kappa_s^{ph}(T) \propto T^n$ where $n \lesssim 2.5$. Gladun et al. also observed this effect before sandblasting their sample. The prediction that at very low temperatures $\kappa(T) \propto T^3$ was based upon the assumption of completely diffuse surface scattering; in the case of some specular reflection the phonon mean free path may increase beyond the sample diameter, which causes $\kappa_s^{ph}(T)$ to decrease more slowly than as T^3 as the temperature is lowered. In summary, the boundary scattering regime of the low temperature lattice thermal conductivity of Nb in the superconducting state is approached at very low temperatures, which are of the order of 0.1K for the unstrained, sandblasted samples reported in Table 3.3.

For the monocrystalline samples, the observed behavior of the lattice thermal conductivity in the superconducting state between $\sim$0.1K and 2.8K arises from phonon-dislocation scattering. Mendelssohn [3.10] studied the effect of deliberately straining a Nb specimen by three increasing amounts: the additional thermal resistance after straining was found to obey $W^{ph} \propto T^{-2}$; the absolute magnitude of this additional thermal resistance was proportional to the calculated increase in the dislocation density based upon the applied strain. Thus the lattice thermal resistivity due to dislocation scattering is indeed proportional to DT^{-2}. The various predictions for the magnitude of $W^{ph}_{dislocation}$ may be compared with measurements made by Kuhn [3.9] for six monocrystalline samples with measured dislocation densities ranging from $D = 1.2\times10^{9}$ cm^{-2} to $D = 23\times10^{9}$ cm^{-2}; Kuhn found that

$$W^{ph}_{s}(1.46K) = (0.59\text{-}0.63)\times10^{-8} D \frac{cm^3\text{-}K}{watt} . \qquad (3.16)$$

The various predictions for $W^{ph}_{dislocation}$ will be evaluated here for Nb. The prediction of Klemens, according to Eq. (3.12), gives

$$W^{ph}_{dislocation}(T) = 1.9\times10^{-10} T^{-2} D \frac{cm^3\text{-}K^3}{watt}. \qquad (3.17)$$

(taking b = 3.3Å and γ = 1.4 as given by Kes et al. [3.7], and $v = 2.2\times10^{5}$ cm/sec). Therefore Klemens' calculation gives

$$W^{ph}_{dislocation}(1.46K) = 0.89\times10^{-10} D \frac{cm^3\text{-}K}{watt} .$$

Ziman's prediction for $W^{ph}_{dislocation}$ is 17 times that given by Eq. (3.17). Carruthers' and Ohashi's predictions for $W^{ph}_{dislocation}$ for Nb are 0.6 and 450 times that given by Eq. (3.17) (using Eq. (4.70) of Carruthers [3.42] and Eq. (35b) of Ohashi [3.43] with $g = C_{111}$ [3.43], $C_{111} \simeq 25\times10^{12}$ dynes/cm^2, $C_{11} \approx 2.4\times10^{12}$

dynes/cm^2 and $\beta = 1\text{-}2\sigma/1\text{-}\sigma \approx 0.342$ for Nb, using the value for Poisson's ratio σ of 0.397 [3.48]). Finally, Wasserbach's [3.25] calculation for edge dislocations accumulated in bundles gives a value for $W^{ph}_{dislocation}$ that is 36 times that of Eq. (3.17).

These theoretical predictions may be compared with the measurements of Kuhn (Eq. (3.16)) as follows: the formula of Klemens given in Eq. (3.17) underestimates the strength of the phonon-dislocation scattering for Nb by a factor of $\sim$70; adjusting Klemens' prediction for $W^{ph}_{dislocation}$ as given in Eq. (3.12) by a factor of 15×4.2 as discussed earlier gives good agreement with experiment. Wasserbach's prediction is also in reasonable agreement with Eq. (3.16). Ziman's prediction underestimates $W^{ph}_{dislocation}$ by a factor of 4. Carruthers' prediction underestimates $W^{ph}_{dislocation}$ by a factor of $\sim$100. Finally, Ohashi's prediction overestimates $W^{ph}_{dislocation}$ by a factor of 7.

In addition to the measurements of Kuhn given by Eq. (3.16), Wasserbach [3.25] has carefully studied the effects of deformation on the lattice thermal resistivity. Wasserbach deformed four samples by increasing amounts; different types and arrangements of dislocations were produced by straining each sample at a different temperature ranging from 77-470K. Wasserbach observed that $W^{ph}_{dislocation} \propto T^{-3}$ for those samples that were deformed weakly at low temperatures; these samples had low densities of long screw dislocations; both the magnitude and temperature dependence of $W^{ph}_{dislocation}$ were consistent with Eckhardt and Wasserbach's predictions for global scattering of phonons. Strong deformation at low temperatures, or deformation at high temperatures led to $W^{ph}_{dislocation} \propto T^{-2}$; these samples had bundles of edge dislocations;

furthermore, the magnitudes of $W^{ph}_{dislocation}$ were in agreement with the theory of Eckhardt and Wasserbach. In conclusion, the scattering of phonons by dislocations is important in limiting $\kappa^{ph}(T)$ for monocrystalline Nb between ~0.1-3K: the results of Wasserbach indicate that global scattering giving $W^{ph}_{dislocation} \propto T^{-3}$ is important for weakly deformed Nb; for larger densities of dislocations scattering by the local strain field around the dislocation gives rise to $W^{ph}_{dislocation} \propto T^{-2}$.

The final mechanism for scattering of phonons is grain boundaries. The measurements of Kes et al. [3.7] on three polycrystalline samples may be used to study the grain boundary scattering of phonons. Table 3.4 summarizes the properties of their samples, including the measured dislocation densities and grain sizes. Table 3.4 also includes the dislocation thermal resistivities estimated from the measurements of Kuhn (Eq. (3.16)); the estimated values for $W^{ph}_{dislocation}$ (1.46K) are much smaller than the measured values of W (1.46K) demonstrating that dislocations were not responsible for limiting the lattice thermal conductivity for these samples. Hence grain boundary scattering must have limited the lattice thermal conductivity. The analysis performed by Kes et al. indicates that grain boundaries scatter like an array of dislocations: they were able to fit their measured curves for $\kappa^{ph}_s(T)$ between 1-9.2K assuming only phonon-electron scattering and phonon-dislocation scattering in evaluating Eq. (3.9) for $\kappa^{ph}_s(T)$. Assuming that grain-boundary scattering limits the phonon mean free path to the grain dimension led to theoretical curves that did not fit the data for $\kappa^{ph}_s(T)$ well. These results of Kes et al. demonstrate that grain boundaries scatter phonons as if they were arrays of dislocations.

Table 3.4 Low Temperature Lattice Thermal Resistivity of Kes et al.'s [3.7] Polycrystalline Samples

Sample	Dislocation density	Grain size	$W^{ph}_{measured}(1.46K)$	$W^{ph}_{dislocation}(1.46K)$ Eq. (3.16)	$W^{ph}_{grain\ boundary}(1.46K)$ Eq. (3.19)
	cm^{-2}	cm	cm-K/watt	cm-K/watt	cm-K/watt
N-0	$<4\times10^{7}$	.0400	11	.24	.050
P1600	$<5\times10^{7}$	.0350	12	.30	.057
P1400	6×10^{8}	.0090	75	3.6	.22

Kes et al. found that the magnitude of the grain boundary scattering was much larger than that predicted by Klemens. Klemens' theory gives

$$\frac{W^{ph}_{\text{grain boundary}}}{W^{ph}_{\text{dislocation}}} = \frac{\alpha/b}{0.55}\frac{G}{D}$$

where α is the angle of tilt of the crystal lattices separated by the grain boundary and G is the number of grain boundaries intersecting a unit length of line (see Reference [3.39], Eqs. (5.25) and (5.29) for the phonon lifetimes τ for each case; this relation includes a factor of 0.55 for randomly oriented dislocations and assumes that $d = b/\alpha$). Using Eq. (3.17) for $W^{ph}_{\text{dislocation}}$ with $\alpha = \pi/8$ and $b = 3.3\text{Å}$ gives

$$W^{ph}_{\text{grain boundary}} = 0.42\times10^{-2}\, G\, T^{-2}\ \frac{\text{cm}^2\text{-K}^3}{\text{watt}}\ . \qquad (3.18)$$

Therefore according to Klemens

$$W^{ph}_{\text{grain boundary}}\ (1.46\text{K}) = 2.0\times10^{-3}\, G\ \frac{\text{cm}^2\text{-K}}{\text{watt}}\ . \qquad (3.19)$$

The expected values for $W^{ph}_{\text{grain boundary}}$ (1.46K) for Kes et al.'s samples computed from Eq. (3.19) are recorded in Table 3.4. These values are all low by a factor of 200-300 when compared with the measured values of W^{ph} (1.46K). However, Klemens' formula for $W^{ph}_{\text{dislocation}}$ given in Eq. (3.17) was found to be lower than the experimental results by a factor of $\sim$70, so that Eq. (3.18) for $W^{ph}_{\text{grain boundary}}$ might also be expected to be low by a factor $\sim$100. In conclusion, Eq. (3.18) gives the correct temperature dependence but underestimates the magnitude of the lattice thermal resistivity due to grain boundary scattering.

In summary, the behavior of $\kappa^{ph}_s(T)$ of Nb may be explained in terms

of the scattering of phonons by electrons, dislocations, grain boundaries and sample boundaries. As T falls below around 3K the thermal resistivity due to phonon-electron scattering decreases rapidly; dislocations and grain boundaries give rise to a thermal resistivity increasing as T^{-2} as T decreases, and cause $\kappa_s^{ph}(T)$ to decrease at temperatures below around 2K. The sample boundary thermal resistivity increases as T^{-3} and becomes significant as the temperature is lowered below 0.1-0.5K.

Thus the physics underlying the measured low temperature thermal conductivity of Nb in the superconducting state may be understood as follows: for very pure Nb the thermal conduction is due to the electrons; the thermal conductivity decreases rapidly with decreasing temperature as the electrons condense into Cooper pairs. For most Nb, the thermal conduction is due to the electrons above about 3K; below about 3K lattice heat conduction is responsible for the measured thermal conductivity, as summarized in the preceding paragraph.

References for Chapter 3

[3.1] A. C. Anderson and S. C. Smith, J. Phys. Chem. Solids 34, 111 (1973); A. C. Anderson and S. G. O'Hara, J. Low Temp. Phys. 15, 323 (1974); A. C. Anderson, C. B. Satterthwaite, and S. C. Smith, Phys. Rev. 133, 3762 (1971); J. R. Carlson and C. B. Satterthwaite, Phys. Rev. Lett. 24, 461 (1970).

[3.2] S. G. O'Hara, G. J. Sellers, and A. C. Anderson, Phys. Rev. B10, 2777 (1974).

[3.3] H. Brechna, Office Memorandum, Stanford University (1969).

[3.4] K. D. Chauduri, K. Mendelssohn, and M. W. Thompson, Cryogenics 1, 47 (1960).

[3.5] C. D. Eger, Thesis, TU Dresden (1975); reported in [3.6].

[3.6] A. Gladun, C. Gladun, M. Knorn and H. Vinzelberg, J. Low Temp. Phys. 27, 873 (1977).

[3.7] P. H. Kes, J. G. A. Rolfes, and D. deClerk, J. Low Temp. Phys. 17, 341 (1974); P. H. Kes, J. O. M. VanderVeeken, and D. deClerk, J. Low Temp. Phys. 18, 355 (1975).

[3.8] M. Klauss, Dissertation A, TU Dresden (1978); reported in [3.18].

[3.9] G. Kuhn, Comm. Energie At. (France) Rappt. CEA-R2808 (1966) (available on microfiche); B. B. Goodman and G. Kuhn, J. Physique Series 8, Vol. 29, 240 (1968); G. Kuhn, Comptes Rend. 255, 2923 (1962).

[3.10] K. Mendelssohn, Physica 24, Kamerlingh Onnes Conference, Leiden, page S53 (1958); P. M. Rowell, Proc. Roy. Soc. (London) A254, 542 (1960); A. Calverly, K. Mendelssohn, and P. M. Rowell, Cryogenics 2, 26 (1961); A. Connolly and K. Mendelssohn, Proc. Roy. Soc. (London) 266A, 429 (1962).

[3.11] K. Mendelssohn and J. Olsen, Proc. Phys. Soc. (London) A63, 2 (1950).

[3.12] K. Mendelssohn and H. Rosenberg, Proc. Phys. Soc. (London) A65, 388 (1952); K. Mendelssohn and C. A. Renton, Phil. Mag. Series 7, Vol. 44, 776 (1953); K. Mendelssohn and C. A. Renton, Proc. Roy. Soc. (London) A230, 157 (1955); H. M. Rosenberg, Phil. Trans. Roy. Soc. (London) A247, 441 (1955).

[3.13] B. A. Merisov and V. I. Khotkevich, Phys. Metals and Metallography 26, No. 2, 182 (1969) [transl. from Russian]; B. A. Merisov, V. I. Khotkevich, G. Zlobintsev, and V. V.

Kozinets, J. Engr. Phys. 12, 364 (1967) [transl. from Russian].

[3.14] K. Mittag, Cryogenics 13, 94 (1973).

[3.15] Y. Muto, K. Noto, and T. Fukuroi, Proc. 11th Intnl. Conf. Low Temp. Phys., Vol. 2, pg. 930 (St. Andrews, 1968); K. Noto, J. Phys. Soc. Japan 26, 710 (1969); Y. Muto, K. Noto, T. Mamiya, and T. Fukuroi, J. Phys. Soc. Japan 23, 130 (1967).

[3.16] A. Oota and Y. Masuda, J. Phys. Soc. Japan 41, 434 (1976); T. Mamiya, A. Oota, and Y. Masuda, Sol. St. Commun. 15, 1689 (1974); A. Oota, T. Mamiya, and Y. Masuda, J. Phys. Soc. Japan 38, 1362 (1975); A. Oota, T. Mamiya, and Y. Masuda, Proc. XIVth Intnl. Conf. Low Temp. Phys., Pt. II, pg. 329 (Finland, August 1975).

[3.17] L. Phillips, Laboratory of Nuclear Studies, Cornell University, private communication.

[3.18] K. Reiche and G. Pompe, J. Low Temp. Phys. 36, 467 (1979).

[3.19] E. Schmidbauer, H. Wenzl, and E. Umlauf, Z. Physik 240, 30 (1970); E. Umlauf, Z. Physik 206, 415 (1967).

[3.20] C. Schmidt, Phys. Rev. B15, 4187 (1977).

[3.21] C. Schmidt, J. Appl. Phys. 46, 1372 (1975).

[3.22] J. B. Sousa, J. Phys. C, Series 2, Vol. 2, 629 (1969); J. B. Sousa, Phys. Lett. 26A, 607 (1968); J. Lowell and J. B. Sousa, J. Low Temp. Phys. 3, 65 (1970); J. Lowell and J. B. Sousa, Phys. Lett. 26A, 480 (1968); J. Lowell and J. B. Sousa, Phys. Lett. 25A, 469 (1967).

[3.23] S. M. Wasim and N. H. Zebouni, Phys. Rev. 187, 539 (1969).

[3.24] W. Wasserbach, Phys. Stat. Sol. B84, 205 (1977).

[3.25] W. Wasserbach, Phil. Mag. A, 38, 401 (1978).

[3.26] G. K. White and S. B. Woods, Can. J. Phys. 35, 892 (1957).

[3.27] G. Cannelli and G. B. Cannelli, J. Appl. Phys. 47, 17 (1976).

[3.28] L. F. Mattheis, Phys. Rev. B1, 373 (1970).

[3.29] G. Webb, Phys. Rev. 181, 1127 (1969).

[3.30] N. Y. Alekseyevski, V. I. Nizhankovskiy, and K.-H. Berthel, Phys. Metals and Metallography 42, No. 5, 25 (1976) [transl. from Russian].

[3.31] N. W. Ashcroft and N. D. Mermin, Solid State Physics, Holt, Rinehart, and Winston, NY, 1976.

[3.32] C. Kittel, Introduction to Solid State Physics, John Wiley and Sons, NY, 4th edition, 1971.

[3.33] J. M. Ziman, Electrons and Phonons, Oxford University Press, London, 1960.

[3.34] V. Yu. Voskresenskii, V. E. Peletski, and D. L. Timrot, High Temp. 4, 39 (1966).

[3.35] J. Bardeen, G. Rickayzen, and L. Tewordt, Phys. Rev. 113, 982 (1959).

[3.36] L. P. Kadanoff and P. C. Martin, Phys. Rev. 124, 670 (1961).

[3.37] L. Tewordt, Phys. Rev. 128, 12 (1962); L. Tewordt, Phys. Rev. 129, 657 (1963).

[3.38] V. Ambegaokar and L. Tewordt, Phys. Rev. 134, A805 (1964).

[3.39] P. G. Klemens, Solid State Physics 7, 1 (1958).

[3.40] J. E. Zimmerman, J. Phys. Chem. Solids 11, 299 (1959).

[3.41] M. W. Ackerman, Phys. Rev. B8, 2751 (1972).

[3.42] P. Carruthers, Rev. Mod. Phys. 33, 92 (1961).

[3.43] K. Ohashi, J. Phys. Soc. Japan 24, 437 (1968).

[3.44] D. Eckhardt and W. Wasserbach, Phil. Mag. A37, 621 (1978).

[3.45] M. W. Ackerman and P. G. Klemens, Phys. Rev. B3, 2376 (1971).

[3.46] H. B. G. Casimir, Physica 5, 495 (1938).

[3.47] C. Winternheimer and A. K. McCurdy, Sol. St. Commun. 14, 919 (1974).

[3.48] L. J. Graham, H. Nadler, and R. Chang, J. Appl. Phys. 39, 3025 (1968).

Chapter 4

HEAT TRANSPORT ACROSS THE METAL TO LIQUID HELIUM INTERFACE

4.1 Introduction

Heat transport across an interface between two dissimilar materials results in a temperature drop across the interface; this is referred to as the thermal boundary resistance at the interface. The temperature drop across a metal to liquid He I interface is primarily determined by the properties of the liquid helium. Heat transport to superfluid He II is unlike heat transport to most cryogenic liquids because of the very high effective thermal conductivity of superfluid He II. Experimentally, the temperature drop due to heat transport across a metal to He II interface depends on the properties of the metal, the conditions at the metal surface, and the temperature of the He II. The theoretical understanding of the physics of heat transport across a metal to He II interface remains an unsolved problem, although this temperature drop was first measured by Kapitza in 1941 [4.1]. Finally, at very high heat fluxes so-called film boiling occurs in both He I and He II, where the entire surface is covered with a film of vapor; this results in a very high thermal boundary resistance.

The discussion in this chapter will be brief, as several review articles are available. Johannes [4.2], R. V. Smith [4.3], and Lyon [4.4] have reviewed heat transport to He I; Van Sciver [4.5] and Frederking [4.6] have reviewed heat transport to He II; Challis [4.7], Snyder [4.8], and Pollack [4.9] have also reviewed heat transport to He II at low heat fluxes (the so-called Kapitza regime).

Measurements of heat transport to liquid helium are not reproducible because the condition of the surface affects the results. This fact has

two important consequences: first, study of the physics of heat transport across an interface is very difficult; in addition, the thermal boundary resistance must be measured whenever heat transport to liquid helium is an important factor in understanding the performance of an experimental apparatus.

4.2 Heat Transport Across the Metal to Liquid Helium I Interface

Figure 4.1 illustrates a typical curve for heat transport from a horizontal flat platinum surface immersed in a pool of liquid helium which is maintained at constant temperature by the evaporation of the liquid helium [4.10]; the heat flux Q/A is plotted against the temperature drop ΔT across the interface. Two different regimes of heat transport are shown. First, for ΔT below about one degree nucleate pool boiling occurs; in this regime bubbles of helium vapor form at nucleation sites on the surface and carry heat away. The maximum flux that may be sustained in the nucleate pool boiling regime is called the peak nucleate boiling flux (PNBF) or film boiling limit. As the flux increases above the PNBF then the film boiling regime is entered; in this regime the entire surface is coated with a vapor film, and ΔT increases to above 10K. On lowering the heat flux the crossover from film boiling to nucleate boiling does not occur until ΔT has fallen to about 2K, as shown in Figure 4.1. The PNBF is very important in the design of superconducting devices; most superconducting materials become normal conducting when the PNBF is exceeded since ΔT rises above 10K.

A third regime for heat transport to He I is observed at very low heat fluxes. Measurements by Tsuruga and Endoh [4.11] and Verkin et al.

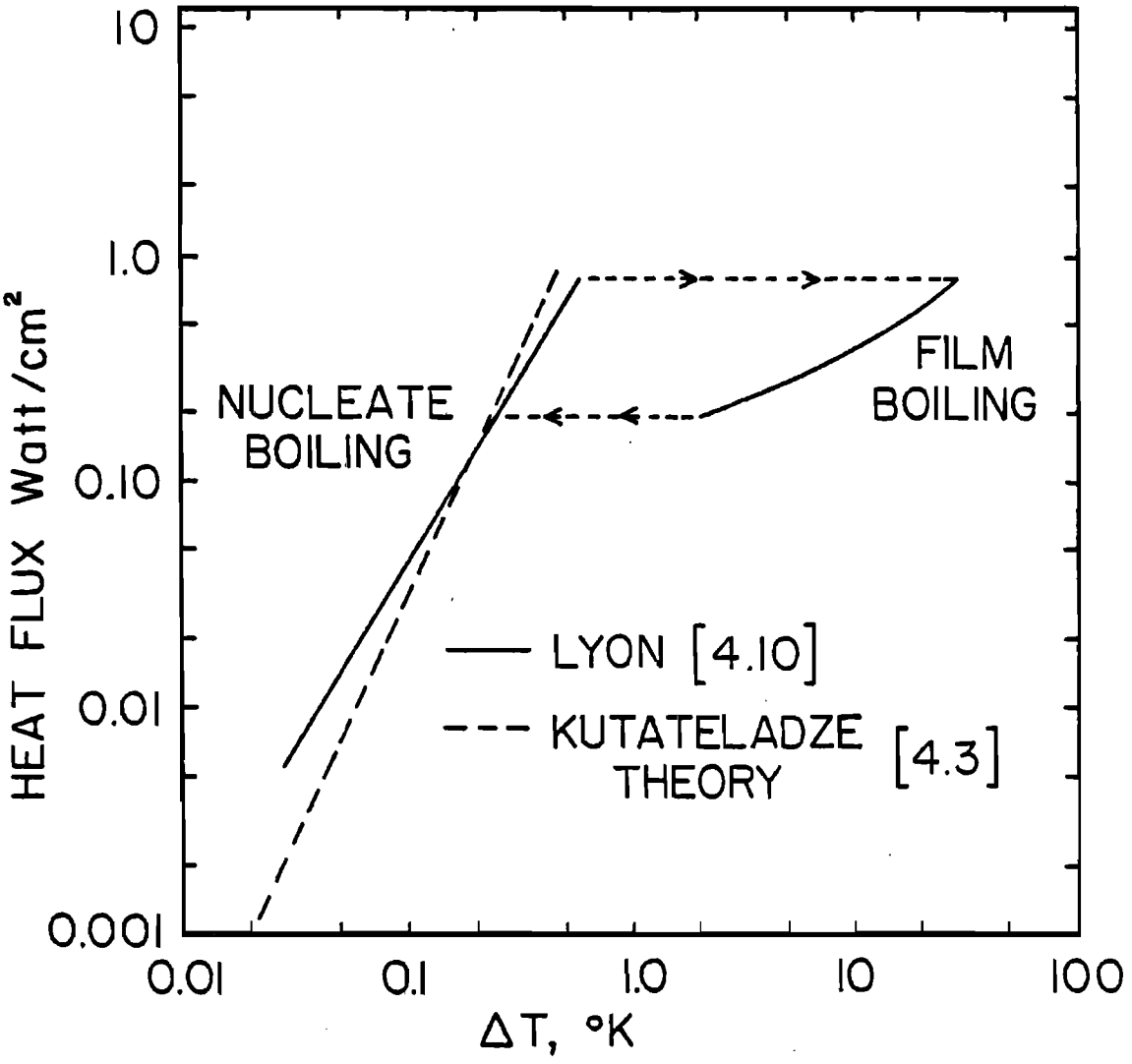

Figure 4.1 Heat flux versus ΔT for horizontal flat platinum in He I at 4.2K.

[4.12] indicate that free convention takes place in He I for heat fluxes below 0.001 watt/cm^2. The heat flux in this regime is considerably lower if the liquid helium is subcooled (maintained at a temperature below the saturation temperature corresponding to the vapor pressure above the liquid).

Measurements in the steady state nucleate boiling regime are usually found to follow an equation of the form

$$Q/A = C \times (\Delta T)^n.$$

The exponent n ranges from 1.4 to 2.0 for most measurements [4.2-4.4, 4.10-4.11, 4.13-4.14]; the value of the constant C is typically of the order of one watt/cm^2. The constant C and the exponent n depend only weakly upon the temperature of the liquid helium for a given experimental data run: n is generally independent of the liquid helium temperature while the value of the constant C decreases by a factor of 2 to 5 between 4.2K and the superfluid transition at 2.17K (the lambda point).

The range of measured values in the nucleate boiling regime is fairly large; Figure 4.2 illustrates the range of measurements on flat horizontal copper surfaces (from [4.15]). Several factors have been shown to affect the nucleate boiling curve. Hysteresis may significantly influence results in the nucleate boiling regime; a rapid increase in heat flux is found to cause a much higher ΔT than is measured in the steady state [4.3,4.10, 4.13]. The nucleate boiling curve also depends upon the surface material, sample geometry, and orientation. The nucleate boiling curve is particularly sensitive to the surface finish: surface roughness, contamination, coatings, chemical treatment, etc. all affect the nucleate boiling curve. Measurements by Cummings and Smith [4.13] indicate that the heat flux for

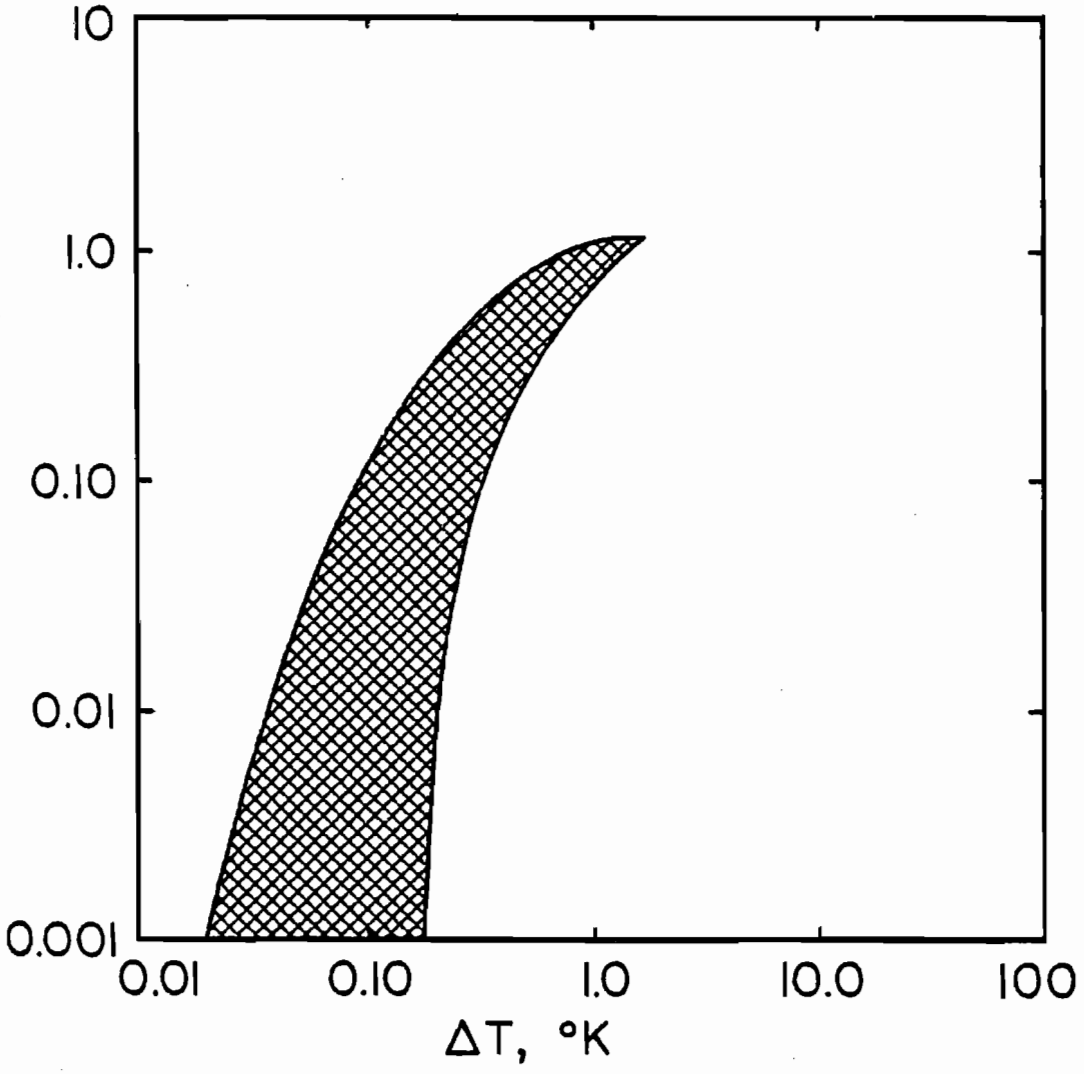

Figure 4.2 Heat flux versus ΔT for horizontal flat copper surfaces in He I at 4.2K; nucleate boiling regime (from [4.15]).

a mirror finish surface is up to a factor of ten lower than for a rough surface. The influence of all of these factors means that accurate predictions for the nucleate boiling curve for a given sample may not be made on the basis of results in the literature.

Figure 4.3 shows measurements by Lyon of the PNBF versus the temperature of the liquid He I [4.10]. The PNBF was found to rise as the helium temperature was lowered from 5.2K, where liquid helium first condenses at about 2 atmospheres of pressure; the PNBF peaked and then fell as the temperature approached the superfluid transition at 2.17K. The PNBF depends upon the sample shape and orientation. Lyon found that the PNBF decreased as the surface was rotated from the horizontal position. Johannes [4.2] found that the PNBF for a vertical sample decreased with the height of the sample; bubbles leaving the lower portion of the sample are transported to the upper portion and lower the heat transport there. However, Goodling and Irey [4.14] found no depth effect for a horizontal surface. In general, the PNBF is much less sensitive than the nucleate boiling curve to changes in the state of the surface: the PNBF does vary somewhat with the composition of the surface [4.13]; surface roughness did not change the PNBF in the measurements by Cummings and Smith [4.13]. Cummings and Smith found that PNBF increased somewhat if the surface was contaminated although Lyon [4.4] did not observe this effect. Both Cummings and Smith, and Lyon did find that the transition region to film boilding was much smoother when the surface was contaminated; the heat transport curve was continuous with an inflection at the PNBF.

The nucleate boiling regime in He I is described reasonably well by the Kutateladze correlation for boiling fluids, as shown in Figure 4.1.

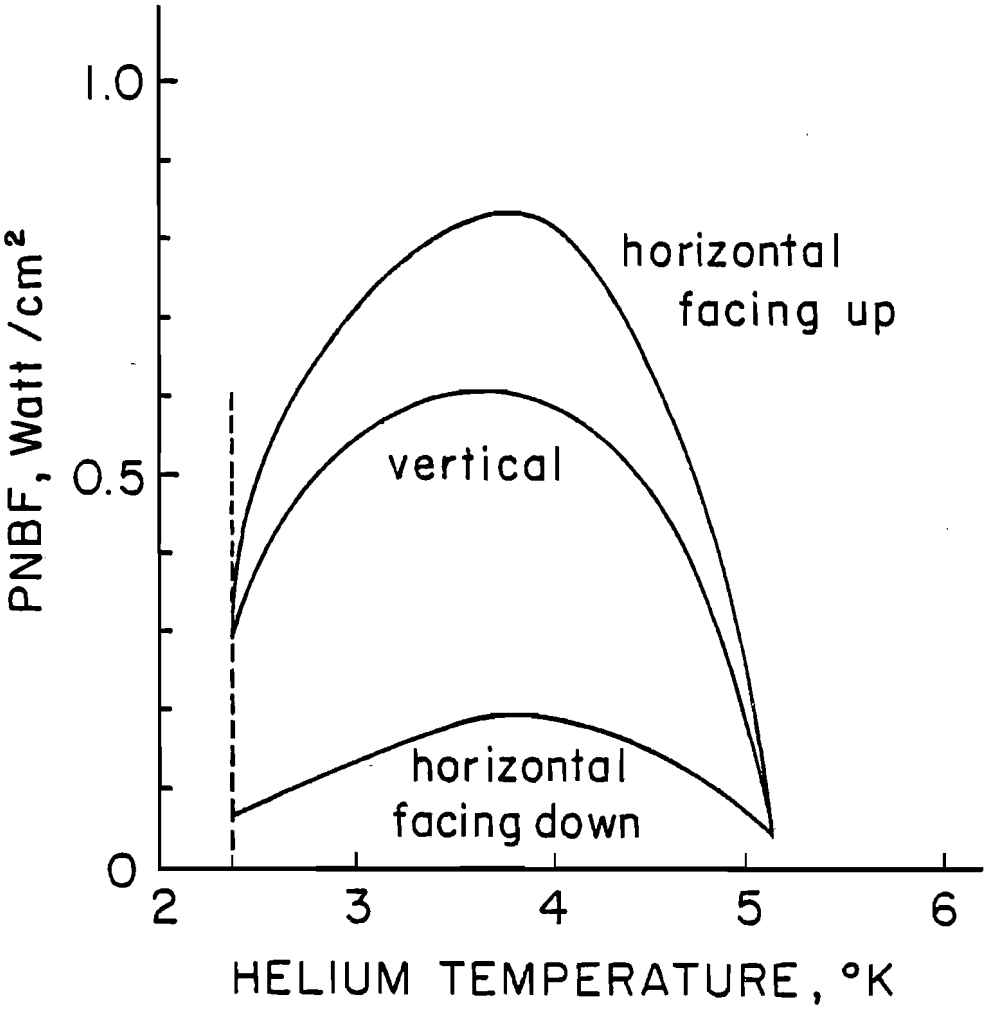

Figure 4.3 Peak nucleate boiling flux for flat polished platinum in He I (from [4.10]).

As described by R. V. Smith [4.3] this correlation depends upon a number of temperature dependent hydrodynamic and thermodynamic properties of the fluid; the gravitational constant g, the densities of the fluid and vapor, the viscosity of the fluid, the thermal conductivity and specific heat of the fluid, the latent heat of vaporization, and the surface tension between the liquid and vapor all enter into the Kutateladze correlation. In addition, R. V. Smith gives a simplified version of an expression developed by Kutateladze to predict the maximum flux in the nucleate boiling regime; this expression successfully describes the temperature dependence of the PNBF measured by Lyon and other researchers for helium temperatures below 4.5K [4.3].

The film boiling regime in He I is described reasonably well by several correlations developed to describe film boiling in cryogenic fluids; these correlations depend upon the same parameters used to describe nucleate boiling in cryogenic liquids (see Smith [4.3] and Lyon [4.4]).

4.3 Heat Transport Across the Metal to Superfluid Helium II Interface

Cooling by superfluid He II is more effective than cooling by He I; hence He II is generally used in superconducting devices in spite of the additional refrigeration costs. Figure 4.4 illustrates a typical curve for heat transport from a horizontal flat platinum surface immersed in He II at 2.07K [4.10] (the measurements for this same sample in He I are shown in Figure 4.1). Two regimes of heat transport are observed in He II. First, for ΔT below 2K, heat transport occurs by free convection in the He II; nucleate boiling is not observed in He II. The free convection regime is also referred to as the Kapitza conduction regime. Film

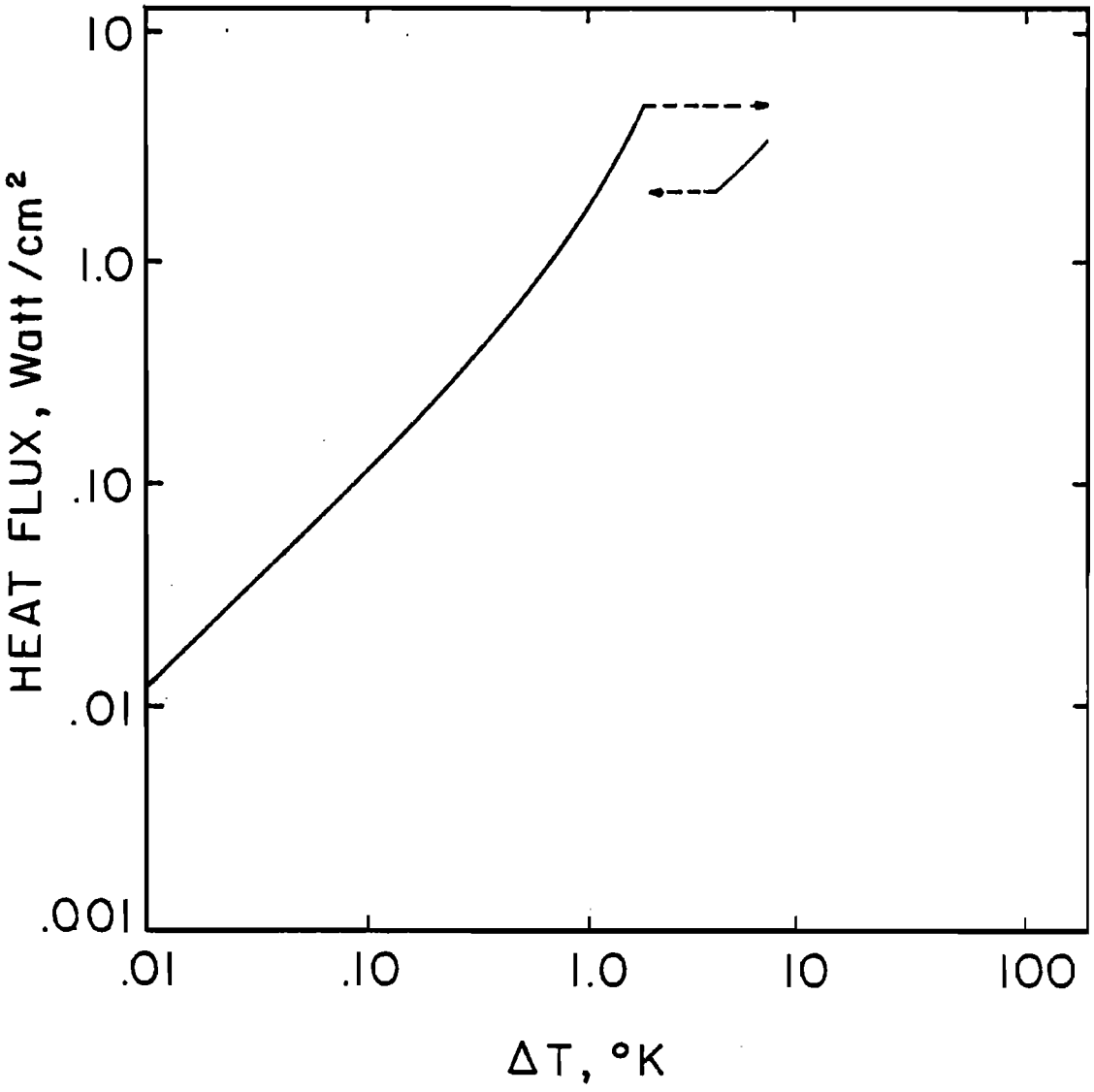

Figure 4.4 Heat flux versus ΔT for horizontal flat platinum in He II at 2.07K [4.4].

boiling occurs when the heat flux is raised above the superfluid critical heat flux Q*.

Measurements in the Kapitza regime are found to follow an equation of the form

$$H_k = \lim_{\Delta T \to 0} \frac{Q/A}{\Delta T} = H_o T_b^m \ ,$$

where T_b is the temperature of the liquid helium bath. H_k is called the Kapitza conductance. The exponent m ranges from 2.5 - 4.5 for most measurements; the value of the constant H_o ranges from about 0.1 - 10 watt/cm^2. As ΔT rises Q/A deviates from a linear dependence upon ΔT. Theories for the Kapitza conductance predict that $Q/A \propto T_s^4 - T_b^4$ where T_s is the temperature at the metal surface; the behavior of Q/A at high heat fluxes is thus expected to follow an equation of the form

$$Q/A \propto T_s^4 - T_b^4 = \Delta T[1 + \frac{3}{2}\frac{\Delta T}{T_b} + (\frac{\Delta T}{T_b})^2 + \frac{1}{4}(\frac{\Delta T}{T_b})^3]T_b^3 \ .$$

This equation describes the nonlinear regime reasonably well except at very high fluxes [4.6,4.14]; deviations from this equation may be due to the assumption that $Q/A \propto T_s^4 - T_b^4$. Some researchers have found deviations from this behavior when the surface temperature of the sample exceeds 2.17K [4.6,4.16].

The range of measured values for the Kapitza conductance varies considerably, depending upon the sample material, surface finish, strain, etc. The Kapitza conductance is independent of the sample orientation [4.10] or depth of immersion [4.17]. One source of these variations is the experimental problem of determining the surface temperature at the surface next to the liquid helium; this is normally done by extrapolation of measurements along the length of the sample; this procedure could lead

to large errors in the surface temperature, especially for low thermal conductivity materials such as most superconductors; surface damage due to machining or contamination could also cause the surface temperature to be overestimated. This error could not account for the large range of values reported for the Kapitza conductance of metals; measurements of the Kapitza conductance of copper span an entire order of magnitude [4.8]. Measurements by Ridner et al. [4.18] indicate that the actual surface temperature is in fact very sensitive to the surface treatment. In general, the surfaces with the highest Kapitza conductance are clean, unstrained samples. For example, Wagner et al. [4.19] systematically studied the effect of strain upon several materials and found that the Kapitza conductance steadily decreased as the strain was increased. The range of reported values for the Kapitza conductance is probably due to differences in the conditions at the sample surfaces.

Figure 4.5 illustrates the dependence of Q* upon the temperature of the superfluid He II [4.20,4.21]. The curve for Q* is found to be continuous as the helium temperature is lowered below the lambda point; Q* rises very quickly to a peak value Q^*_{max} at about 1.9K and then decreases slowly as the He II temperature is lowered below 1.9K. The reported values for Q^*_{max} range from 1 - 10 watt/cm^2, depending upon the sample shape and configuration. For cylindrical samples Q* increases as the sample diameter is decreased; for very fine wires Q^*_{max} exceeds 10 watt/cm^2 [4.20]. In addition, Q* is generally observed to increase as the depth of immersion of the sample is increased [4.14,4.22-4.23]. Q* is found to be independent of the orientation of the surface [4.10,4.17]. Measurements on contaminated surfaces indicate that Q* depends upon the

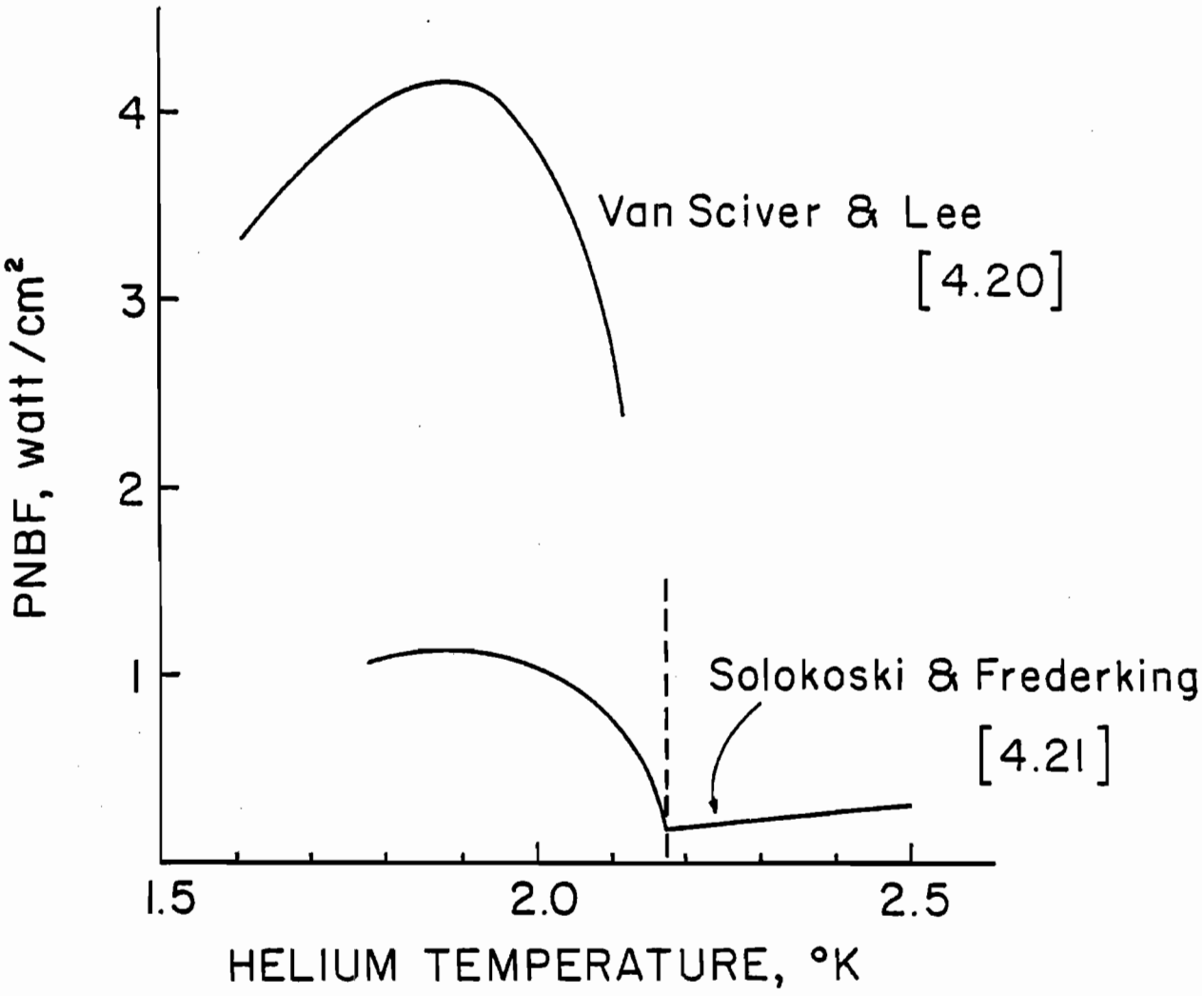

Figure 4.5 Critical heat flux in saturated He II.

conditions at the surface; Lyon [4.4] found that Q* was initially lowered for a contaminated surface. However, film boiling in He II is often accompanied by surface temperature fluctuations and intense acoustic noise which disrupts and cleans the surface [4.4,4.23]. Finally, Q* may be raised by a factor of two or more by subcooling the liquid helium [4.23]. This brief survey of the various factors that influence the film boiling regime in He II indicates yet again the importance of measuring the heat transfer characteristics for a given device.

A good theoretical understanding of heat transport in He II has not yet been achieved for two reasons: one reason is that the experimental results depend upon the sample configuration and surface conditions; the second reason is that heat transport in He II is very complex. Several theoretical approaches to Kapitza conduction will be discussed here. First, the maximum expected heat transport is given by the phonon radiation limit; the number of phonons striking an interface per second per unit area is given by

$$J = \frac{1}{4} \times v \times U$$

where v is the mean velocity of the phonons and U is the phonon energy density per unit volume; using the Debye expression for the energy density [4.24] then the net energy flux across an interface is given by

$$J = \frac{\pi^4 k_B^2}{10\hbar\theta_D^2} \left(\frac{3N}{4\pi}\right)^{2/3} (T_s^4 - T_b^4) ;$$

H_k is calculated by letting $\Delta T \to 0$ in the above expression, giving

$$H_k = \frac{2\pi^4 k_B^2}{5\hbar\theta_D^2} \left(\frac{3N}{4\pi}\right)^{2/3} T_b^3$$

This expression gives approximately the correct temperature dependence

but is one order of magnitude higher than the best measured Kapitza conductances. The acoustic mismatch theory (AM) developed by Khalatnikov gives the average probability that a phonon will cross from the metal into the liquid; the transmission probability is approximately equal to the ratio $\rho_\ell v_\ell / \rho_s v_s$, where the subscripts ℓ and s refer to the liquid and solid, respectively (see the discussions in References [4.7,4.8] for example); for He II $\rho_\ell \sim 0.1$ gm/cm^3 and $v_\ell \sim 10^4$ cm/sec [4.6] while for most solids $\rho_s \sim 5$ gm/cm^3 and $v_s \sim 10^5$ cm/sec; accordingly the Kapitza conductance is reduced by a factor of several hundred from the phonon radiation limit due to reflection of phonons at the metal to liquid helium interface. The acoustic mismatch theory underestimates the Kapitza conductance to He II by at least an order of magnitude. Extensions of the AM theory for the case of solid to solid heat transport are fairly successful in explaining the measured conductances in that case [4.25]. Recent measurements of the dependence of the transmission coefficient upon the angle and polarization of the incident and transmitted phonons indicate that the AM theory correctly describes one mechanism for energy transport across the metal to liquid interface [4.26]; considerable energy transport at angles outside those predicted by the AM theory indicates that the high conductance is due to another non-classical mechanism for heat transport across the interface. Theories for the Kapitza conductance to liquid He must account not only for the observed magnitude and temperature dependence but also for two other effects: first, the similar behavior for heat transport to ^{3}He and ^{4}He [4.7] indicates that other modes in the fluids (quasiparticles, etc.) are not important in the transport of heat to the fluids; second, H_k is

higher for a metal in the normal state than in the superconducting state; the difference between H_k in the normal and superconducting states is largest for strong coupling superconductors [4.6,4.9]. Suggestions for non-classical effects that may be important in heat transport to He II include absorption and desorption of He atoms at the interface or phonon modulation of the surface charge density [4.7-4.9].

Theoretical values for Q* are computed in terms of the heat flow required to raise the temperature of the liquid helium near the surface above 2.17K. Heat flow in He II is usually treated in terms of two-fluid hydrodynamics: the superfluid component flows freely with zero viscosity and carries no heat; the normal fluid component carries the heat away from the metal. At high heat fluxes the motion is turbulent; for systems with dimensions above 1 mm the dominant dissipative process is the mutual friction between the two fluids (see Reference [4.5]). With this approach Van Sciver and Lee [4.20] fit their data (shown in Figure 4.5) reasonably well; the calculated temperature dependence was correct although the calculated magnitudes were somewhat higher than the measured values.

The theoretical understanding of heat transport in the film boiling regime in He II is not very good because of the complex interaction between heat transport in He II and the thermal resistance at the metal to He II interface; temperature fluctuations and acoustic noise further modify the heat transfer. Recently, Labuntzov [4.27] has developed a theory which seems to describe film boiling for fine wires; extensions of this theory may be of use for larger systems.

4.4 Summary and Heat Transport from Superconducting Nb to Liquid Helium

In summary, at low heat fluxes heat transport to He I is described by nucleate boiling with $Q/A \sim (\Delta T)^{1.65}$; heat transport to He II is described by Kapitza conduction with $Q/A \sim (\Delta T)^{1.0}$. Hence He II cools most effectively at low heat fluxes. As the heat flux reaches the level of 0.1 watt/cm^2 He I and He II cool about equally effectively. However, the peak heat flux that may be sustained before film boiling begins is significantly higher for He II; thus He II is usually used in cooling superconducting devices.

Finally, estimates for heat transport from superconducting Nb to superfluid He II are given in Table 4.1 [4.28-4.29]. The constants H_o and m in the equation $H_k = H_o \times T_b^m$ are listed; measured values at 1.8K are included in Table 4.1 for comparison. These measured values provide a rough estimate for the Kapitza conductance of clean Nb samples in the superconducting state. Measurements for heat transport from Nb to He I are not available in the literature. One reasonable estimate to use for Nb are the measurements by Lyon for flat platinum [4.10]; the measurements by Tsuruga and Endoh for a large copper cylinder (2.5 cm diameter) give somewhat lower values for heat transport to He I [4.11]. Film boiling in He I is likely to occur for heat fluxes exceeding about 0.5 watt/cm^2, depending upon the sample orientation, etc. Film boiling in He II is likely to occur for heat fluxes exceeding 1-5 watt/cm^2, depending upon the sample configuration and depth of immersion. These estimates for heat transport from superconducting Nb to liquid He should only serve as guidelines; precise values may be obtained only by measurements for the given system.

Table 4.1 Kapitza Conductance of Nb in the Superconducting State

Specimen	H_o $\frac{watt}{cm^2\text{-}K}$	m	$H_k(1.8K)$ $\frac{watt}{cm^2\text{-}K}$
#1, Run 2 [4.29] Electropolish	.0136	3.99	.145
#2 [4.29] Electropolish	.0252	3.90	.25
#3, Run 1 [4.29] Electropolish	.0072	4.41	.094
#3, Run 2 [4.29] 165°C anneal & electropolish	.0145	3.96	.15
#4 [4.29] Electropolish	.0248	4.30	.31
Nb 1 [4.28] as is	.017	3.62	.14
Nb 2 [4.28] annealed	.020	4.65	.31
Average			.20±.08

References for Chapter 4

[4.1] P. L. Kapitza, J. Phys. (USSR) 4, 181 (1941).

[4.2] C. Johannes, Proc. 3rd Intnl. Cryogenic Engineering Conf. ICEC 3, 97 (1970).

[4.3] R. V. Smith, Cryogenics 9, 11 (1969).

[4.4] D. N. Lyon, Chem. Engr. Prog. Symp. Series, J. A. Inst. Chem. Engr. 64, 82 (1968).

[4.5] S. W. Van Sciver, Proc. 8th Intnl. Cryogenic Engineering Conf., ICEC8, 228 (1980).

[4.6] T. H. K. Frederking, Chem. Engr. Prog. Symp. Series, J. A. Inst. Chem. Engr. 64, 21 (1968).

[4.7] L. J. Challis, J. Phys. C: Solid State Phys. 7, 481 (1974).

[4.8] N. S. Snyder, Cryogenics 10, 89 (1970).

[4.9] G. L. Pollack, Rev. Mod. Phys. 41, 48 (1969).

[4.10] D. N. Lyon, Adv. Cryogenic Engr. 10, 371 (1965).

[4.11] H. Tsuruga and K. Endoh, Proc. 5th Intnl. Cryogenic Engineering Conf., ICEC5, 262 (1974).

[4.12] B. I. Verkin, Yu. A. Kirichenko, S. M. Kozlov, and K. V. Rusanov, Proc. 8th Intnl. Cryogenic Engineering Conf., ICEC8, 256 (1980).

[4.13] R. D. Cummings and J. L. Smith, in Technologie de l'helium liquide, issued by Institut International du Froid, Paris, pg. 85 (1966); also reported in [4.15].

[4.14] J. S. Goodling and R. K. Irey, Adv. Cryogenic Engr. 14, 159 (1969).

[4.15] W. B. Bald and T.-Y. Wang, Cryogenics 16, 314 (1976).

[4.16] S. W. Van Sciver, Adv. Cryogenic Engr. 23, 340 (1977).

[4.17] M. A. Hilal, Adv. Cryogenic Engr. 25, 358 (1980).

[4.18] A. Ridner, E. N. Martinez, and F. de la Cruz, Phys. Rev. Lett. 35, 855 (1975).

[4.19] F. Wagner, F. J. Kollarits, K. E. Wilkes, and M. Yaqub, J. Low Temp. Phys. 20, 181 (1975).

[4.20] S. W. Van Sciver and R. L. Lee, Adv. Cryogenic Engr. 25, 363 (1980).

[4.21] S. C. Solokoski and T. H. K. Frederking, Proc. 7th Intnl. Cryogenic Engr. Conf., ICEC7, 222 (1978).

[4.22] T. H. K. Frederking and R. L. Haben, Cryogenics 8, 32 (1968).

[4.23] H. Kobayashi and K. Yasukuchi, Adv. Cryogenic Engr. 25, 372 (1980).

[4.24] N. W. Ashcroft and N. D. Mermin, Solid State Physics, Holt, Rinehart and Winston, NY, 1976.

[4.25] S. B. Kaplan, J. Low Temp. Phys. 37, 343 (1979).

[4.26] A. F. G. Wyatt, in Phonon Scattering in Condensed Matter, ed. H. J. Maris, Plenum Press, NY, 1980, pg. 181.

[4.27] D. A. Labuntzov and Ye. V. Ametistov, Cryogenics 19, 401 (1979).

[4.28] K. Mittag, Cryogenics 13, 94 (1973).

[4.29] K. E. Wilkes, Ph.D. thesis, Ohio State University (1978).

Chapter 5

PREPARATION AND CHARACTERIZATION OF HIGH THERMAL CONDUCTIVITY NIOBIUM

5.1 Introduction

In this chapter the procedures used to prepare high thermal conductivity Nb will be described. As discussed in Chapter 3, in order to have high thermal conductivity Nb the residual resistivity of the Nb must be low; this means that the defect concentration in the Nb must be minimized. First, the types of defects and their effects upon the residual resistivity of Nb will be discussed. Next, the two steps used to prepare high purity Nb will be described: the first step was to use electrodeposited Nb to reduce the concentration of several metallic impurities, especially Ta; the second step was to outgas the Nb at high temperatures in ultra high vacuum to remove other impurities to the level of a few parts per million (atomic). At the end of this chapter measurements of the thermal conductivity of several test samples of outgassed Nb will be reported. These measurements served several purposes: first, they gave definitive measurements of the thermal conductivity for the electrodeposited Nb cavities prepared in the same manner; these measurements also provided a means to investigate the effects of various treatments (such as chemical polishing) upon the thermal conductivity of the Nb; finally, both the measured electronic and lattice thermal conductivity were found to agree with the results that were expected on the basis of the processes used in preparing the high purity Nb.

5.2 Defects in Nb

Two types of defects cause deviations from a perfect lattice in

metals. The most important type of defects in Nb are foreign atoms located either on lattice sites (substitutional impurities) or between lattice sites (interstitial impurities). In addition, several kinds of intrinsic defects are found in metals: these include vacancies, metal atoms at interstitial sites, dislocations and grain boundaries.

Several kinds of foreign impurities are found in Nb. Typical impurity concentrations in commercial high purity Nb [5.1-5.3] are listed in Table 5.1. The first group of impurities consists of metals such as Ta, W, and Mo that lie near Nb in the periodic table and substitute for Nb in the lattice; Ta lies directly below Nb in the periodic table and is usually present in relatively large quantities. These substitutional impurities are difficult to remove because they have similar physical and chemical properties to the Nb atoms. Their concentrations may be reduced slightly by refining or electron-beam melting [5.4-5.5]. Their concentrations may be considerably reduced by electrodeposition of the Nb [5.6], as described in Section 3 of this chapter; the other method to reduce the concentration of these substitutional impurities is a multiple step process involving extraction of niobium pentoxide which is converted to niobium pentachloride and then thermally dissociated in a vacuum [5.7].

The second group of impurities consists of metallic impurities that are quite different from Nb. These impurities include Fe, Al, Cu, Si, Mg, etc., all of which are found in varying quantities in commercial high purity Nb. The important characteristic of these metals is that they have low melting points, and vapor pressures many orders of magnitude higher than Nb at high temperatures; hence, most of these metallic impurities may be reduced to levels below a few atomic ppm by UHV

Table 5.1 Impurity Concentration in Commercial High Purity Nb [5.1-5.3] and the Effect of Impurities upon the Residual Resistivity of Nb [5.7-5.11]

Element	Typical Impurity Concentration	$\frac{\Delta\rho_o}{\Delta C}$ $\frac{10^{-4}\ \mu\Omega\text{-cm}}{\text{at. ppm}}$
Ta	$\gtrsim$200	0.11-0.25
V	$\sim$1	
W	5-50	0.35-1.10
Mo	1-10	.20
Cr	1-20	--
Hf	$\sim$2	1.40
Zr	2-30	1.10
Ti	$\sim$2	0.96-1.25
Fe	2-20	--
Al	1-40	--
Cu	1-10	--
Si	$\sim$30	--
Mg	$\sim$10	--
Mn	1-4	--
Ni	4-40	--
Pb	$\sim$1/2	--
H	5-500	0.64
C	10-300	2.9-4.3
N	50-500	3.0-9.9
O	100-2,000	4.1-8.1

outgassing of the Nb at high temperatures or by UHV electron-beam melting of the Nb.

The final group of impurities in Nb are light elements such as H, C, N, and O which are found at interstitial sites in the lattice; these impurities are normally present in relatively large quantities in commercial high purity Nb. However, the concentration of these impurities may be reduced to the atomic ppm level by heating the Nb at temperatures close to its melting point in an ultra-high vacuum; the outgassing process will be described in Section 4 of this chapter.

The effectiveness of many of the impurity atoms at scattering electrons is summarized in Table 5.1, where the influence of low impurity concentrations upon the residual resistivity of Nb is given in units of 1×10^{-4} $\mu\Omega$-cm per atomic ppm impurity concentration. The results for metallic impurities are from References [5.7-5.9]; the result for hydrogen is from Reference [5.10]; Reference [5.11] contains a summary of results for interstitial C, N, and O in Nb; most of the results given in Reference [5.11] lie between $3.5\text{-}5.5\times10^{-4}$ $\mu\Omega$-cm per atomic ppm. The substitutional impurities such as Ta and V that are similar to the Nb atoms are relatively weak scatterers of electrons; the interstitial impurities are relatively strong scatterers of electrons.

Scattering of electrons by intrinsic defects has not been investigated carefully for BCC metals such as Nb because impurity scattering usually dominates the residual resistivity. According to Meyerhoff [5.8] the contribution of vacancies to the residual resistivity of Nb is negligible for Nb with an RRR below 20,000. A rough estimate of the contribution of dislocations to the residual resistivity of Nb was made

by Zubeck et al. [5.12]; they estimated that the dislocation resistivity of Nb is given by $\Delta\rho_o/\Delta D = 7\times10^{-12}$ $\mu\Omega$-cm^3, where D is the number of dislocations per cm^2; this estimate is about an order of magnitude higher than measurements made on FCC metals by Gregory et al. [5.13]. Since dislocation densities in annealed Nb are typically below 1×10^8 lines/cm^2 [3.7] then dislocation scattering is probably only important for Nb with an RRR above 20,000. The contribution of grain boundaries to the scattering of electrons is also likely to be negligible, since grain boundaries may be considered as arrays of dislocations. Thus intrinsic defects are not likely to constitute a significant source of electron scattering. However, if the Nb is severely strained then dislocation scattering of electrons may make a measurable contribution to the total residual resistivity of the Nb.

The maximum impurity levels allowable in Nb to achieve a desired residual resistivity ratio may be estimated from Table 5.1. As discussed at the end of Chapter 2, for this investigation of thermal transport in cavities made of high thermal conductivity Nb an RRR of 3,000 or more was desired. This meant that the Ta content of the Nb had to be well below 200 atomic ppm while the total concentration of H, C, N, and O had to be well below 10 atomic ppm. This was accomplished by using electrodeposited Nb, which reduced the Ta concentration to a few atomic ppm; the Nb was then outgassed in an ultra high vacuum to reduce the interstitial impurity concentrations to a few atomic ppm.

5.3 Electrodeposition of Niobium

The electrodeposition of Nb will be described here very briefly; the process has been described in detail by Mellors and Senderoff [5.6,

5.14]. The electrodeposition takes place in a fused salt electrolyte containing LiF, NaF, KF, and K_2NbF_7; the electrolyte is maintained at about 800C under an argon atmosphere. Commercial reactor grade Nb sheet was used for the anodes. OFHC copper mandrels were prepared for use as cathodes. The niobium was then electrodeposited to the copper cathodes as described in Reference [5.6]; the electrodeposition of Nb for this investigation was performed by General Metals Technologies Corp. [5.15]. After deposition the Nb metal was removed from the copper mandrel by dissolving the copper in a mixture of HNO_3 and H_2O.

The uniformity of the deposited Nb depended very strongly upon the shape of the copper mandrel and upon the thickness of the plated Nb. In particular, the Nb deposition was quite thick and uneven at outside corners and quite thin at inside corners. The best results were achieved when the size of the copper mandrel was much greater than the dimensions of an X-band muffin-tin cup so that the outside edges of the mandrel were not near the cup area. The dimensions of the copper were thus chosen to be 6"x2"x1" thick before machining; a muffin-tin form was then machiend out of each side of the copper with dimensions of 0.94"x0.60" x0.32" high and 1/8" radii at most of the corners. The completed mandrel thus resembled a 6"x2"x1/4" thick copper plate with a muffin-tin form protruding from each side; the inside cavity surface was then the smooth Nb surface that was next to the copper surface during the deposition process. The thickness of the Nb deposition for such mandrels varied withlocation as follows: when the cavity cup-bottom was about 0.052" thick then the cavity sidewalls were about 0.020" thick and the Nb in the area next to the cup was about 0.030" thick. In addition, the Nb

thickness was always lower at the end of the mandrel that was closest to the top of the plating bath. Therefore the location that plated most poorly was the cavity wall that was closest to the top of the electrolyte bath; the plated Nb at the upper sidewall became quite bumpy on the outside surface when the thickness of the Nb exceeded 0.020"; furthermore, the inside surface at the upper sidewall was found to be pitted when examined under a microscope. Further experimentation with the plating process was not possible for this investigation; schemes such as shaping the Nb anodes might improve the Nb deposition at the corners.

Impurity analysis of the electrodeposited Nb provided further evidence for the poor quality of the Nb deposited at corners. Samples from different parts of the electrodeposited Nb pieces were chemically polished to remove any surface contamination; neutron activation analysis was then performed to determine concentrations of Ta, W, Cu, Na, and K in the Nb. The concentrations of Ta, W, and Cu were about the same in each of the Nb samples. However, the concentrations of Na and K ranged from 1/2 - 1 atomic ppm in most of the electrodeposited Nb to 5 - 40 atomic ppm in the very bumpy Nb from the edges [5.16].

The impurity concentrations changed significantly after the Nb was electrodeposited. The Ta concentration was found to be below 3 atomic ppm while the W, Mo, and V concentrations were reported to be below 0.1 atomic ppm in electrodeposited Nb [5.3]. The Cu concentration in the electrodeposited Nb used in this investigation was about 10 atomic ppm [5.16]. Fe and Ni impurities were quite high in the electrodeposited Nb, due to contamination from structural materials used in the deposition process. The electrodeposited Nb used in this

investigation had over 1,000 atomic ppm Fe before annealing [5.17]; after annealing at 1900C the Fe concentration was only a few atomic ppm. The concentrations of interstitial C and N have been found to decrease when the Nb was electrodeposited; the C concentration has been reported to decrease from 3,000 to 40 atomic ppm after electrodeposition, while the N concentration decreased from 2,000 atomic ppm to 60 atomic ppm after electrodeposition [5.6]. The oxygen concentration of the electrodeposited Nb is fairly high (several hundred atomic ppm) due to the solubility of oxygen in the electrolyte [5.3]. In summary, the impurities in the electrodeposited Nb are either low melting point metallic impurities or the interstitial impurities; the concentrations of all of these impurities may be reduced by the UHV outgassing process to be described in the following section.

5.4 UHV Outgassing of Nb

The outgassing of H, C, N, O, and H_2O from Nb at high temperatures will be described in this section; because the melting temperature of Nb is quite high (2470C) outgassing of Nb in UHV is very effective. Hydrogen desorbs readily from Nb at temperatures above about 800C [5.18, 5.19]; two dissolved hydrogen atoms combine to form molecular hydrogen which then desorbs from the surface of the Nb. The equilibrium concentration of hydrogen in Nb, as measured by Veleckis and Edwards [5.19], is given by the formula

$$C_H = 35 \times (p_{H_2})^{\frac{1}{2}} \times \exp^{4200/T}$$

where C_H is the concentration of hydrogen in the Nb in atomic ppm, the partial pressure of H_2 gas is in torr, and T is in degrees Kelvin. The

concentration of hydrogen in Nb is thus below 1 atomic ppm for temperatures above 1000C and pressures below 1×10^{-6} torr. However, Nb readily absorbs large quantities of hydrogen when it is cooled down to room temperature after an outgassing process [5.18-5.22]. This absorption is usually prevented by an oxide barrier which is normally present at the Nb surface; this oxide layer is no longer present after the outgassing process. In order to avoid absorption of hydrogen after outgassing the sample must be cooled down to room temperature while still under ultra high vacuum (turning off the vacuum pumps will cause a high pressure of H_2 gas due to outgassing from the walls of the apparatus); then an oxide barrier must be formed by either adding a partial pressure of O_2 to the vacuum chamber [5.3,5.22] or by letting dry air into the vacuum chamber in which case an oxide barrier forms immediately.

Carbon may be removed from Nb as carbon monoxide at temperatures between 1500 and 1800C [5.23-5.26]. This process requires an excess concentration of oxygen in the Nb relative to the carbon concentration. In the case of the electrodeposited Nb this condition is already satisfied. Ordinarily a separate step is required in which a partial pressure of oxygen gas (of the order of 1×10^{-6} torr) is introduced into the vacuum chamber at a sample temperature of about 1600-1700C in order to increase the oxygen content of the Nb; after the carbon is removed as CO then the oxygen is removed by outgassing the Nb at temperatures of 1900C or higher. The equilibrium concentration of carbon in Nb, as measured by Fromm and Spaeth [5.23], is given by

$$C_C = \frac{63}{C_O} \times p_{C_O} \times \exp^{33600/T} .$$

The carbon concentration is well below 1 atomic ppm for temperatures above 1500C and partial pressures of CO below 1×10^{-8} torr provided that the oxygen concentration is above 100 atomic ppm.

The removal of oxygen takes place by evaporation of NbO and NbO_2 from the metal surface [5.27,5.28]. At high temperatures the steady-state concentration of oxygen in Nb was measured by Fromm and Jehn [5.27] to be

$$C_O = 4.4 \times p_{O_2} \times \exp^{38400/T} .$$

This curve is illustrated in Figure 5.1 for a partial pressure of O_2 of 1×10^{-9} torr; the concentration for a given temperature then scales linearly with the partial pressure of O_2. Oxygen may also be present in the Nb due to the decomposition of water vapor at the Nb surface. This was investigated by Fromm and Jehn [5.29] who determined that the equilibrium concentration of oxygen in Nb due to water vapor is given by

$$C_O = 0.085 \times p_{H_2O} \times \exp^{45200/T} .$$

Thus for temperatures above 1900C and partial pressures of H_2O below 1×10^{-8} torr the concentration of oxygen in Nb due to water vapor is below 1 atomic ppm.

Oxygen desorbs readily from thin Nb samples in the form of metal oxides. The oxygen concentration decays exponentially in time; the desorption rate from thin samples of Nb depends upon the temperature and the ratio of the sample surface area to volume. According to Gebhardt et al. [5.28] the desorption of oxygen from 0.030" thick Nb is given by

$$\log \frac{C_O(t)}{C_O(t=0)} = -18\times10^{10} \times \exp^{-65300/T} \times t$$

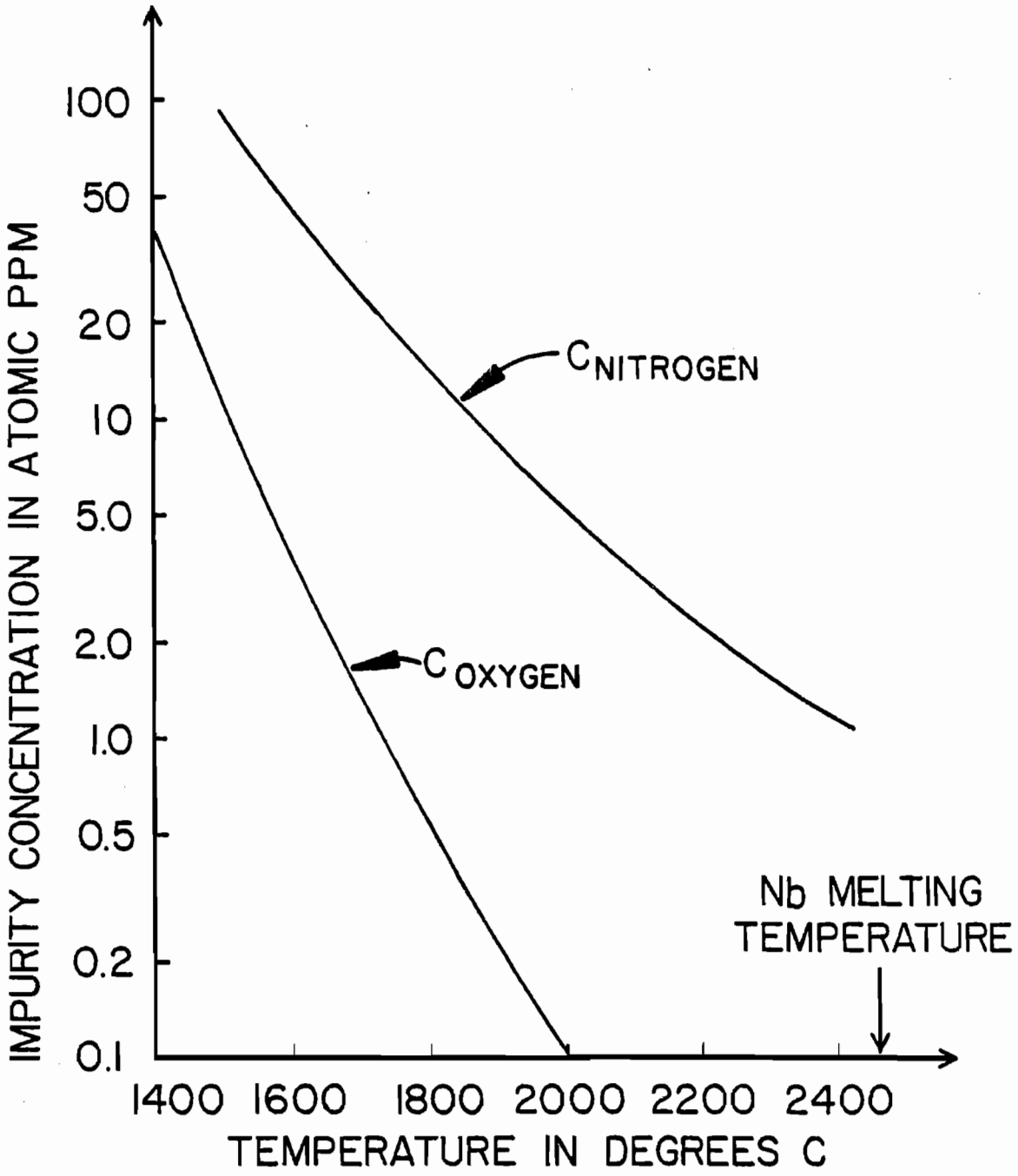

Figure 5.1 Calculated impurity concentration in Nb for a partial pressure of 1×10^{-9} torr of either O_2 or N_2.

where time is measured in minutes. The desorption of oxygen from Nb thus proceeds quickly for temperatures above 1800C; at 1900C the oxygen concentration of 0.030" thick Nb decreases by a factor of two every 20 minutes. Hence oxygen may be easily removed from thin samples of Nb; the limiting factor is the vacuum pumping speed, not the desorption rate.

The removal of nitrogen from Nb is governed by the formation and evaporation of N_2 from the Nb surface [5.28,5.30-5.32]. The high temperature equilibrium concentration of nitrogen in Nb as measured by Cost and Wert [5.32] is given by

$$C_N = 6.2 \times (p_{N_2})^{\frac{1}{2}} \times \exp^{23150/T} .$$

This curve is illustrated in Figure 5.1 for a partial pressure of N_2 of 1×10^{-9} torr. Figure 5.1 shows that reduction of the nitrogen concentration in Nb to levels below 10 atomic ppm is very difficult, since temperatures above 1900C are required at pressures of 1×10^{-9} torr. Because the nitrogen concentration scales only as $(p_{N_2})^{\frac{1}{2}}$, the pressure has to be reduced by a factor of 100 to effect a change in the nitrogen concentration of a factor of 10.

The desorption of nitrogen from Nb is much slower than the desorption of oxygen from Nb, because the desorption of nitrogen is limited by the rate at which two atoms of nitrogen combine at the metal surface to form N_2. The desorption of nitrogen from Nb is thus described by the equation

$$\frac{dC_N(t)}{dt} = k\,C_N^2(t)$$

which has a solution

$$\frac{1}{C_N(t)} = \frac{1}{C_N(t=0)} + kt .$$

According to the results of Gebhardt et al. [5.28,5.30], the desorption of nitrogen from 0.030" thick Nb is described by

$$\frac{1}{C_N(t)} = \frac{1}{C_N(t=0)} + 2.6\times10^7 \times \exp^{-62500/T} \times t$$

where time is in minutes. The desorption of nitrogen to levels below 100 atomic ppm thus proceeds slowly: at 1900C over 200 hours are required to reach 10 atomic ppm nitrogen; at 2200C 6 hours are required to reach 10 atomic ppm nitrogen. The desorption of nitrogen to the level of a few atomic ppm is therefore very difficult because high sample temperatures and long outgassing times are necessary.

The evaporation of the Nb metal itself must be considered in the UHV outgassing of Nb. The evaporation rate may be determined from the vapor pressure of Nb; the evaporation from a Nb surface is given by [5.33]

$$\nu = 9.45\times10^4 \times \frac{P}{T^{\frac{1}{2}}} \left(\frac{.001"}{hour}\right) ,$$

where the vapor pressure p is in torr and T is in degrees Kelvin. The calculated total evaporation rate for both sides of a Nb sample is shown in Figure 5.2 as a function of temperature (the vapor pressure of Nb was taken from Reference [5.34]). At temperatures below 2100C the evaporation of Nb is negligible. However, at 2200C the Nb evaporates at the rate of 0.001" every 8 hours. This constituted a serious limitation for outgassing the 0.020-0.030" thick Nb used in this investigation; after 24 hours at 2200C the Nb thickness decreased by about 10%. This evaporation rate meant that the maximum outgassing time at a temperature of 2200C was of the order of 24 hours; the samples were not outgassed at

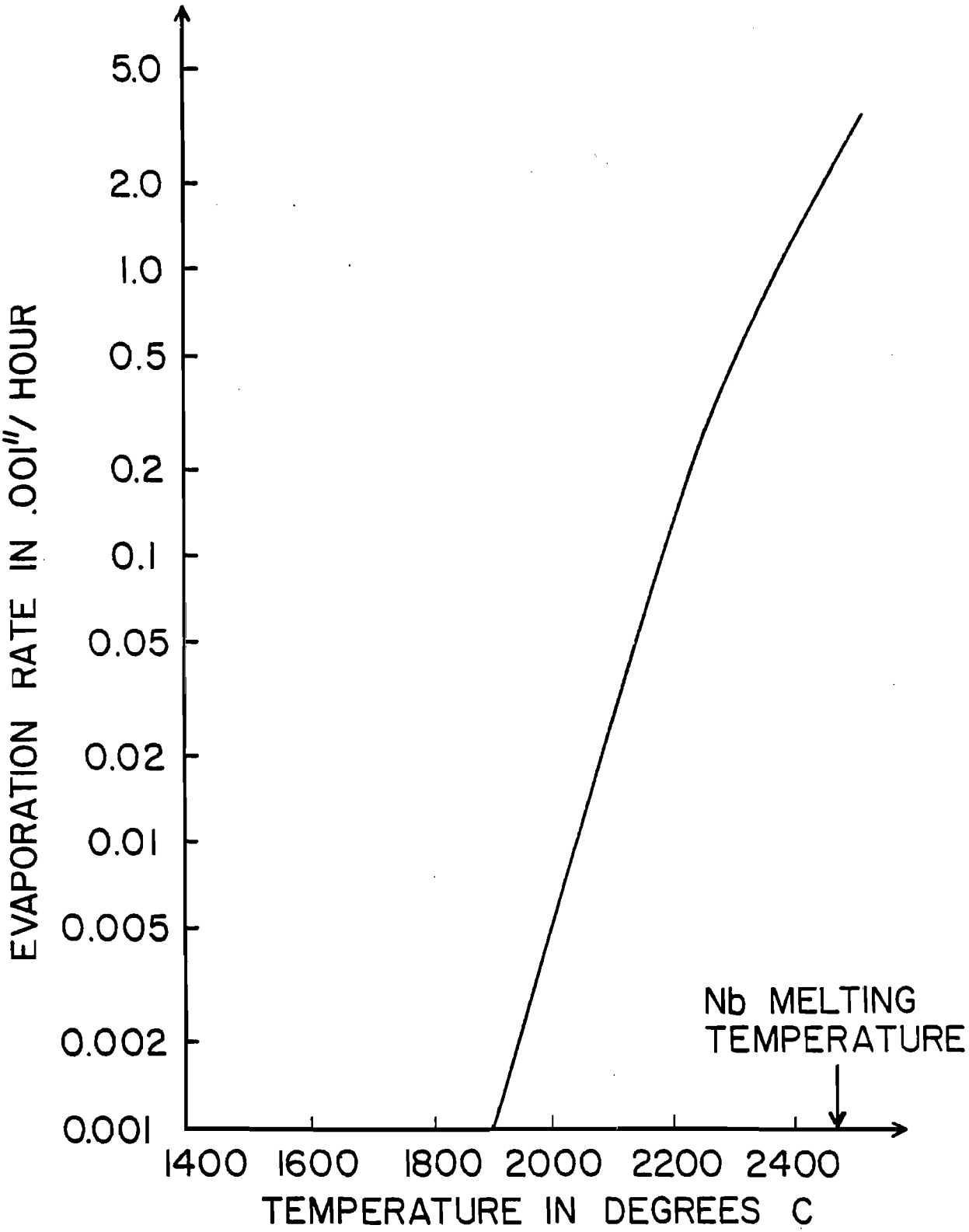

Figure 5.2 Calculated total evaporation rate for Nb (see text).

higher temperatures such as 2300C because the Nb would have evaporated at the rate of 0.001" every 2 hours. The evaporation of Nb thus limited both the final temperature and the time for which the Nb was outgassed.

5.5 Experimental Apparatus for UHV Outgassing of Nb Muffin-tin Cavities

The experimental apparatus used for the UHV outgassing of the Nb used in this investigation is shown schematically in Figures 5.3 and 5.4; the important features of the UHV apparatus will be discussed in this section. The apparatus consists of standard UHV components mounted to an 8" tee which is connected directly to a 270 liter/sec ion pump as shown in Figure 5.3; two liquid nitrogen cooled sorption pumps (indicated in Figure 5.4) were used first to bring the apparatus from atmospheric pressure to a pressure of 1×10^{-4} torr. The entire apparatus was baked out at about 350C every time a new sample was placed in the apparatus; the pressure after the bakeout was 1×10^{-9} torr. In order to maintain a low pressure when several kilowatts of power was being dissipated in the sample, both the electrical feedthroughs and the vacuum apparatus needed to be cooled. The electrical feedthroughs were cooled by two mechanisms: first, a large fan was used to blow air directly at the feedthroughs; copper tubing with circulating water inside it was soldered directly to copper clamps mounted on the outside of the feedthroughs to provide additional cooling. The 8" tee was cooled by running water; water was supplied at the top of the tee and flowed along a cloth that was wrapped around the tee. The sample was taken up to temperature in several steps over a period of three days in order to give the ion pump time to trap the desorbed gasses; the samples were then kept at their final temperature for 24 hours. With this apparatus the samples could be heated up

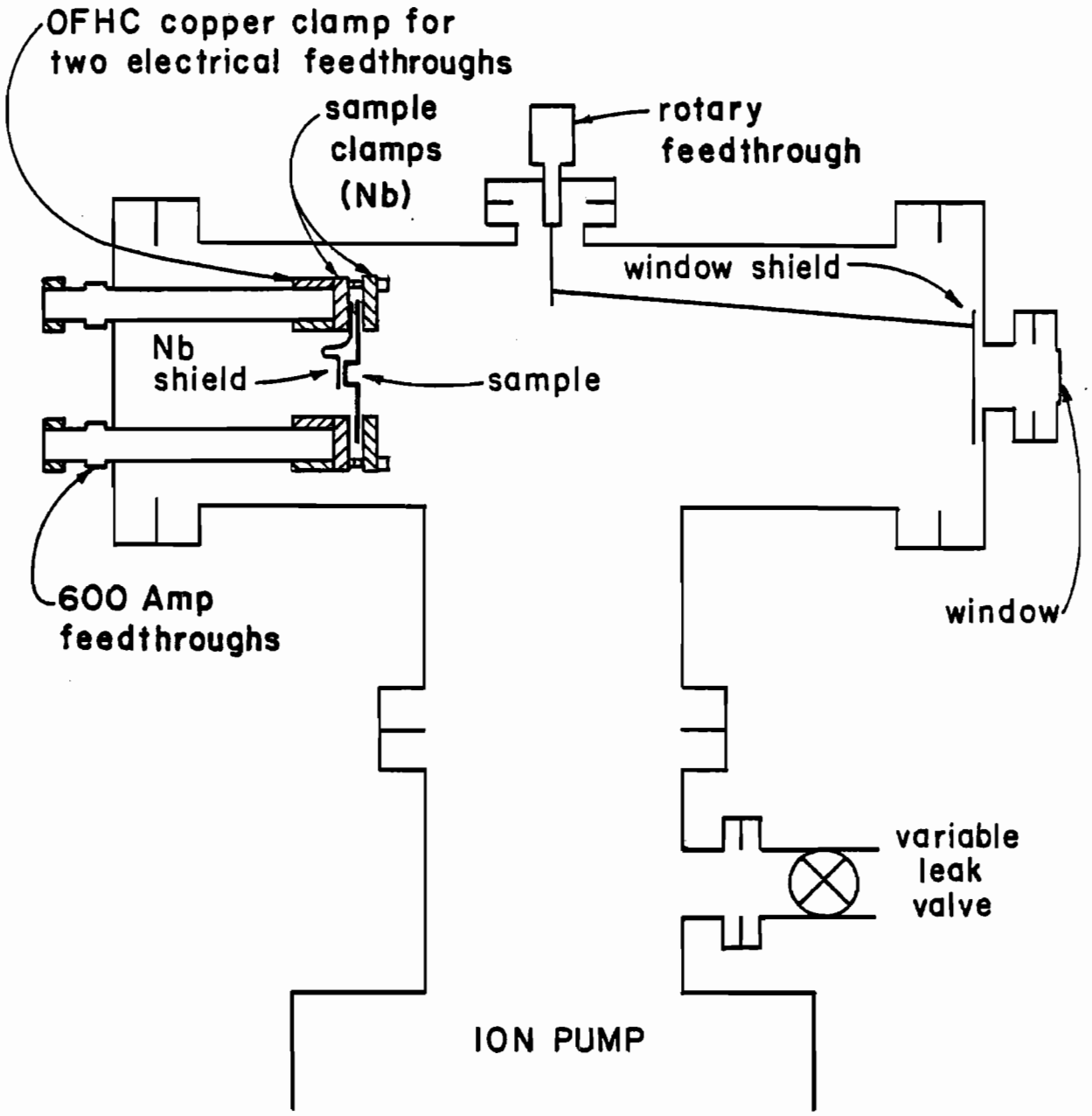

Figure 5.3 Side view of experimental apparatus for UHV outgassing of Nb.

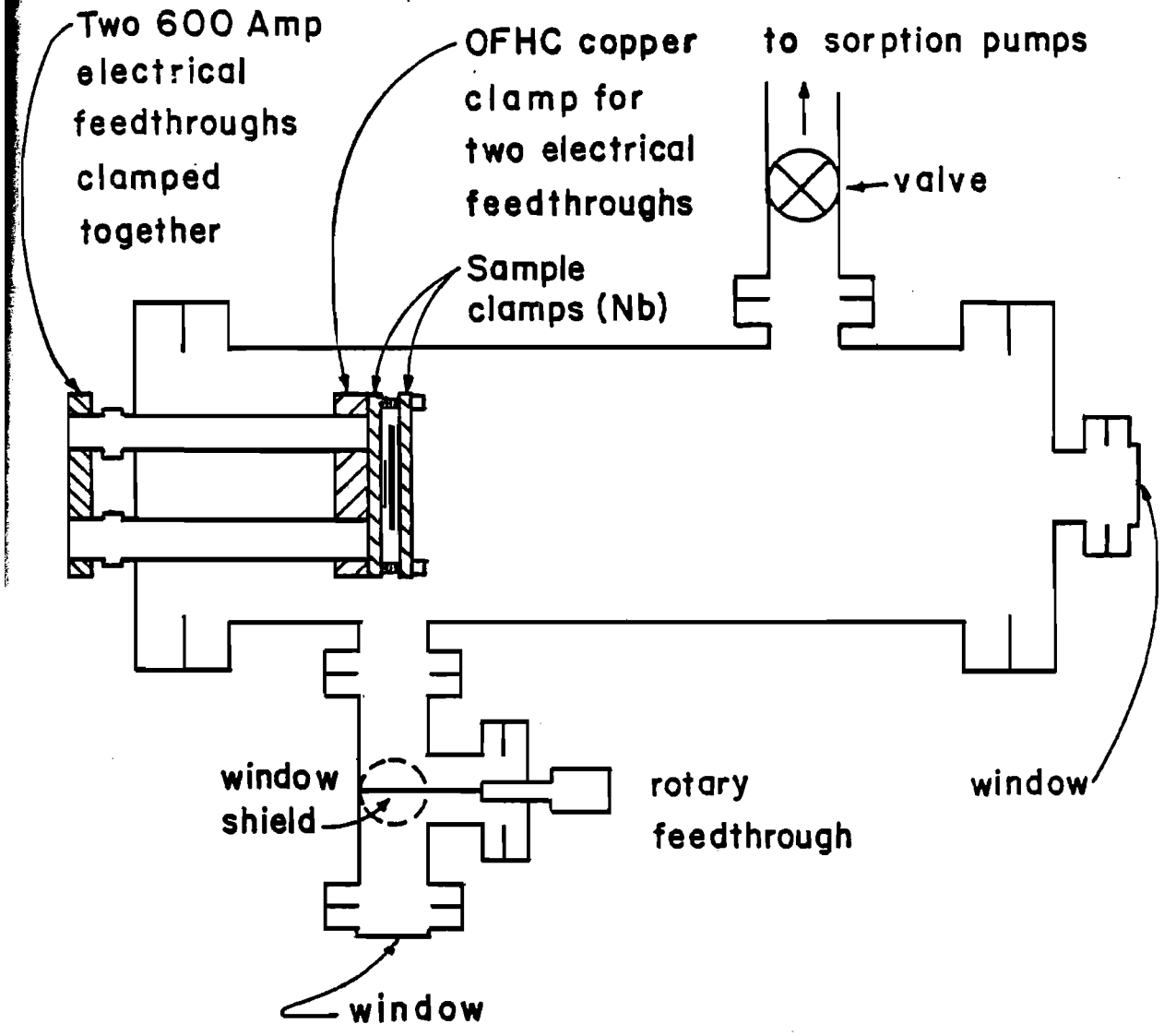

Figure 5.4 Top view of experimental apparatus for UHV outgassing of Nb.

to 1900-2200C at a final pressure of 1×10^{-9} torr.

The two UHV glass windows indicated in Figures 5.3 and 5.4 were used to view the front and side of the sample. The sample temperature was monitored with a Leeds and Northrup optical pyrometer. The measured sample temperature was then corrected for the fact that Nb is not a perfect blackbody according to the procedure described in Wood and Cork [5.35]; the high temperature emissivity of Nb used in making the corrections was taken from the measurements reported by Barnes [5.36]. An additional correction was included for the transmission loss of the window; the transmission coefficient was taken to be 0.92 [5.37]. Shields were placed in front of the windowsto protect them from the evaporating Nb which would otherwise have lowered the transmission coefficient; the two mechanical rotary feedthroughs were used to move the shields for the temperature measurements.

The Nb samples were heated resistively by passing high currents through the sample. Two pairs of electrical feedthroughs were used to supply the current to the sample; each electrical feedthrough was rated for a current of 600 Amps, so that a maximum of 1200 Amps could be used to heat the sample. The sample was mounted between the two pairs of electrical feedthroughs as shown in Figures 5.3 and 5.4; each end of the sample was held between two pieces of 1/4" Nb which were then screwed down to the OFHC copper clamps which held the pairs of electrical feedthroughs together. Power was delivered to a Variac from a 220V power line; the sample voltage was controlled with the Variac; the output from the Variac was connected to a transformer which reduced the voltage by a factor of 40 and raised the current by a factor of 40; the output from

the transformer was then connected across the pairs of electrical feed-throughs.

The expected temperature profiles for uniform rectangular samples of Nb were computed as a function of the current passing through the sample. An iterative computer program was written to find the temperature distribution along the length of the sample such that at every location the dissipated power was equal to the radiated power plus the power conducted away towards the ends of the sample. The dissipated power was computed from measured high temperature values for the electrical resistivity of the Nb [5.38]; the radiated power was computed from measured high temperature values for the total hemispherical emittance of Nb [5.39] using the Stefan-Boltzmann law [5.40] for blackbody radiation; the thermally conducted power was computed from the measured high temperature thermal conductivity of Nb [5.39] assuming a fixed value for the temperature at the ends of the sample. The calculated temperatures agreed quite well with the temperature profiles determined experimentally; this indicates that the resistive heating of Nb is governed by the balance between the dissipated power and the two mechanisms by which the power may leave the Nb; the agreement also indicates that the sample temperatures computed from measurements with the optical pyrometer were reliable.

The outgassing of X-band muffin-tin cups was more difficult than the outgassing of rectangular samples: the temperature across the width of the sample was not uniform because of the muffin-tin cup located in the middle of the sample. The temperatures at various locations during the outgassing process are shown in Figure 5.5 as a function of the total current passing through the sample; an illustration of the sample shape

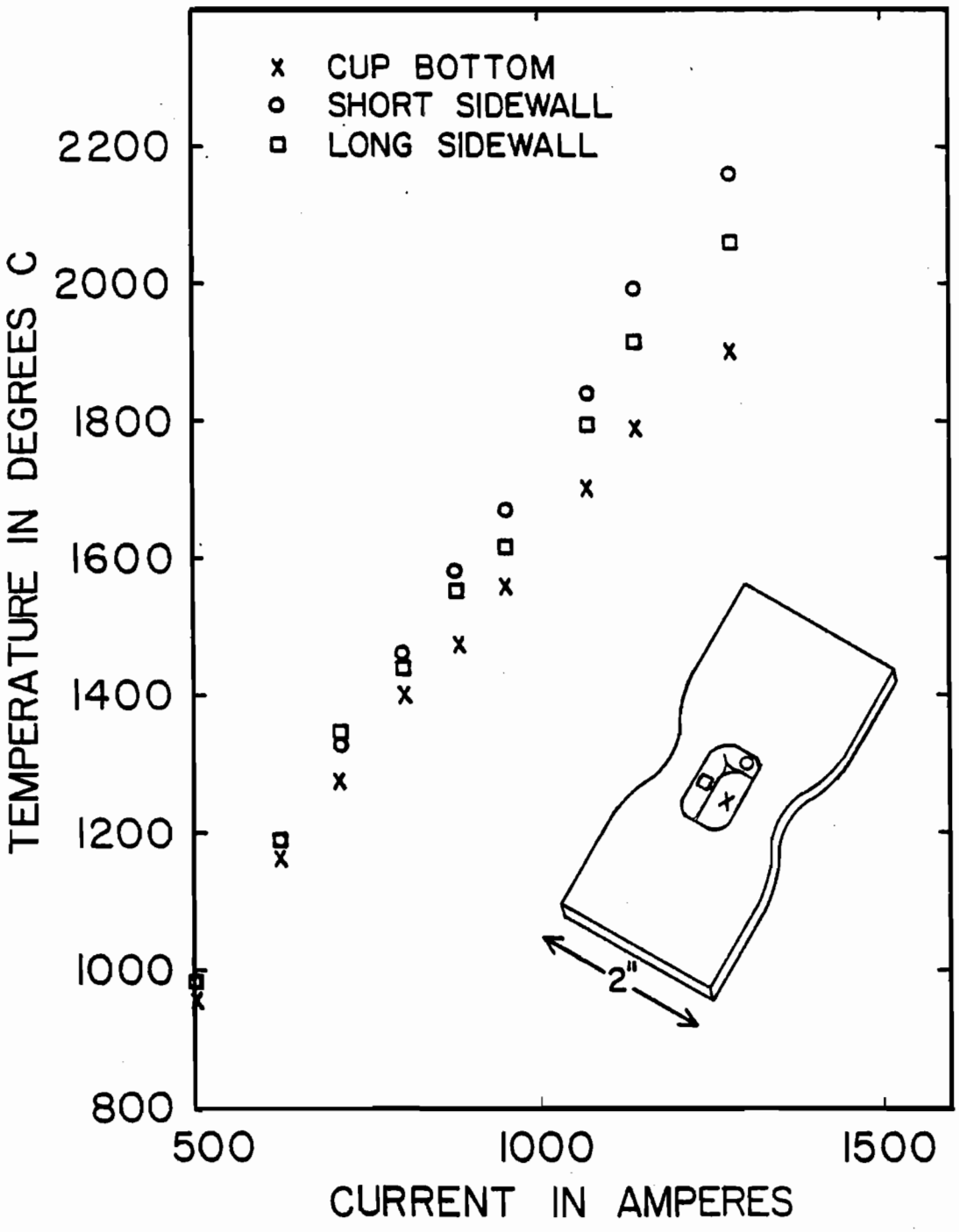

Figure 5.5 Sample shape and temperatures during UHV outgassing.

is also included in Figure 5.5. The cup region was cooler than the surrounding region because of the extra area of the cup relative to the area for a flat sample; in addition, the non-uniform sample thickness caused the Nb temperatures to be elevated at locations where the Nb was relatively thin and the electrical resistance was high. The temperature profiles shown in Figure 5.5 were achieved only by means of several modifications to the outgassing process and sample shape: first, a radiation shield made of electrodeposited Nb was located behind the cup-bottom (as shown in Figure 5.3); in addition, the cup-bottom was thinned by about 30% to a thickness of 0.030"; finally, the area next to the cup was notched to increase the current through the cup region as shown in Figure 5.5. (The sample was cold polished to remove any surface contamination before being placed in the UHV apparatus.)

With these schemes the final temperature of the Nb ranged from 1900C at the cup-bottom to 2200C at the short sidewalls. Strip samples of electrodeposited Nb were outgassed in the same UHV apparatus; their thermal conductivity was then measured in the superconducting state at temperatures between 1.4-4.2K.

5.6 Experimental Technique for the Measurement of Thermal Conductivity

The thermal conductivity measurements were straightforward: dc heat was applied at the top of the strip sample of Nb and the temperature difference along a length of the sample was measured; the thermal conductivity was then computed from the formula

$$\kappa(T) = \frac{Q}{A} \times \frac{L}{\Delta T} ,$$

where Q was the heater power, A was the cross-sectional area of the

sample, and ΔT was the temperature difference for a length L of the sample. The temperature difference was kept fairly small so that the thermal conductivity along the length of the sample would be relatively constant.

A schematic of the experimental apparatus is shown in Figure 5.6a; Figure 5.6b shows the thermometry bridge used to determine ΔT. The entire apparatus was fixed to a 4-1/2" UHV flange; the flange was then attached to the end of a 35" long vacuum pipe which was lowered inside the dewar; a diffusion pump was connected at the top of the vacuum pipe which provided a vacuum of 1×10^{-6} torr. A multi-pin feedthrough was located at the top of the dewar for leads from the apparatus. The sample was mounted to an OFHC copper post which was brazed to the vacuum flange as shown; the copper post was thus thermally connected to the liquid helium in which the apparatus was immersed. The heat source was a 1/4-watt metal film resistor with a variable power supply connected across it. Both the heater and the resistance thermometers were placed in Apiezon N grease to make thermal contact with the sample; the resistors were held in place by thread which was looped around the resistor leads, tied in a knot on the back side of the sample, and then anchored in place with GE 7031 varnish. The leads from the resistors were then connected to the UHV instrumentation feedthrough; the heat leak down the leads was negligible due to the use of small diameter constantan and manganin leads.

The helium vapor pressure was monitored in order to determine the temperature of the liquid helium bath. The sample temperatures were monitored with Allen-Bradley 1/8-watt, 100Ω carbon composition resistors. The resistance of these thermometers ranged from 1200Ω at 4.2K to 35,000Ω at 1.4K. Clement and Quinnell developed the following relationship between

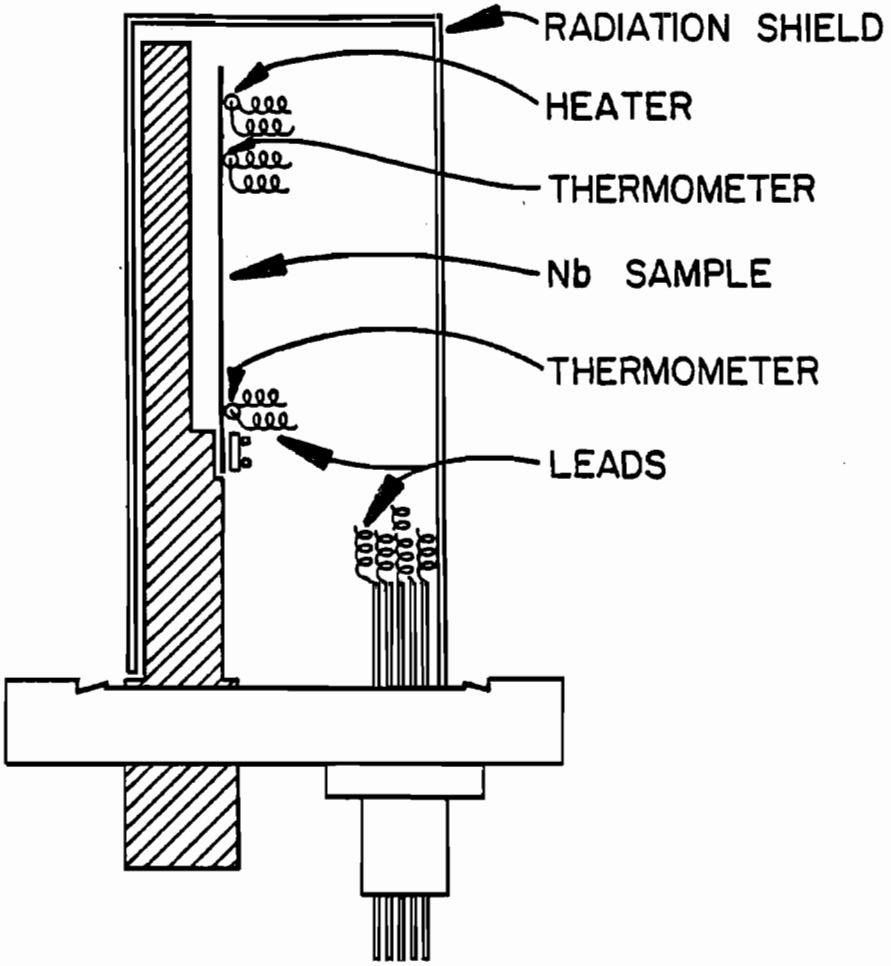

Figure 5.6a Apparatus.

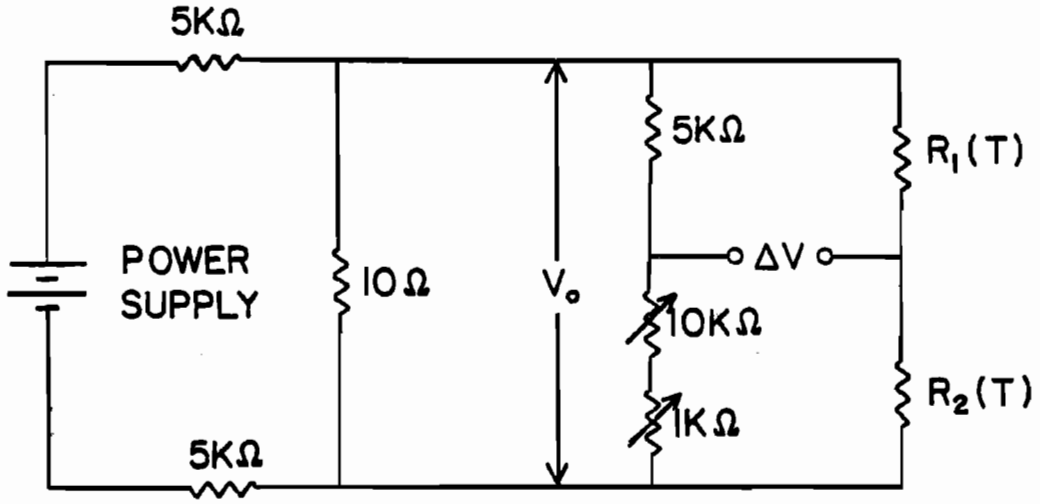

Figure 5.6b Thermometry bridge.

Figure 5.6 Thermal conductivity apparatus.

the resistance and temperature of carbon composition resistors [5.41]

$$\log(R) + \frac{C}{\log(R)} = A + B/T \ .$$

The parameters A, B, and C were determined by fitting the formula to the measured resistance at three bath temperatures. Temperatures calculated from resistance values by means of this equation were within ±0.005K of the temperatures determined from the helium vapor pressure.

The resistance of the thermometers was measured by monitoring the voltage across each thermometer with a 1μA current across the thermometer; the Joule heating of the thermometers was negligible at 1μA. The precision of the resistance measurements was limited to ±1Ω, which corresponded to ±0.002K at 4.2K and less than ±0.0001K below 2.1K.

Measurements of the temperature gradient ΔT were performed with the thermometers connected to the bridge shown in Figure 5.6b, in order to increase the accuracy of the measurements of ΔT. The bridge voltage ΔV was first zeroed with the heater off; with the heater on then ΔV was related to ΔT by the equation

$$\Delta V = \frac{V_o}{4} \times \left(\frac{1}{R}\frac{dR}{dT}\right) \times \Delta T \ ,$$

provided that the resistors were closely matched so that $R_1 \approx R_2$ and $dR_1/dT \approx dR_2/dT$. Using this bridge the sensitivity of the measurements of ΔT was increased by a factor of ten at 4.2K.

A preliminary experiment was performed to investigate the accuracy of the thermal conductivity measurements, in which the thermal conductivity of a sample of Al 1100 (commercially pure aluminum) was measured. At low temperatures the thermal conductivity of Al 1100 was expected to be linear in temperature according to the measurements of Powell et al.

[5.42]. The magnitude of the expected thermal conductivity for this sample was computed from the Wiedemann-Franz law (see Section 3.2) using the value of ρ_o measured for this sample; the measured values of the thermal conductivity for this sample were all within ±10% of the expected results. This agreement indicates that the measurement technique is satisfactory for low thermal conductivity samples.

However, the measurements of the thermal conductivity of the outgassed Nb samples were difficult to perform because of the very high thermal conductivity of these samples at temperatures above 3K. The difficulty arose because at temperatures above 3K up to 100 times as much heater power was required to obtain the same ΔT for the outgassed Nb samples as for the Al 1100 sample; at such power levels the heater temperature rose by up to 10K; the temperature measurements were not accurate at these power levels because the thermometers were very sensitive to the long wavelength radiation from the heater, as discussed in Appendix A. At bath temperatures below 3K, where the thermal conductivity of the outgassed Nb was lower, the temperature measurements were reproducible and yielded reliable measurements for the thermal conductivity of the outgassed Nb samples.

5.7 Thermal Conductivity of Electrodeposited and Outgassed Nb

The low temperature superconducting state thermal conductivity was measured for electrodeposited Nb samples that were outgassed at 1900C, 2000C, and 2200C. Measurements were also made for a sample of electrodeposited Nb that received no outgassing treatment. The experimental results are all shown in Figure 5.7, along with the published results

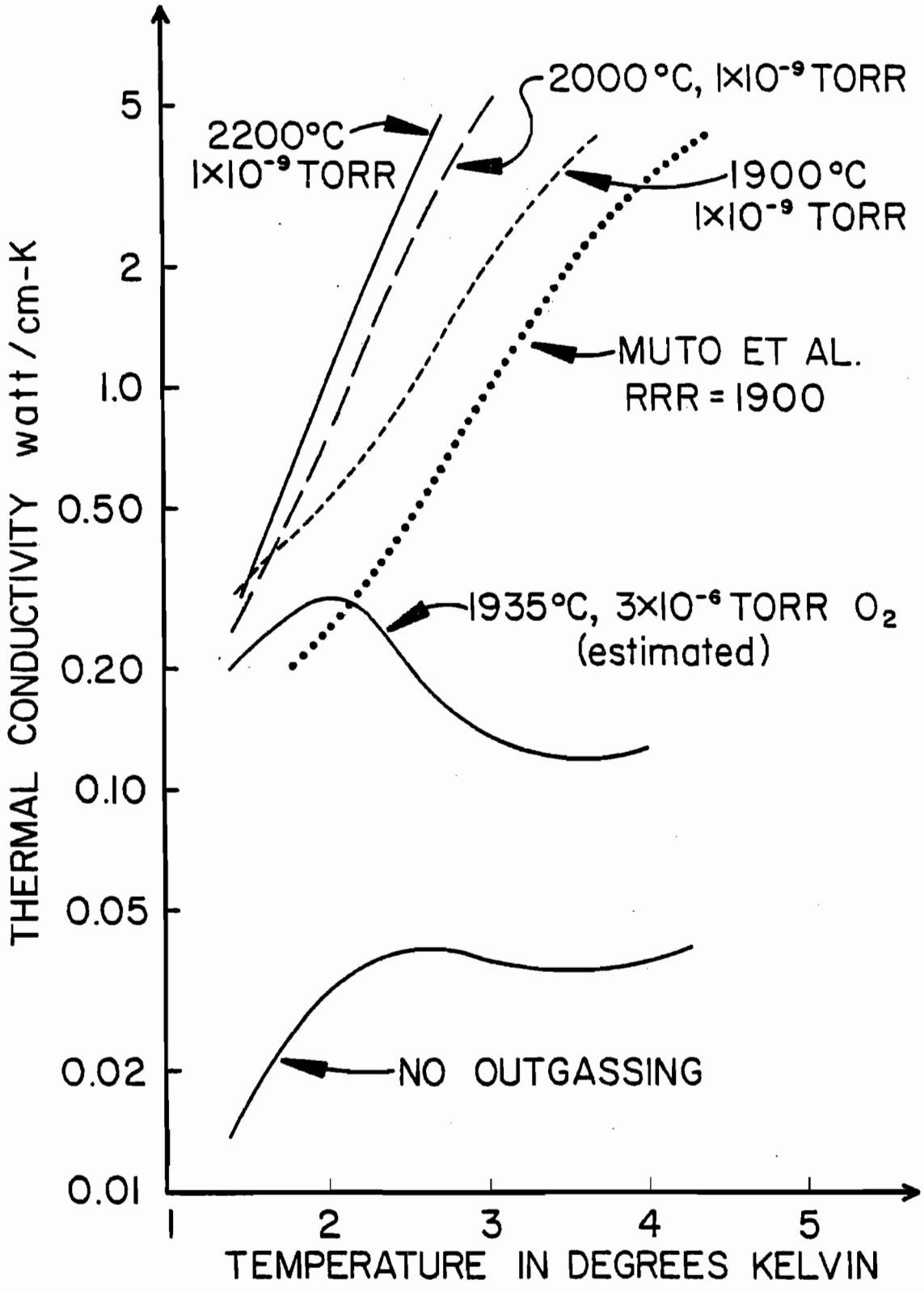

Figure 5.7 Thermal conductivity of electrodeposited Nb after different outgassing treatments (see text).

of Muto et al. [3.15] for a sample with a residual resistivity ratio (RRR) of 1900 for comparison. In addition a curve was included in Figure 5.7 that gives the expected thermal conductivity for a muffin-tin cavity that was made from electrodeposited Nb that was annealed in a partial pressure of O_2; this case will be discussed at the end of this section.

The temperature dependence of the measured thermal conductivity of the outgassed Nb is in reasonable agreement with the results of Muto et al. The magnitudes of the measured thermal conductivity for the outgassed Nb samples may also be shown to agree with the expected results. The RRR of the outgassed samples was estimated from the thermal conductivity measurements at 2.5K, where the heat transport for the high thermal conductivity Nb is entirely due to the electrons. The estimated RRRs for the samples outgassed at 1900C, 2000C, and 2200C were thus 4000, 8000, and 12000 respectively, based upon the results of Muto et al. for their sample with an RRR of 1900. The expected RRR may be computed from the formulas for the equilibrium concentrations of interstitial impurities in Nb. Hydrogen is normally the major residual gas in UHV systems. In this case Nb was continuously being evaporated from the sample onto the walls of the apparatus; because hydrogen is adsorbed by Nb films at room temperature [5.43] the major residual gas was probably the N_2 which was slowly evolving from the sample surface. If at high temperatures the gas in the UHV chamber consisted only of 1×10^{-9} torr of N_2, then the impurity concentration may be estimated by using the formula of Cost and Wert [5.32] given in Section 5.4; this gives values of 8.3, 5.2, and 2.3 atomic ppm of nitrogen in the samples outgassed at 1900C, 2000C, and

~2200C respectively; finally, the corresponding values for the RRRs of the samples are 3500, 5500, and 12000 (assuming that $\Delta\rho_o/\Delta C_N = 5\times10^{-4}$ μΩ-cm/atomic ppm and ρ(Rm.T) = 14 μΩ-cm). These calculated values for the expected RRR of the outgassed Nb agree remarkably well with the values determined from the thermal conductivity measurements. The RRR of the electrodeposited and outgassed Nb appears to be consistent with the assumption that all of the gas in the vacuum apparatus at high temperatures was nitrogen. In summary, the measured thermal conductivity of the outgassed Nb is consistent with the expected results for the electronic thermal conductivity in both magnitude and temperature dependence.

The expected lattice thermal conductivity of the annealed samples may be estimated from the grain size of these samples, which was 1-2mm, and the results of Kes et al. that are summarized in Table 3.4; for a grain size of 1.5mm the expected lattice thermal conductivity of the annealed Nb is thus $\kappa(1.46K) \simeq 0.35$ watt/cm-K. This very rough estimate of the expected lattice thermal conductivity of the annealed Nb is consistent with the measured thermal conductivity of the outgassed Nb at 1.4K.

The final curve included in Figure 5.7 is the expected thermal conductivity for a muffin-tin cavity that was made from electrodeposited Nb that was annealed in a partial pressure of 3×10^{-6} torr of O_2; the cup bottom temperature was 1680C and the temperature of the short sidewalls was 1935C during the engassing. The equilibrium concentration of oxygen in the sidewalls was computed to be 500 atomic ppm using the formula given in Section 5.4; this corresponds to an RRR of about 60. The thermal conductivity of the cavity sidewalls between 3-9K was thus

described by the results of Kuhn for a sample of RRR = 60 (curve 13 in Figure 3.2b, Reference [3.9]); below 3K the thermal conductivity was taken from measurements of Wasserbach (curve 8 in Figure 3.2b, Reference [3.24]) because the lattice conductivity of Wasserbach's sample was approximately equal to that for the electrodeposited and outgassed Nb used in this investigation.

Various treatments were given to Nb samples that were outgassed at 2200C to determine what might degrade the purity and hence the thermal conductivity of the outgassed Nb. The one treatment that lowered the thermal conductivity was electropolishing [5.44]; after electropolishing for 1/2 hour to remove 0.0004" from each surface of the sample, the thermal conductivity of the Nb was lowered by a factor of two; the Nb purity was lowered because the Nb surface was not protected by an oxide barrier during polishing, so that the hydrogen which evolves in the polishing solution was able to diffuse into the Nb. However, chemical polishing with a dilute mix of HNO_3 and HF in H_2O [5.45] did not lower the thermal conductivity of theoutgassed Nb. Furthermore, the thermal conductivity was not lowered if electron-beam welds were made at the ends of the samples; this meant that the outgassed muffin-tin cups could safely be welded into cavity frames and chemically polished prior to the microwave tests. A number of chemical substances were found to be safe for use with the outgassed Nb: GE 7031 varnish, methanol, xylene, Tra-Bond BA-2151 epoxy (used in the thermal transport measurements described in Chapter 6) and Eccostrip 93 (an organic solvent for removing epoxy) did not affect the thermal conductivity of the outgassed Nb. Finally, the thermal conductivity of the outgassed Nb was found to be

unchanged after exposure to the atmosphere for one year. Thus the oxide barrier on the Nb surface protects the Nb from hydrogen diffusing into the bulk; without the oxide barrier the Nb would have absorbed enormous quantities of hydrogen.

In conclusion, the thermal conductivity of the electrodeposited and outgassed Nb samples was found to be in agreement with the results expected on the basis of the published results for the thermal conductivity of Nb given in Chapter 3 and the expected purity of the outgassed electrodeposited Nb.

References for Chapter 5

[5.1] R. E. Reed, Second Intnl. Conf. on Electron and Ion Beams in Science and Technology, Gordon and Breach, NY, 1969, pp. 225-258.

[5.2] H. Wenzl and J.-M. Welter, Current Topics in Material Science 1, 603 (1978).

[5.3] K. Schulze, J. Metals 33, 33 (May 1981).

[5.4] R. E. Reed, J. Crystal Growth 19, 61 (1973).

[5.5] F. H. Cocks, R. M. Rose, and J. Wulff, J. Less-Common Metals 10, 157 (1966).

[5.6] G. W. Mellors and S. Senderoff, J. Electrochem. Soc. 112, 266 (1965).

[5.7] J. Barthel, K.-H. Berthel, K. Fischer, R. Gebel, G. Guntzler, M. Jurisch, W. Neumann, J. Kunze, P. Mull, H. Oppermann, R. Petri, G. Sobe, G. Weise, and W. Wisner, Fiz. Metal Metalloved. 35, 921 (1973) [transl. in Phys. Metals and Metallography 35, No. 3, 23 (1973)].

[5.8] R. W. Meyerhoff, J. Electrochem. Soc. 118, 997 (1971).

[5.9] T. G. Berlincourt and R. R. Hake, Phys. Rev. 131, 140 (1963).

[5.10] G. Pfeiffer and H. Wipf, J. Phys. F6, 167 (1976).

[5.11] K. Schulze, J. Fuss, H. Schultz, and S. Hofmann, Z. Metallkunde 67, 737 (1976).

[5.12] R. B. Zubeck, T. W. Barbee, Jr., T. H. Geballe, and F. Chilton, J. Appl. Phys. 50, 6423 (1979).

[5.13] P. Gregory, A. J. Banjay, and J. E. Hargreaves, Metallurgia 74, 71 (1966).

[5.14] S. Senderoff and G. W. Mellors, J. Electrochem. Soc. 113, 66 (1966).

[5.15] General Metals Technologies Corp., Richmond, VA.

[5.16] F. Palmer, Laboratory of Nuclear Studies, Cornell University, private communication.

[5.17] J. C. Amato, Laboratory of Nuclear Studies, Cornell University, private communication.

[5.18] J. A. Pryde and C. G. Titcomb, J. Phys. C: Solid State Physics 5, 1293 (1972).

[5.19] E. Veleckis and R. K. Edwards, J. Phys. Chem. 73, 683 (1969).

[5.20] W. M. Albrecht, W. D. Goode, and M. W. Mallett, J. Electrochem. Soc. 106, 981 (1959).

[5.21] J. A. Pryde and C. G. Titcomb, Trans. Faraday Soc. 65, 2758 (1969).

[5.22] K. Faber and H. Schultz, Scr. Metallurgica 6, 1065 (1972).

[5.23] E. Fromm and G. Spaeth, Z. Metallkunde 59, 65 (1968).

[5.24] G. Horz and K. Lindenmaier, Z. Metallkunde 63, 240 (1972).

[5.25] E. Fromm and H. Jehn, Vacuum 19, 191 (1969).

[5.26] G. Horz, Metall. Trans. 3, 3069 (1972).

[5.27] E. Fromm and H. Jehn, Z. Metallkunde 58, 61 (1967).

[5.28] E. Gebhardt, E. Fromm, and D. Jakob, Z. Metallkunde 55, 432 (1964).

[5.29] E. Fromm and H. Jehn, Z. Metallkunde 58, 120 (1967).

[5.30] E. Gebhardt, W. Durrschnabel, and G. Horz, J. Nuclear Materials 18, 149 (1966).

[5.31] E. Gebhardt, E. Fromm, and D. Jakob, Z. Metallkunde 55, 423 (1964).

[5.32] J. R. Cost and C. A. Wert, Acta Metallurgica 11, 231 (1963).

[5.33] S. Dushman, Scientific Foundations of Vacuum Technique, John Wiley and Sons, NY, 1949, pg. 17.

[5.34] R. E. Honig, RCA Review 23, 567 (1962).

[5.35] W. P. Wood and J. M. Cork, Pyrometry, 2nd edition, McGraw-Hill, NY, 1941.

[5.36] B. J. Barnes, J. Opt. Soc. Am. 56, 1546 (1966).

[5.37] American Institute of Physics Handbook, 2nd edition, p. 6-58.

[5.38] J. M. Abraham and B. Deviot, J. Less-Common Metals 29, 311 (1972).

[5.39] V. Yu Voskresenskii, V. E. Peletskii, and D. L. Timrot, High Temperature 4, 39 (1966).

[5.40] S. Wieder, The Foundations of Quantum Theory, Academic Press, NY, 1973.

[5.41] J. R. Clement and E. H. Quinnell, Rev. Sci. Instr. 23, 213 (1952).

[5.42] R. L. Powell, W. J. Hall, and H. M. Roder, J. Appl. Phys. 31, 496 (1960).

[5.43] P. della Porta and T. Giorgi, Vacuum 16, 379 (1966).

[5.44] H. Diepers, O. Schmidt, H. Martens, and F. S. Sun, Phys. Lett. 37A, 139 (1971).

[5.45] P. B. Wilson, Z. D. Farkas, H. A. Hogg, and E. W. Hoyt, IEEE Trans. NS-20, 104 (1973).

Chapter 6

EXPERIMENTAL INVESTIGATION OF THERMAL TRANSPORT IN HIGH THERMAL CONDUCTIVITY NIOBIUM CAVITIES

6.1 Introduction

An experimental study of thermal transport from an outgassed Nb cavity surface to liquid helium was performed by measuring temperatures along a cavity surface with a localized heat source located on the cavity surface. The measurements were performed with the high thermal conductivity Nb cavities for which a measurable temperature rise was expected across the entire cavity surface; for the low thermal conductivity Nb cavities the temperature rise would have been confined to the region near the heat source.

The results were then analyzed using a modified version of the HEAT program to calculate the expected surface temperatures. The expected temperatures are calculated from three types of input: first, a set of input parameters and boundary conditions must be chosen that are appropriate to the experimental situation. In addition, a function for the thermal conductivity of the metal must be included in the program; the thermal conductivity of the Nb used in these experiments was well established, as reported in Figure 5.7. Finally, the thermal boundary resistance must be included in the program. The functional relationship between the power density and the rise of the surface temperature above the bath temperature was established in Chapter 4; however, the magnitude of the boundary resistance from Nb to liquid helium is not well known and depends upon the surface preparation, orientation, etc. Therefore, the magnitude of the boundary resistance used in the calculations was

varied by up to an order of magnitude about the values given in Section 4.4, in order to see if a good fit to the experimental data could be found. This procedure was successfully used to obtain reasonable matches to the experimental data for heat transport to both He I and He II. This investigation yielded two very important results: first, it provided justification for the use of the HEAT program to calculate surface temperatures; second, it provided a good estimate of the thermal boundary resistance for the electrodeposited cavities, which will be valuable in interpreting the microwave measurements presented in the next chapter.

6.2 Experimental Apparatus

The main factor that entered into the design of the apparatus was that the measurements needed to have sufficient spatial resolution to see the expected temperature variations; this meant that the thermometers and heater had to be kept relatively small; because high precision measurements were not required the apparatus was kept simple so that the experiments would be easy to perform and analyze.

The thermometers used here were the same type as those used for the thermal conductivity measurements (1/8-watt, 100Ω Allen Bradley carbon composition resistors placed in Apiezon N grease); the calibration procedure and calculation of temperatures was the same as discussed in Section 5.6. These thermometers are small in size (0.16" long and 0.062" in diameter) compared to the cup dimensions (0.94" long by 0.60" wide by 0.32" deep). Reliable surface temperature measurements may be made when each thermometer is oriented along a line of constant temperature; here the surface temperature along the length of each thermometer

will be fairly constant provided that the thermometers are not placed too close to the heat source and that they are oriented with their long axis perpendicular to the line between the thermometer and the heat source.

Experimentally, the radiation sensitivity of the thermometers made it impossible to locate a heater inside the cavity with the thermometers (the radiation sensitivity of these thermometers is discussed in Appendix A). Therefore the heater (a 1/4 watt carbon resistor) was placed on the outside of the cavity cup bottom and thermally isolated from the liquid helium bath in order that heat travel into the cavity. In fact this method of supplying heat was advantageous because the inside surface temperature at the heater location could be measured directly. The heater was located inside a metal cover (H in Figure 6.1) with teflon between the heater and the walls of the cover. Thermal contact between the heater and the Nb surface was made with Apiezon N grease; less than 1% of the total heater power was conducted along the small diameter constantan wires between the heater and the liquid helium. The heater assembly was pressed against the Nb surface (J in Figure 6.1) and sealed with epoxy (Tra-Bond BA-2151). During the low temperature tests up to 5 watts of power could safely be dissipated in the heater.

This heating method had several potential drawbacks. First, the HEAT model assumes that the heat is applied to the vacuum side of the test surface; in this case the temperature difference across the .030" thickness of the outgassed Nb was estimated to be quite small relative to the overall temperature rise of the Nb (see Section 4 of this chapter). A second consideration is that about 10% of the outer surface

of the Nb cup was covered by the heater assembly and was not in contact with the liquid helium; this was accounted for in the analysis of the results. The final concern is whether a significant fraction of the heater power escaped directly into the liquid helium instead of heating up the Nb. The thermal resistance between the covered heater and the liquid He was somewhat lower than that found for a heater located on the inside cavity surface, indicating that some of the heat probably did escape directly into the liquid helium. The heat leak was investigated by constructing a second heater tube assembly in which the heater was oriented perpendicular to the cavity surface with only one end of the heater in contact with the cavity surface. With this second heater assembly the contact between the heater and the cavity was considerably reduced, while the contact between the heater and the teflon shield was much better. The thermal resistance between the heater and the liquid helium with this new assembly increased by a factor comparable to the reduction in contact area between the heater and the Nb; if heat leaks directly through the heater box were significant then the thermal resistance from the heater to the liquid helium should have decreased with the second heater assembly. From these results, heat transfer directly from the covered heater to the helium bath was estimated at less than 10% of the total heater power.

A schematic of the experimental apparatus is shown in Figure 6.1. The apparatus was attached to the end of a 30" long vacuum pipe which was lowered inside the dewar. A diffusion pump system was then connected at the top of the vacuum pipe which provided a vacuum of

Figure 6.1 Schematic of apparatus used for thermal transport investigation.

A = Nb frame to which Nb cup is welded

B = stainless steel ring for attaching thermometer holders

C = .005" stainless steel thermometer holders

D = leads from thermometers to feedthrough

E = 8-pin instrumentation feedthrough

F = vacuum flange

G = indium seals

H = heater assembly

J = heater assembly restraint

K = radiation shield

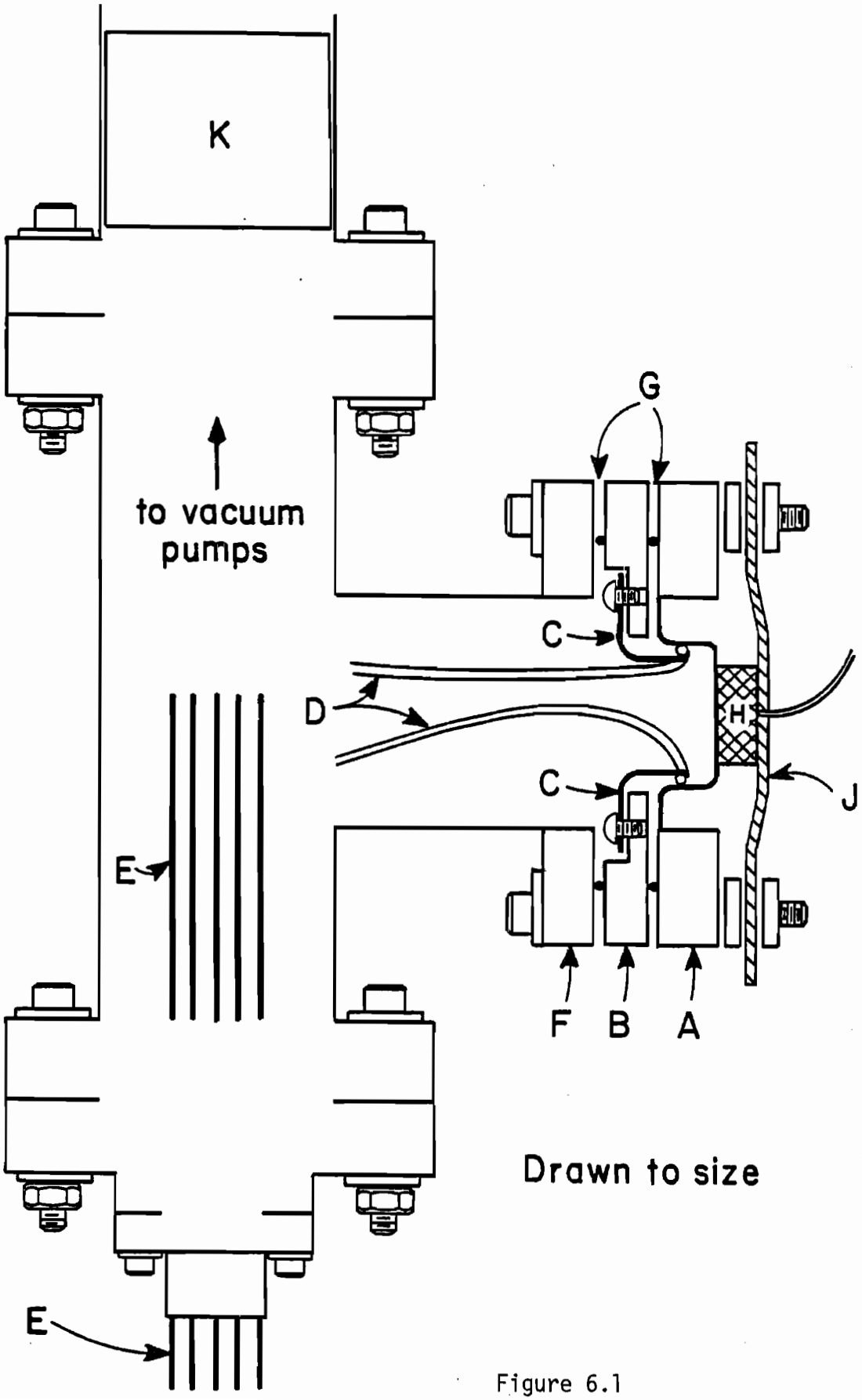

Figure 6.1

1×10^{-6} torr. A multi-pin feedthrough was located at the top of the dewar for wires from the apparatus. The Nb cup in its frame (A) is shown on the right side of the schematic. Next a ring (B) for attaching the thermometers was mounted to the frame with an indium seal. The thermometers were tied to 0.005" stainless steel pieces (C) which were bent to hold the thermometers in place against the Nb surface and then secured to the ring (B); for clarity, only two of the thermometers are shown in the figure. The thermometers made thermal contact with the Nb by careful application of Apiezon N grease to the Nb only. The leads from the thermometers were 15" long pieces of 0.002" diameter wire (D); the wires were made long enough to reach to the 8-pin UHV instrumentation feedthrough (E) even when the apparatus was fully apart. When the thermometers were all in place, a second indium seal was made to connect the cavity half and stainless steel ring to the vacuum flange (F). The remaining vacuum joints were all standard UHV flanges sealed with copper gaskets. The final step was to mount the heater assembly in place, as described previously.

The actual measurements were straightforward; the current and voltage across the heater resistor were monitored with digital multimeters in order to measure the power dissipated in the heater. The surface temperatures were measured by monitoring the resistance of the thermometers as for the thermal conductivity measurements. The minimum temperature rise that could be measured ranged from 0.002K at 4.2K to 0.0001K below 2.1K; the sensitivity was lowered if the pressure of the liquid helium bath was drifting.

6.3 Results and Discussion

Experimental results for this investigation of thermal transport from the high thermal conductivity Nb cavity halves to liquid helium are shown in Figures 6.2 and 6.3. In these figures heater power is plotted against the rise in inside surface temperature above the bath temperature. Representative results for thermal transport are given in Figure 6.2 for He I and in Figure 6.3 for superfluid He II. Each figure contains results for two different bath temperatures in order to demonstrate the variation in thermal transport with bath temperature.

The surface temperature rises are shown for two locations: the center of the cup bottom (marked by an x) and the center of a short sidewall (marked by a solid dot); for clarity only the results for one short sidewall are shown in Figures 6.2 and 6.3. The extremes in temperature rises on the cavity surface are represented by these two locations; the maximum temperature rise is expected at the heat source itself; the minimum temperature rise is expected far away from the heat source, near the outer edge of the cup. Measurements at the upper and lower edges of the four sidewalls showed temperature rises that were within 50% of the rise at the center of the short sidewalls; the temperature rise did decrease with distance from the heat source as expected. No significant variation was noted for the temperature rise at the cup bottom for different data runs. The temperature rise at the sidewall was observed to vary by up to 30% for different data runs, even when the apparatus was kept in the dewar at 77K between runs; possible causes of this variation include changes in any frost layer or other surface contamination.

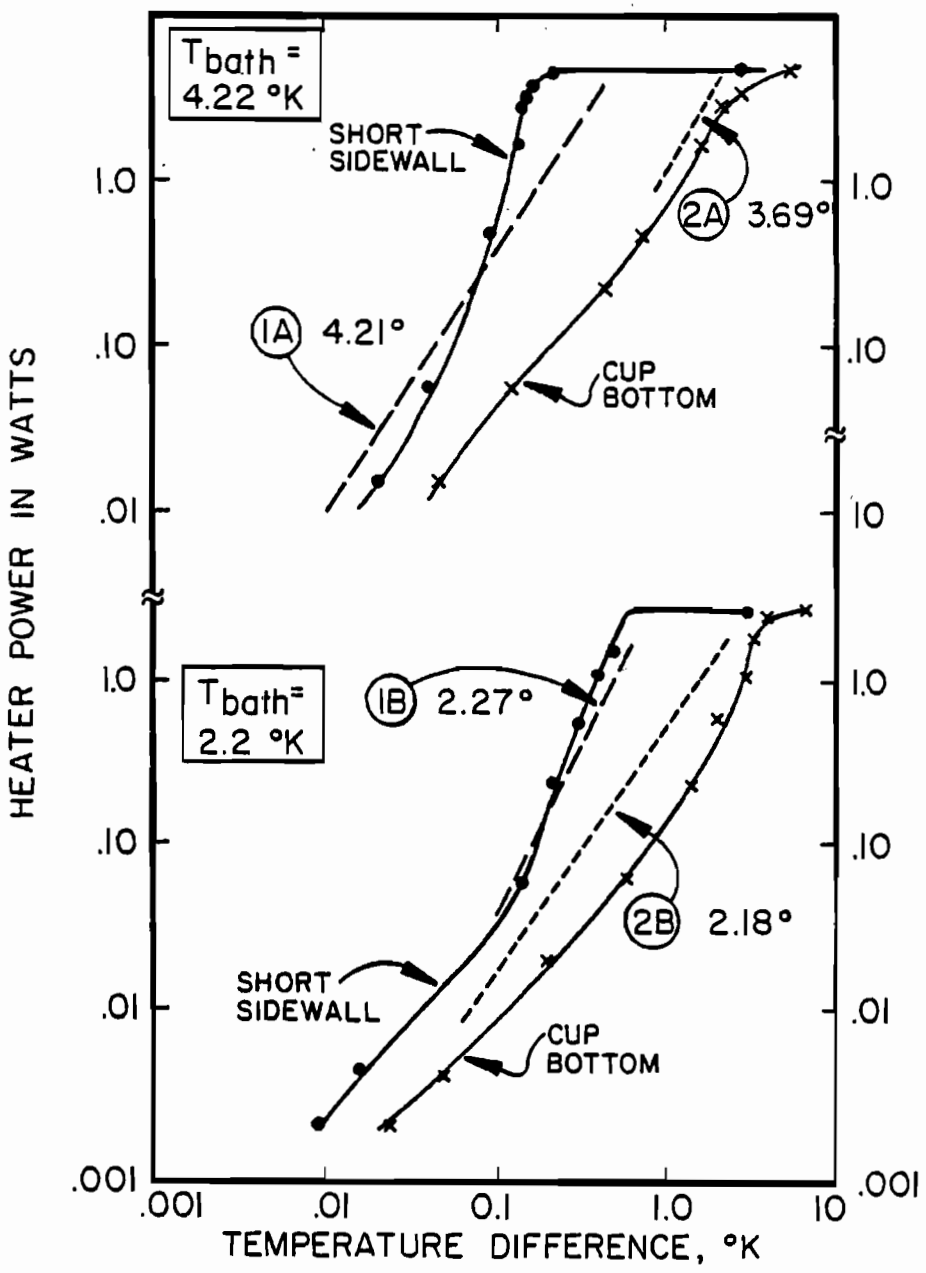

Figure 6.2 Thermal transport to He I from a high thermal conductivity cavity half.

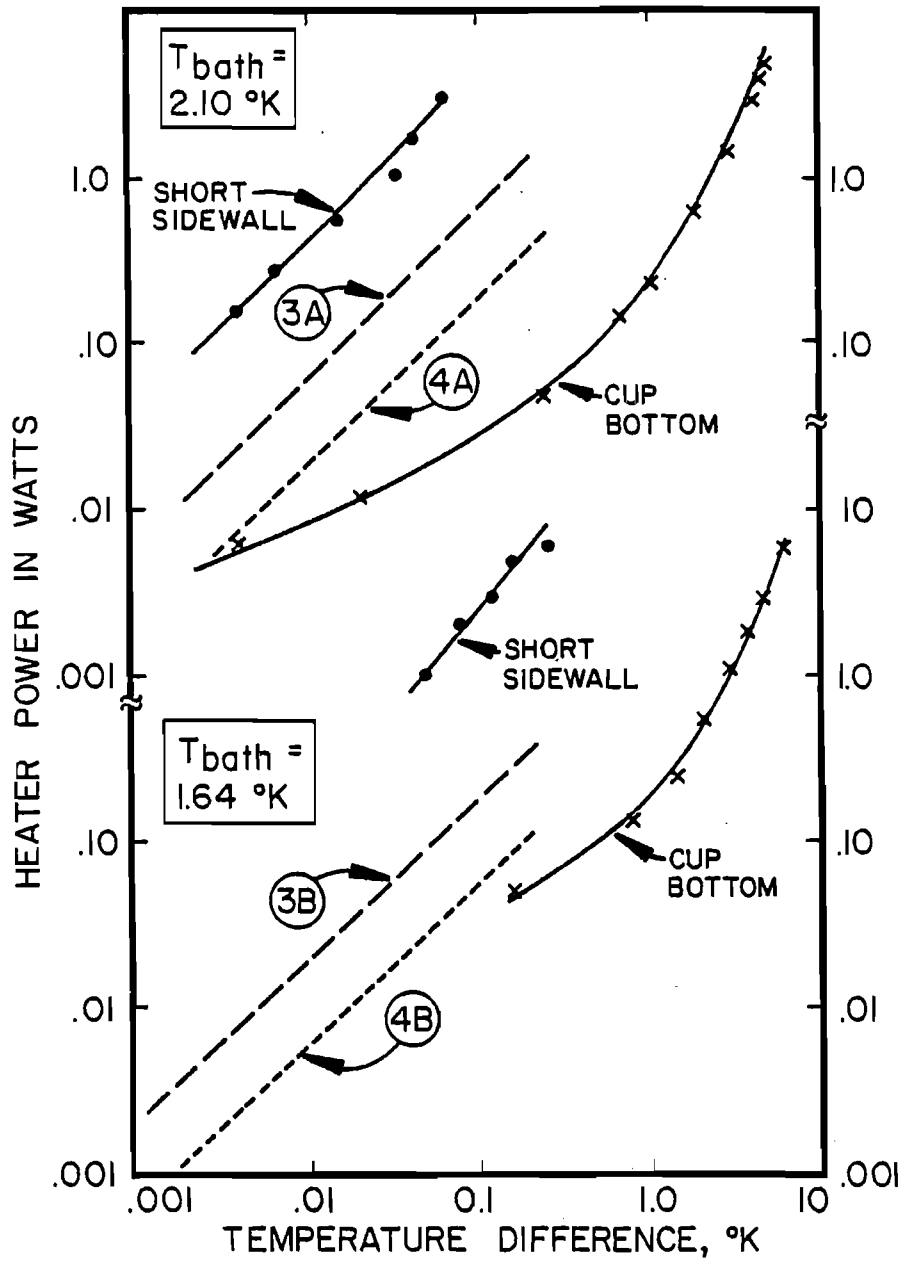

Figure 6.3 Thermal transport to He II from a high thermal conductivity cavity half.

A rough estimate of the expected boundary resistance between the Nb cavity half and the liquid helium may be performed by selecting typical curves for the boundary resistance (see Section 4.4) and then assuming a uniform heat flux from the Nb surface to the liquid helium; this procedure yields an estimated average temperature rise which should lie between the measurements shown in Figures 6.2 and 6.3 for the minimum and maximum surface temperature rises. The predictions included in Figure 6.2 for He I are from the following sources: curve #1 is from Lyon [4.10] for flat polished platinum in a vertical orientation; curve #2 is from Tsuruga and Endoh [4.11] for a horizontal copper cylinder. The predictions included in Figure 6.3 for Kapitza conduction to He II are taken from Table 4.1; these two curves give the highest and lowest values reported for Nb; curve #3 is for sample Nb2 from Mittag [4.28] and curve #4 is for specimen 3, run 1 reported by Wilkes [4.29].

These predictions for the average surface temperature rise are indeed consistent with the measurements shown in Figures 6.2 and 6.3. First note that the shape of the measured and predicted curves agree at low power levels; i.e., $Q \propto (\Delta T)^{1.65}$ for He I and $Q \propto (\Delta T)^{1.0}$ for He II. Furthermore, these predicted curves do lie within the range of measured surface temperature rises; the agreement is remarkably good since the reported values for the metal to liquid helium boundary resistance vary by up to an order of magnitude.

Finally, consider the high power results in Figure 6.2 for He I. At power levels of a few watts the cavity surface suddenly exhibits a large increase in surface temperature. This indicates that film boiling is taking place across the entire cavity surface. The levels

at which film boiling occurs range from 0.5 watt/cm^2 at 4.2K to 0.3 watt/cm^2 at 2.2K. These film boiling limits are consistent with the film boiling limits discussed in Chapter 4; the decrease in the film boiling flux with decreasing bath temperature is in agreement with other measurements. The film boiling limits for He II are expected to occur at about 1 watt/cm^2; this power level was out of the range of the experimental apparatus and hence film boiling could not be studied for He II.

To summarize, thermal transport from the Nb cavity half to both liquid He I and He II is in qualitative agreement with the predicted behavior. In addition, film boiling occurs in He I as expected.

6.4 Interpretation of Results: HEAT Calculations

The HEAT program described in Section 2.4 was modified for analysis of the heat transport measurements by using dc heat applied to a localized area at the center of the disk as the heat source. A schematic of the configuration used for the calculations is shown in Figure 6.4. The cavity half was assumed to be a disk whose thickness was the same as the cavity cup-bottom, and whose radius was chosen to give the same surface area as an X-band muffin-tin cavity half. Heat is applied uniformly over a surface area equal to that in the actual thermal transport study. Heat flows out to the liquid helium from the bottom and side walls; heat is not allowed to flow out from the center of the bottom surface in order to account for the presence of the heater assembly. The HEAT calculations were performed by dividing the disk into a mesh with $N_z = 10$ and $N_r = 40$.

For a given power level, the HEAT program determines the equilibrium temperature distribution from the temperature dependent functions for thermal conductivity and thermal boundary resistance. The thermal

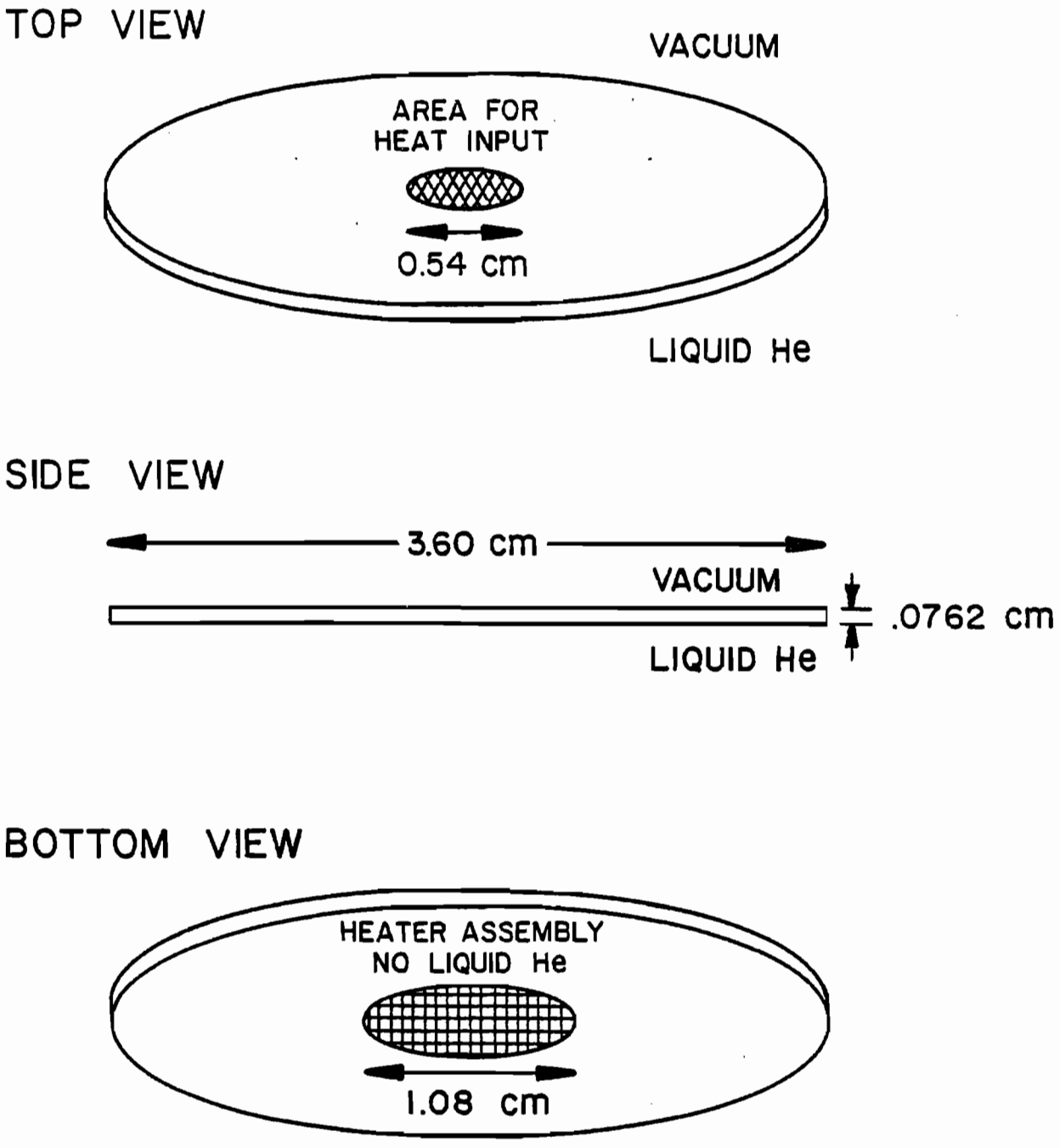

Figure 6.4 Model used in HEAT calculations. Scale 3:1.

conductivity for the outgassed Nb is assumed to be well known: the thermal conductivity between 1.4K and 3.0K was taken from the results shown in Figure 5.7 for a test strip outgassed at 1900C in a vacuum of 1×10^{-9} torr; the thermal conductivity was extended to higher temperatures by constructing a curve with the same temperature dependence as measured by Oota et al. (Reference [3.16], sample Nb6300). The maximum heat flux to the liquid helium was set by the film boiling limit which is specified as an input parameter. The dependence of the boundary resistance upon the surface temperature rise is fairly consistent for all experiments, as discussed in Chapter 4; the magnitude of the boundary resistance at a given bath temperature was varied to see if a good fit to the experimental results could be obtained from the HEAT program.

Reasonable fits to the experimental results for heat transport to both He I and He II were obtained from calculations with the HEAT program. The experimental data and HEAT calculations for He I at 4.2K and He II at 2.1K are shown in Figure 6.5. The experimental results shown in Figure 6.5 are for the center of the cup-bottom, and a short sidewall. The calculated inside surface temperature rises shown in Figure 6.5 are for the center of the disk and the outer edge of the disk; the distance to the sidewall is about the same as the radius of the disk.

The fit for He I at 4.2K (shown in Figure 6.5) was generated by taking $Q/A = 1.10\times(\Delta T)^{1.65}$ watt/cm^2; this value is 1/2 that reported by Lyon [4.10] and lies midway between curves 1A and 2A in Figure 6.2; the film boiling limit was taken to be 0.5 watt/cm^2. Reasonable fits to the remaining He I data were found with $Q/A \propto (\Delta T)^{1.65}$; the proportionality constant range from 1.10 watt/cm^2 at 4.2K to 0.25 watt/cm^2

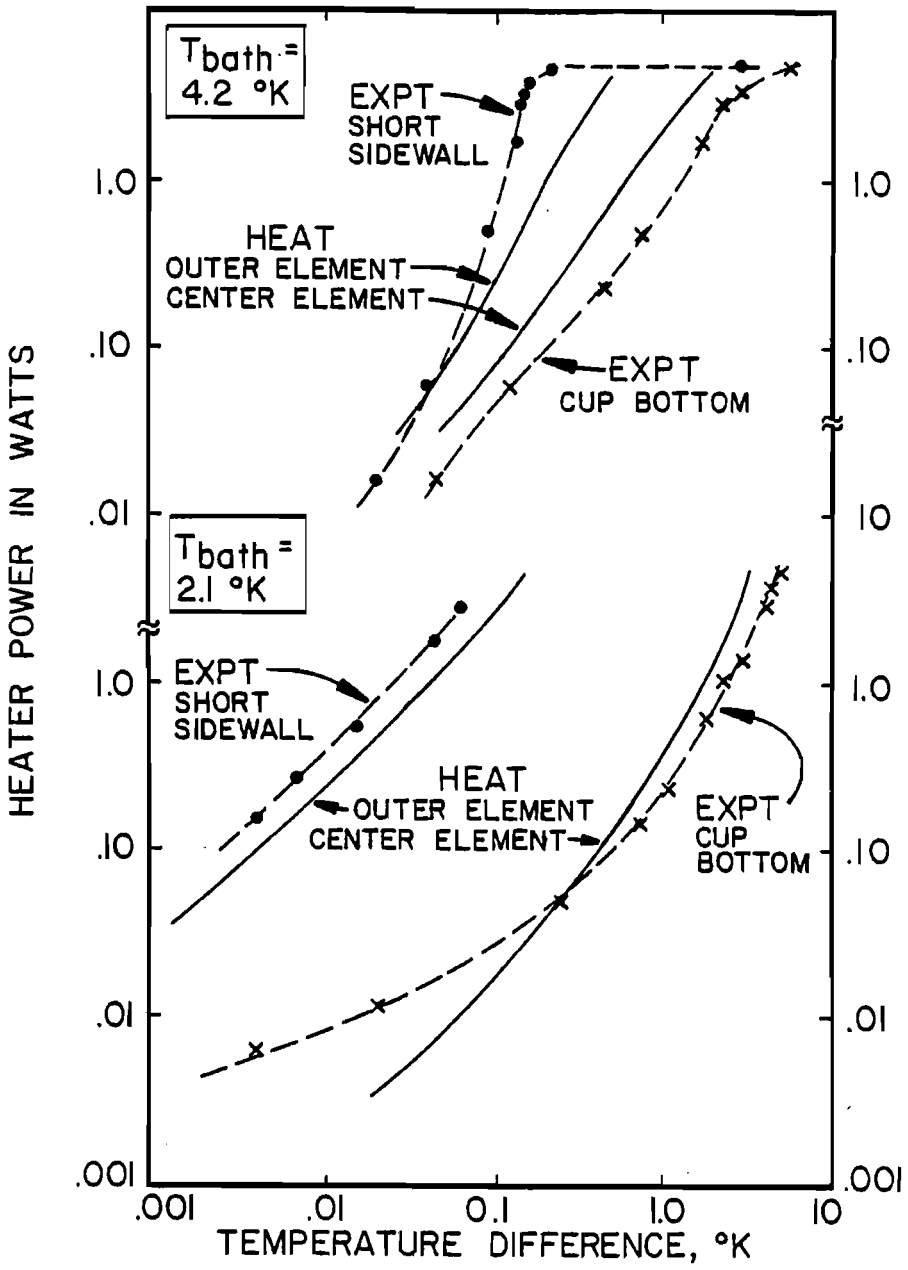

Figure 6.5 Thermal transport from a high thermal conductivity cavity half and HEAT calculations to fit the data.

at 2.2K.

The fit for He II at 2.1K (shown in Figure 6.5) was generated by taking H_k = 0.420 watt/cm^2-K; this value lies midway between curves 3A and 3B in Figure 6.3; the film boiling limit was taken to be 1.0 watt/cm^2. Reasonable fits to the remaining He II data were found with $H_k \propto T_b^3$ or $Q/A = 0.0113 \ (T_s^4 - T_b^4)$ watt/cm^2-K^4.

The HEAT calculations agree well with the experimental results in spite of the approximations that are made in modeling the experimental situation: for instance, the disk used in the calculations could not account for the rectangular shape or corners of the muffin-tin cavity. Furthermore, the thermal conductivity of the muffin-tin cavity varied with location, since during the UHV outgassing process the sidewalls are at a higher temperature than the cup bottom; the thermal conductivity used in the calculations corresponded to that for the cup bottom. Finally, the calculated temperatures shown in Figure 6.5 were for the inner and outer elements of the disk, while the experimental results shown in Figure 6.5 were for the center of the cup bottom and the center of a short sidewall; the distance from the center of the cup-bottom to the center of a short sidewall is about the same as the radius of the disk, but the center of the short sidewall is in fact not located at the outermost edge of the cavity.

These calculated fits to the data are fairly sensitive to changes in the functions chosen for the thermal conductivity and boundary resistance. For example, decreasing the boundary resistance lowers all of the surface temperature rises, with the surface temperature rise changing much more at the outer edge of the disk than at the center

element. The HEAT program is very useful then to quantify different aspects of the thermal transport problem. For instance, the HEAT calculations provided a means of calculating the temperature difference across the thickness of the Nb surface; in the cases shown in Figure 6.5 the temperature drop across the thickness was less than 2% of the total temperature rise; such a low temperature drop was expected for the high thermal conductivity Nb.

In conclusion, the HEAT calculations are useful in analyzing thermal transport in the Nb cavities, where both the thermal conductivity and boundary resistance must be taken into account. In the next chapter the HEAT program will be used to understand the microwave properties of X-band muffin-tin cavities; there the heat source will be losses due to the surface resistance of the metal and the defects in the presence of electromagnetic fields.

Chapter 7

MICROWAVE MEASUREMENTS OF CAVITY PERFORMANCE

7.1 Introduction

The aim of this investigation is to demonstrate improved performance of superconducting cavities with regard to thermal-magnetic breakdown; as discussed in Chapter 2, raising the thermal conductivity of the metal is expected to help stabilize localized lossy areas on the cavity surface against heating and subsequent thermal-magnetic breakdown.

Three types of X-band muffin-tin cavities were prepared from electrodeposited Nb cups for microwave testing: one cavity was made from unannealed Nb cups which were welded directly into Nb frames; the frames were made from commercial grade Nb since the frames are outside the field zone. Two cavities were made with Nb cups outgassed as described in Chapter 5. The third type of cavity was made by annealing Nb cups following the standard procedure and then engassing the Nb in a partial pressure of oxygen, as described in Section 5.7.

Microwave measurements were performed for bath temperatures between 4.2K and 1.4K; at each bath temperature,the cavity Q_0 was studied as a function of the power dissipated in the cavity; the cavity field levels were computed from the measurements of Q_0 and the dissipated power.

The microwave performance of the Nb cavities is significantly improved by raising the thermal conductivity of the Nb; much higher fields and power levels may safely be sustained with the high thermal conductivity Nb cavities. In Section 5 of this chapter, the HEAT program will be used to examine the thermal transport processes responsible for the measured microwave performance of the different types of cavities.

7.2 Experimental Apparatus

The cavity geometry, the test station, and the microwave devices used in the low temperature microwave cavity tests will be described in this section. In the following section the methods used to analyze the data will be discussed.

A schematic of an assembled cavity is shown in Figure 7.1. The cavity is constructed from two Nb frames which have Nb cups welded into them; before assembly, each cup area was chemically polished to remove 2μ of material. The frames were attached with indium seals to the Nb ring as shown in Figure 7.1; the assembly was then immediately attached to the test station with another indium seal and placed under high vacuum; in order to give the vacuum pumps times to reach their ultimate pressure the cavity and test station were kept at room temperature overnight; the cavity and test station were then lowered into a magnetically shielded dewar (<10 milligauss) for the low temperature tests.

The cavity fields may be described qualitatively by the equations for a perfect rectangular cavity; the fields are altered by the presence of the gap for the particle beam. The fundamental accelerating mode for a rectangular cavity is the TM_{110} mode. Let the dimensions of the cavity in the x, y, and z directions be a, b, and c respectively; also, locate the origin of the coordinate system at the center of the cavity. Then the fields for the TM_{110} mode in a rectangular cavity are given by (see Reference [7.1] for example)

$$E_z \propto \cos(\tfrac{\pi x}{a})\cos(\tfrac{\pi y}{b}),\ H_x \propto \cos(\tfrac{\pi x}{a})\sin(\tfrac{\pi y}{b}),\ \text{and}\ H_y \propto \sin(\tfrac{\pi x}{a})\cos(\tfrac{\pi y}{b}).$$

E_x, E_y, and H_z are all zero in the TM_{110} mode. Note that the peak electric

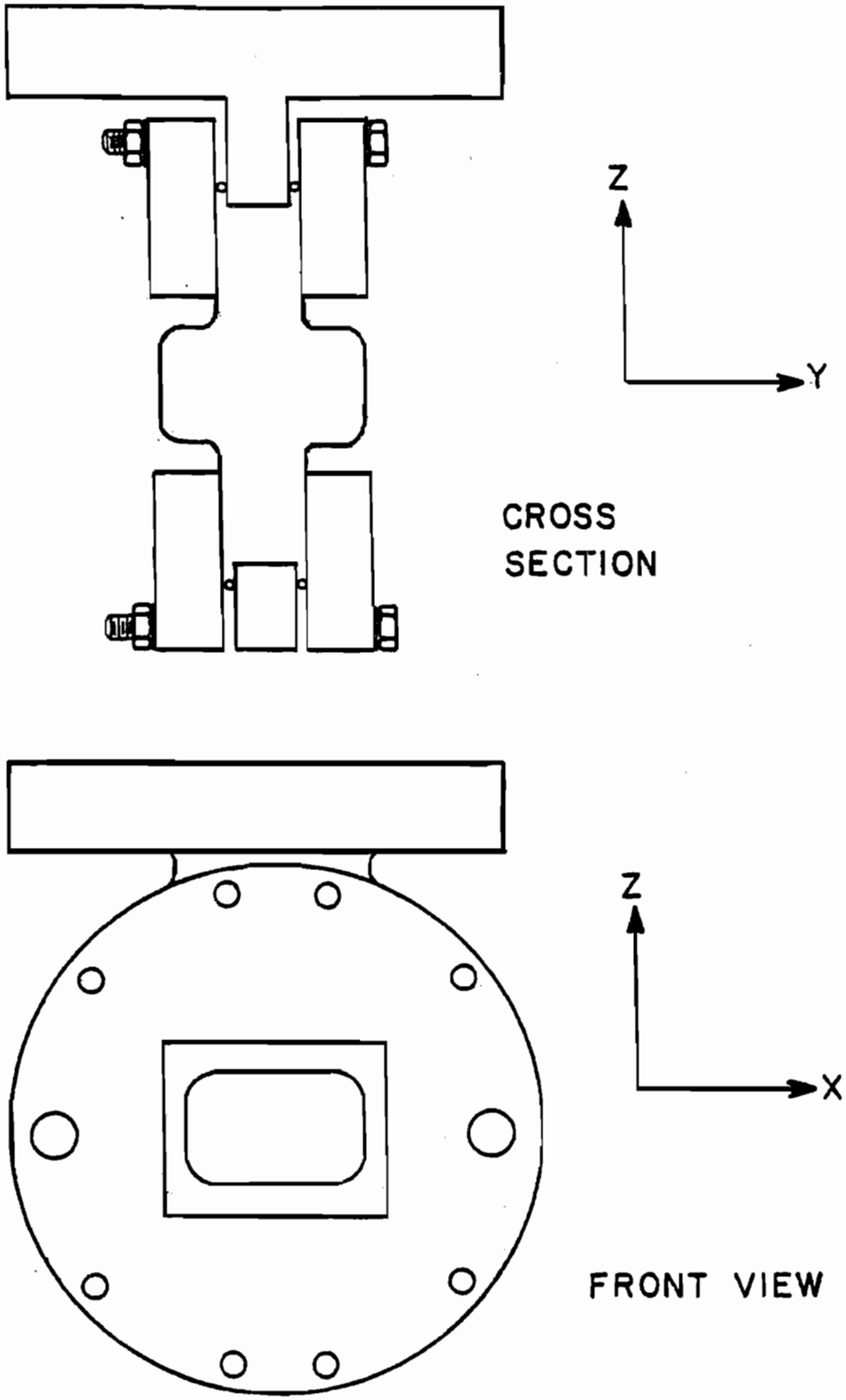

Figure 7.1 Assembled single cell X-band muffin-tin cavity (drawn to size).

field is located on the z-axis, through the center of the cavity. Also note that high magnetic fields are located at the cavity walls.

The dimensions of the mounting ring were chosen to satisfy two criteria: first, the microwave fields outside the cup region had to be severely attenuated to eliminate losses due to currents at the indium seals. Second, the area inside the ring forms a cylindrical cavity itself; the dimensions of the ring were therefore chosen to guarantee that the "ring modes" were not close in frequency to the fundamental cavity mode.

The microwave properties of the cavity were studied with a 50Ω coaxial transmission line with adjustable coupling to the cavity. The transmission line and coupling used in the low temperature tests are illustrated in Figures 7.2 and 7.3. Figure 7.2 is a schematic of the top of the transmission line, drawn to half scale. Figure 7.3 is a schematic of the bottom of the transmission line and coupling to the cavity, drawn to full scale. The transmission line was 32" long in order to accommodate sufficient liquid helium for the low temperature tests; the long straight section from the top of the transmission line to the cavity is not shown in these figures. Only the important features of the transmission line will be mentioned here: first, the entire transmission line was contained inside stainless steel tubing; a small vacion pump was connected to the transmission line in order to obtain a pressure of 1×10^{-8} torr in the line and cavity at room temperature. Microwave power entered the transmission line at the top of the test station through the UHV coaxial feedthrough shown in Figure 7.2; the entire transmission line was suspended from the feedthrough as shown.

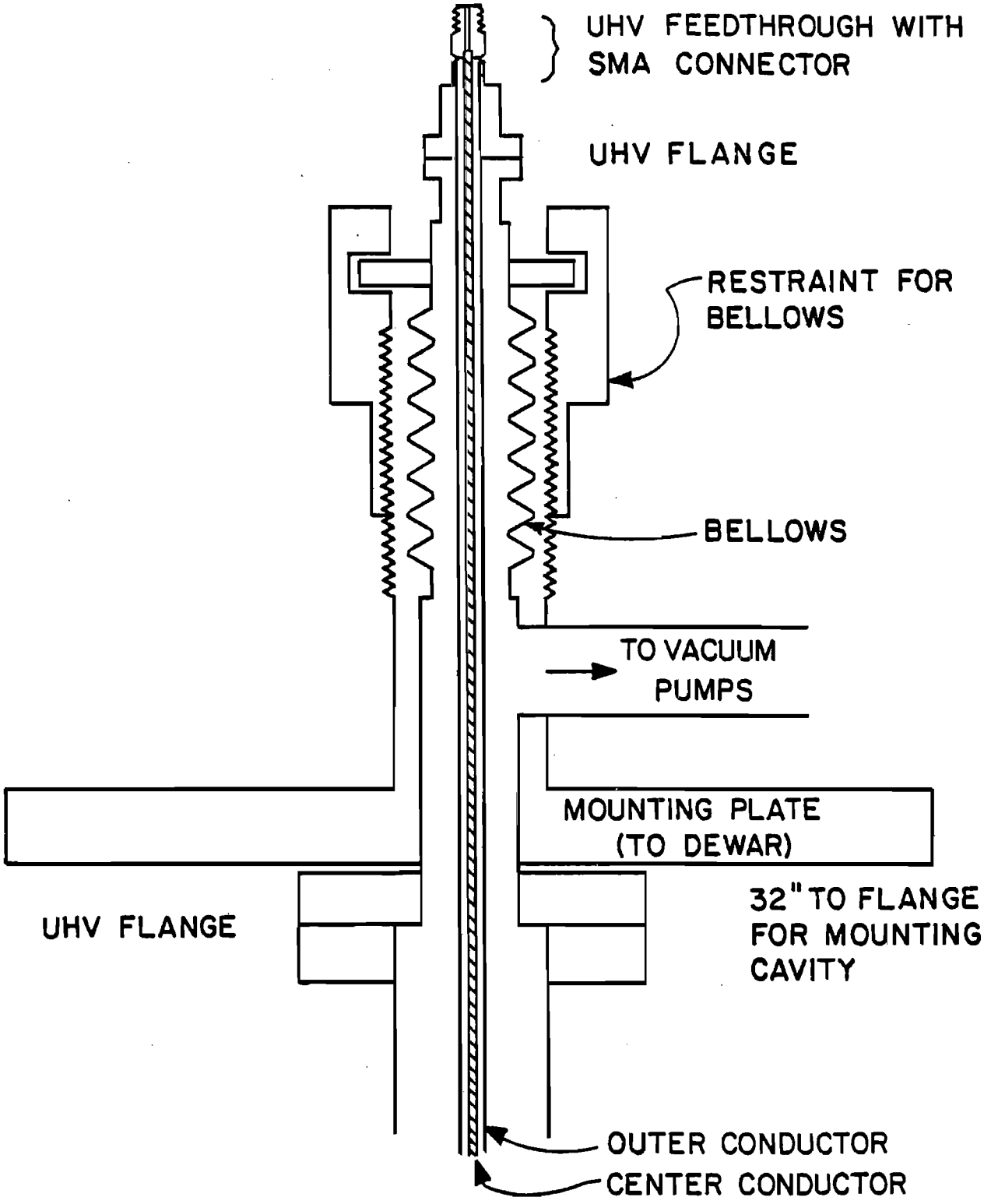

Figure 7.2 Schematic of variable length transmission line for X band (scale 1:2).

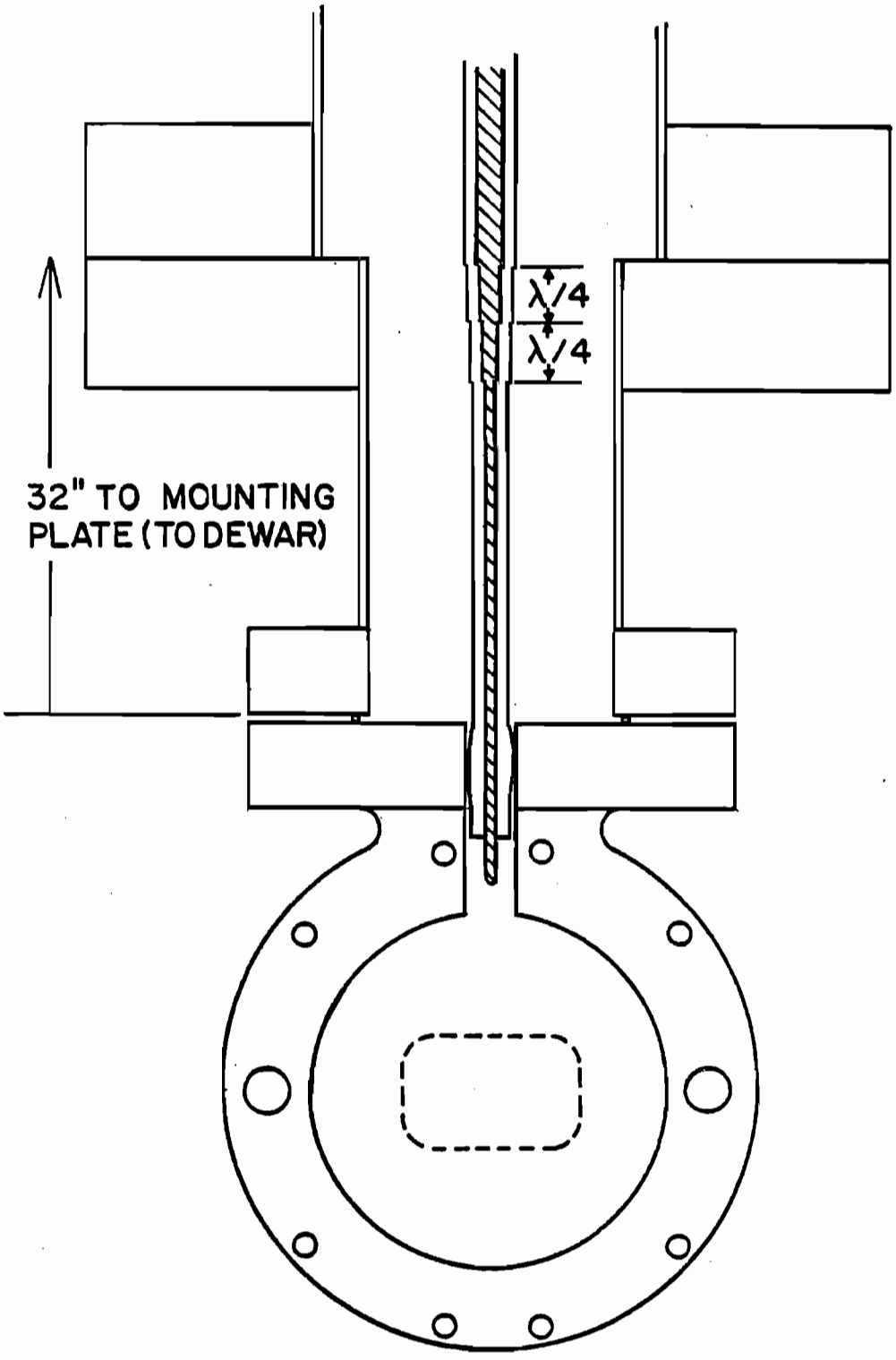

Figure 7.3 Schematic of coaxial coupling to X-band cavity (drawn to size).

The bellows arrangement shown in Figure 7.2 was used to vary the extension of the transmission line into the cavity. Just above the cavity the dimensions of the transmission line were changed in three steps each, as indicated in Figure 7.3; the steps were each one-quarter wavelength apart ($\lambda = c/f$, where the frequency, f, is 8.56 GHz). The outer conductor made contact with the cavity through a hole reamed in the top of the cavity assembly; the outer conductor was slotted just above the end of the transmission line and then bowed outwards slightly to guarantee good electrical contact with the cavity. The center conductor extended further into the cavity, as shown, and coupled to the electric field in the cavity.

Finally, a diagram of the devices used to control and monitor the microwave signal at the top of the transmission line is shown in Figure 7.4. The path between the microwave source and the transmission line is indicated with a heavy line; the remaining connections are for the devices that control the signal to the transmission line. The microwave source was an 8-12 GHz sweep generator which was used in the continuous wave mode for the low temperature tests. The microwave signal passed through a directional coupler, where a fraction of the signal was used to monitor frequency. The signal was amplified 30dB by a TWT (traveling wave tube) amplifier which had a maximum output of 1 watt; a circulator was used at the TWT output to protect it from returning power. The signal then went to a PIN diode modulator; the output of the PIN diode depended upon the signal input at its third port; thus the amplitude and shape of the signal to the transmission line was controlled electronically with the signal to the third port of the PIN diode. Finally, the modulated signal was amplified by a 35dB TWT with a maximum output

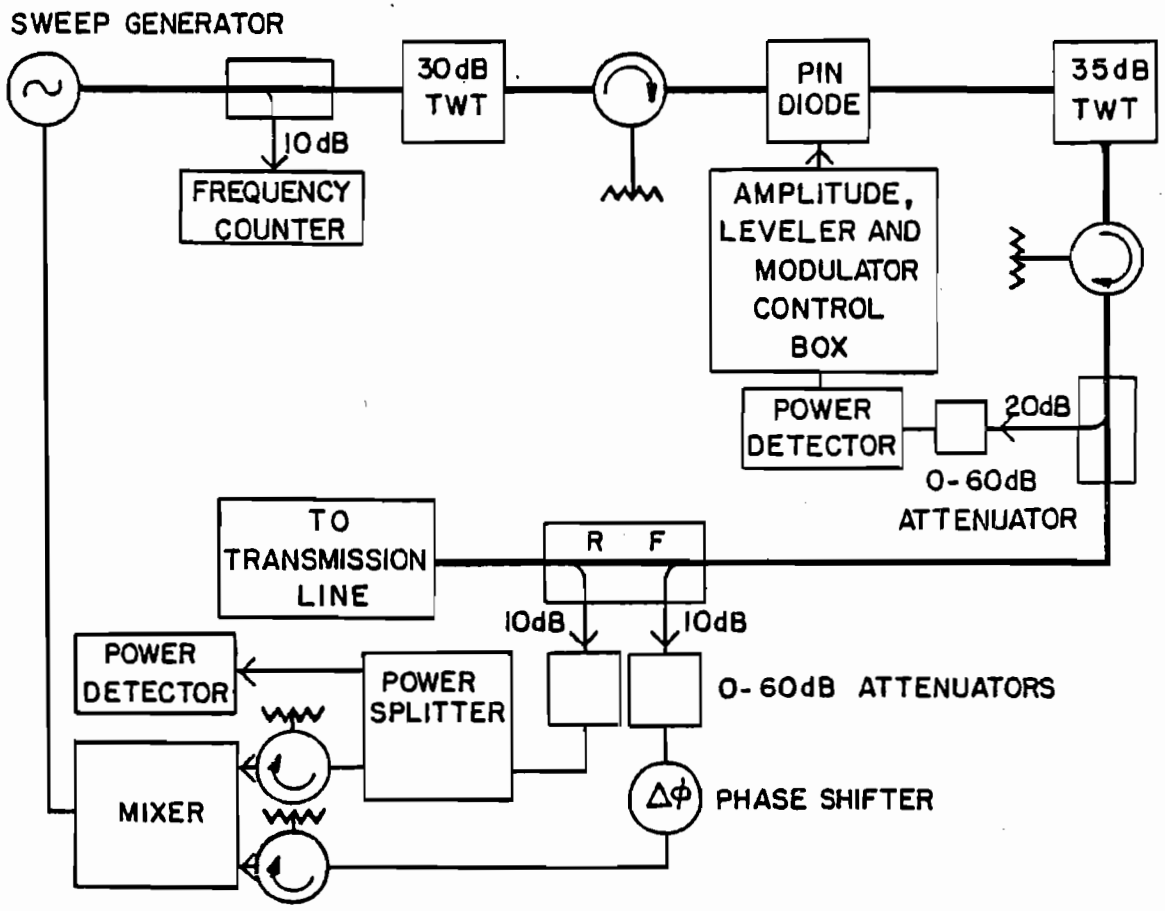

Figure 7.4 Schematic of RF electronics.

of 20 watts. The amplified signal then passed through two more directional couplers to the UHV feedthrough and transmission line. To maximize the power available at the transmission line, the second TWT was placed very close to the dual directional coupler; however, losses in the directional couplers and a short coaxial cable (between the TWT and the dual directional coupler) still amounted to about 30% of the output from the TWT. The signal was attenuated by 50% between the feedthrough and the bottom of the transmission line because of losses in the line that were due to the finite electrical conductivity of the center conductor. Thus 7 watts was the maximum power available at the cavity. The output power level of the second TWT was monitored by the electronics control box with a directional coupler placed at the output port of the TWT; the electronics control box regulated the signal to the PIN diode in order to hold the output level constant in the event of amplifer drifts, etc. The dual directional coupler was connected directly to the feedthrough and was used to monitor the forward and reflected signals at the top of the transmission line. The reflected signal was split in half: one half went to a crystal diode detector where the power level was monitored with an oscilloscope; the other half went to one arm of a double balanced mixer. The forward signal passed through an adjustable phase shifter (a variable length line) and then to the second port of the mixer. The mixer output was adjusted by varying the amplitude and relative phase of the two input signals to the mixer; the output of the mixer was used to maintain the frequency of the sweep generator signal at the resonant frequency of the cavity.

A network of Allen-Bradley carbon composition resistance

thermometers placed on the outside of the cavity was used to monitor temperature changes due to localized heating of the cavity surface. A constant current was supplied to the thermometers and the voltage across each thermometer was amplified and displayed on an oscilloscope via a multiplexer. During the low temperature tests, the power to the cavity was pulsed; the thermometer output was thus examined for changes that were synchronous with the pulsing of the cavity; if the thermometer was located where significant heating of the cavity was occurring then measurable signals were observed. The heating of the cavity surface could thus be mapped out and also studied as a function of the power dissipated in the cavity.

7.3 Measurement Technique and Analysis

The microwave testing of the cavity performance consisted of measuring the cavity Q_o as a function of the power dissipated in the cavity. The cavity Q_o was measured by the decrement method: first, a microwave signal is used to excite the resonant cavity; then the incident signal is turned off and the signal radiated by the cavity into the transmission line is monitored as it decays exponentially. This is illustrated in Figure 7.5 for two different values of the coupling to the cavity.

These microwave measurements were interpreted using an equivalent circuit for the cavity and transmission line, as shown in Figure 7.6. The cavity off resonance is represented approximately as an open circuit in series with a lossless transmission line of characteristic impedance Z_o. At resonance the cavity is represented as a resistive load Z_c located at the coupling port. A coupling parameter is defined by the

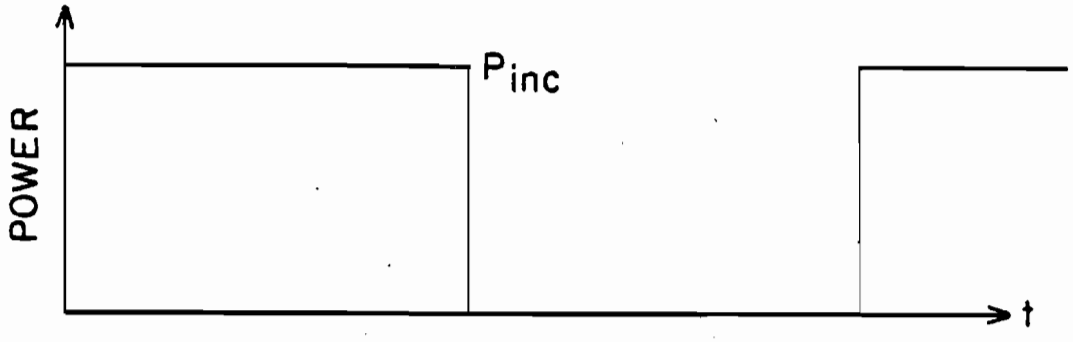

Figure 7.5a Reflected power off resonance

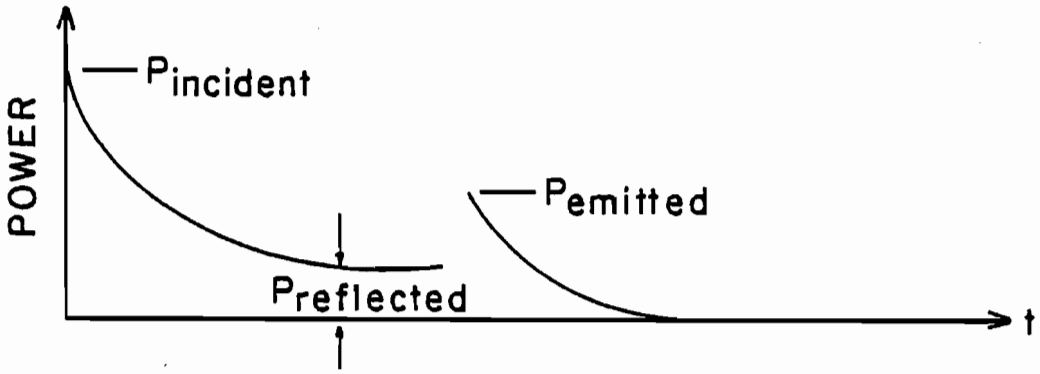

Figure 7.5b Reflected power at resonance, $\beta < 1$

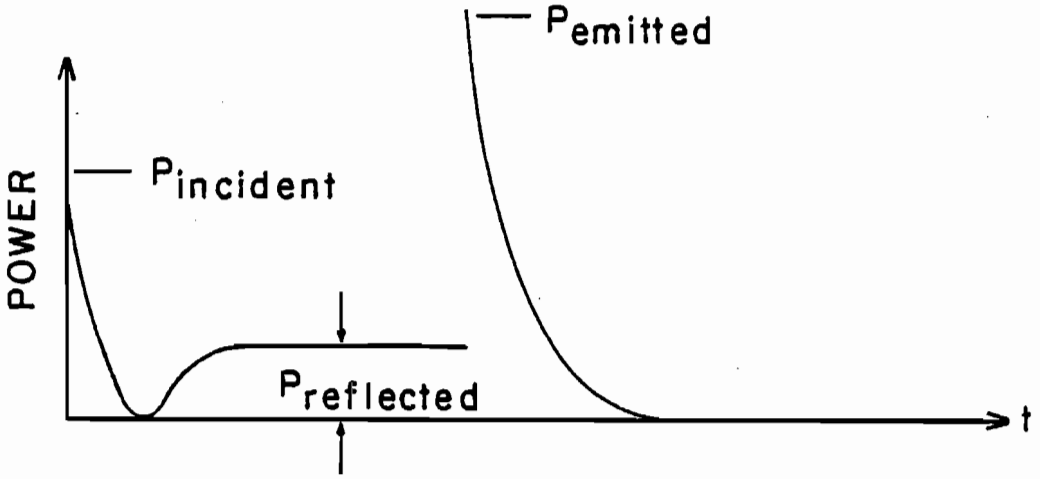

Figure 7.5c Reflected power at resonance, $\beta > 1$

Figure 7.5 Decrement method for measuring Q of resonant cavity.

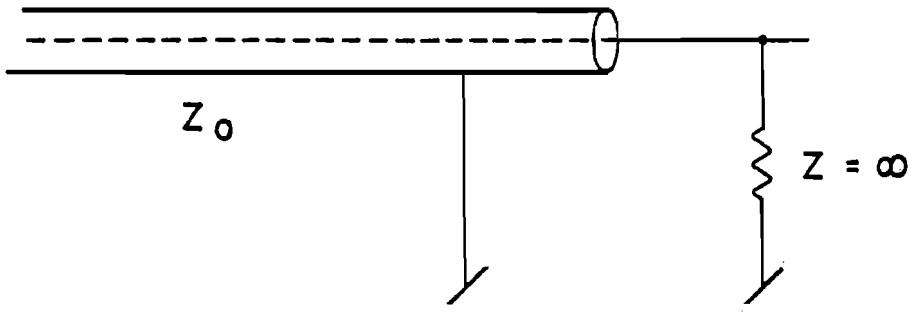

Figure 7.6a Cavity off resonance

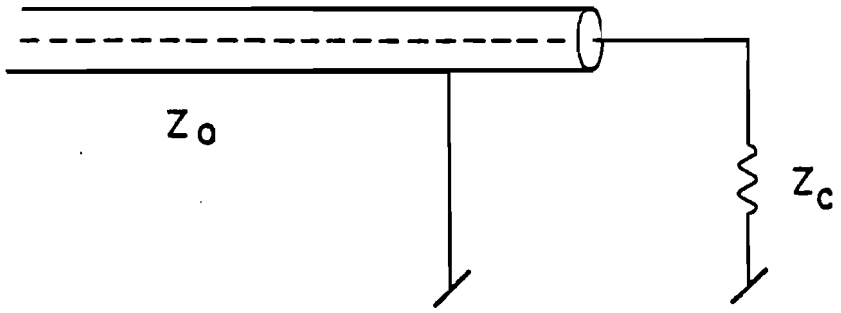

Figure 7.6b Cavity at resonance

Figure 7.6 Equivalent circuit of a one-port cavity.

equation $\beta = Z_o/Z_c$. The various power levels in Figure 7.5 may be related to β using the equivalent circuit. For instance, the reflected power is given by (see Reference [7.2], Eq. 4.63 for example)

$$P_{refl} = \frac{(1-\beta)^2}{(1+\beta)^2} \times P_{inc} .$$

The power emitted by the cavity at the instant the incident power is changed to zero is also related to β, as follows: let I_c be the current at the coupling port when the incident power is switched off; because I_c cannot change instantaneously then

$$P_{emitted} = I_c^2 \times Z_o = \frac{P_{inc} - P_{refl}}{Z_c} \times Z_o = \frac{4\beta^2}{(1+\beta)^2} \times P_{inc} .$$

The coupling parameter, β, may thus be computed from measured curves such as are shown in Figure 7.5. In fact, β may be computed from any two of the power levels P_{inc}, P_{refl}, and $P_{emitted}$. In practice, the coupling parameter was usually adjusted to be close to unity, in which case P_{refl} was quite small; thus the most accurate value for β was that computed from $P_{emitted}$ and P_{inc}.

The power dissipated in the cavity, P_{diss}, was computed from β and P_{inc} using the formula

$$P_{diss} = P_{inc} - P_{refl} = \frac{4\beta}{(1+\beta)^2} \times P_{inc} .$$

This formula assumes that P_{inc} is measured at the coupling port at the bottom of the transmission line, whereas the power levels were actually measured at the top of the transmission line with the reflected power arm of the dual directional coupler; the measured values for P_{inc} were therefore corrected for the attenuation between the coupling port at

the bottom of the transmission line and the reflected power arm of the dual directional coupler. The magnitude of the attenuation was determined experimentally at low temperatures by sending a signal down the transmission line while the cavity was off resonance; with the cavity acting as an open circuit the microwave signal returning to the top of the transmission line was attenuated by two traverses of the line.

The cavity Q_0 was computed from the coupling constant, β, and the decay time for the emitted power signal from the formula

$$Q_0 = (1+\beta) \times \omega\tau \ .$$

The factor $(1+\beta) = \frac{Z_c+Z_0}{Z_c}$ accounts for the fact that some of the stored energy in the cavity radiated out the transmission line and caused the stored energy in the cavity to decay faster than if the cavity were not loaded by the transmission line.

Finally, P_{diss} and Q_0 were used to calculate the electromagnetic fields in the cavity. The average effective accelerating gradient is given by the formula

$$E_{acc}^2 = \frac{P_{diss}}{\text{cavity length}} \times \left(\frac{R}{Q_0}\right) \times Q_0$$

R/Q_0 is called the normalized effective shunt impedance. R/Q_0 depends only upon the cavity shape, scaling linearly with frequency for a given cavity shape; R/Q_0 is independent of the cavity Q_0. $R/Q_0 = 9600$ ohms/meter for a single cell muffin-tin cavity at 8.76 GHz [7.3]. The electromagnetic fields in the cavity are directly proportional to E_{acc}; in particular, the peak surface magnetic field, H_p, is given by $H_p = 64 \times E_{acc}$, where H_p is in Oersteds and E_{acc} is in units of 1×10^6 volts/meter [7.4].

The precision of these measurements and computations for P_{diss}, Q_o, and E_{acc} are limited both by measurement errors in the power levels and the decay time, and by systematic errors caused by reflections in the transmission line. The measurement error was less than 10%, and arose from two main sources; the first was any departure of the power detector from "square law" behavior. The second source of error arose if the cavity was heating significantly during the microwave pulse; in that case the cavity was cooling after the incident signal was turned off, and the decay time would therefore increase somewhat with elapsed time.

To further investigate the measurement error a second UHV feed-through was added directly to the mounting ring for use as a transmission probe. Of particular concern here were possible errors due to the fact that the variable coupling was adjusted considerably during the course of the measurements; at high dissipated powers heating of the cavity surface caused the cavity Q_o to fall, requiring that the probe be extended further into the cavity in order to keep the coupling near unity. The microwave measurements with two probes were then analyzed in terms of an equivalent circuit with two coupling ports; the second probe was very weakly coupled to the cavity ($\beta_2 < 0.05$). The calculated values for E_{acc} were then compared with the signal from the fixed transmission probe, which should be proportional to the electric field at the probe; the results agreed to within 5% for all power levels, indicating that the calculations for P_{diss}, Q_o, and E_{acc} are acceptable.

The reflections in the transmission line were responsible for a systematic error in the results. The reflections in the feedline were estimated by measuring the ratio of the reflected to forward power at

the dual directional coupler as a function of frequency. If the only reflection is at the cavity (acting as an open), then this ratio should be independent of frequency with a magnitude determined by the attenuation of the transmission line. If reflections also occur at the feedthrough, for instance, then this ratio will vary as the frequency is changed due to interference effects; the range of minimum and maximum values of this ratio will increase if the magnitude of the reflections in the transmission line are increased. A circuit model was developed to investigate the possible sources of reflections in the transmission line; the model is discussed in detail in Appendix B. Formulas are also developed in Appendix B that may be used to estimate the errors in the calculated values of P_{diss}, Q_o, and E_{acc} due to reflections in the transmission line. For the transmission line as used in this study the error in P_{diss} is negligible; the uncertainty in Q_o is estimated to be about 5%, and the uncertainty in E_{acc} is estimated to be about 2% (refer to Case III of Table B.1).

7.4 Results and Discussion

Experimental results for the three types of electrodeposited cavities described in the introduction to this chapter are presented in Figures 7.7, 7.8, and 7.9; Figure 7.7 shows results for a test of the unannealed cavity; Figure 7.8 shows results for a test of the annealed and engassed cavity; Figure 7.9 shows results for a test of an outgassed cavity. In these figures the peak surface magnetic field, H_p, is plotted against the square root of the dissipated power in the cavity (recall that H_p/E_{acc} = 64 Oe/1×10^{6}V/meter); note that the scales for each figure are different.

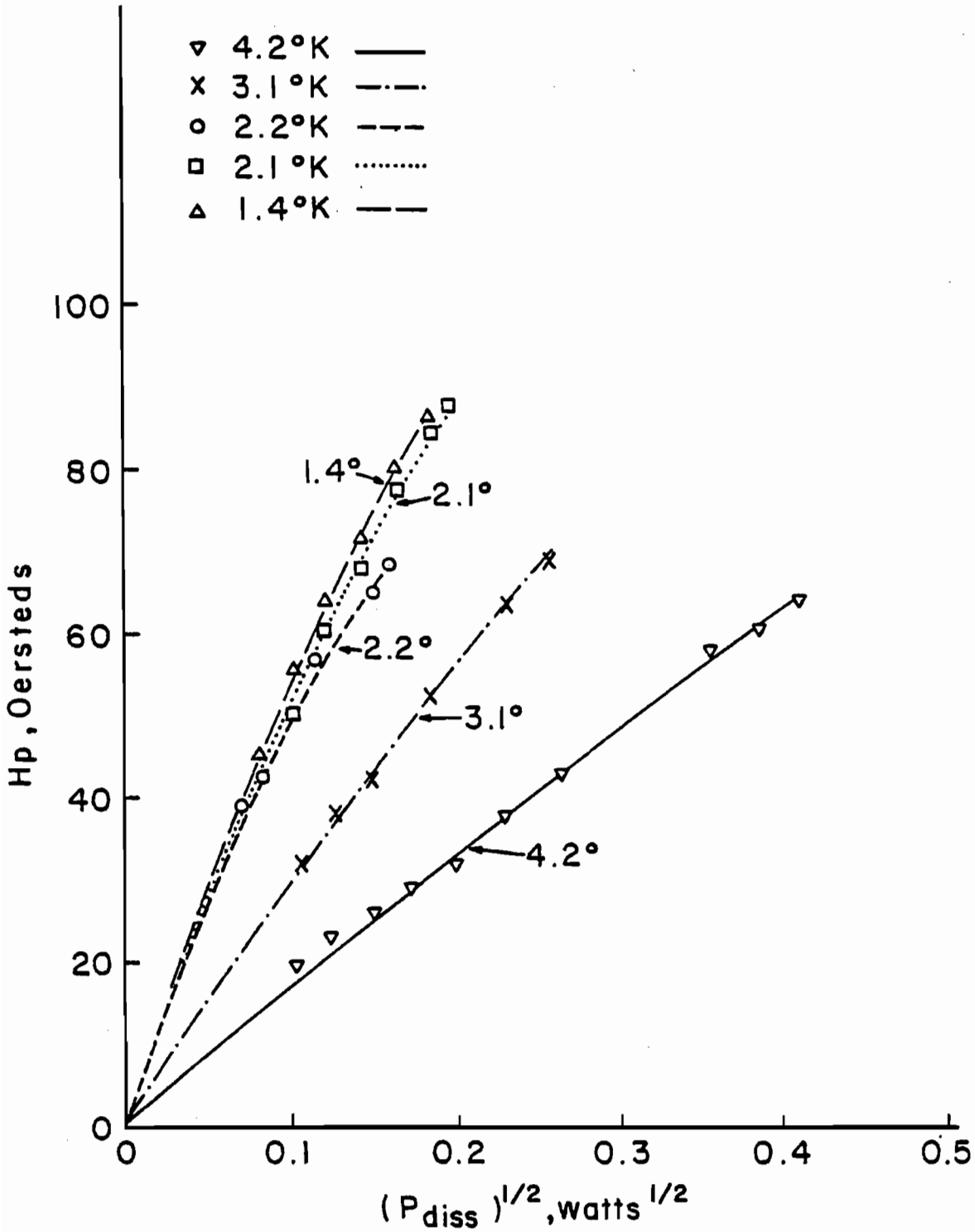

Figure 7.7 Microwave performance of unannealed Nb cavity.

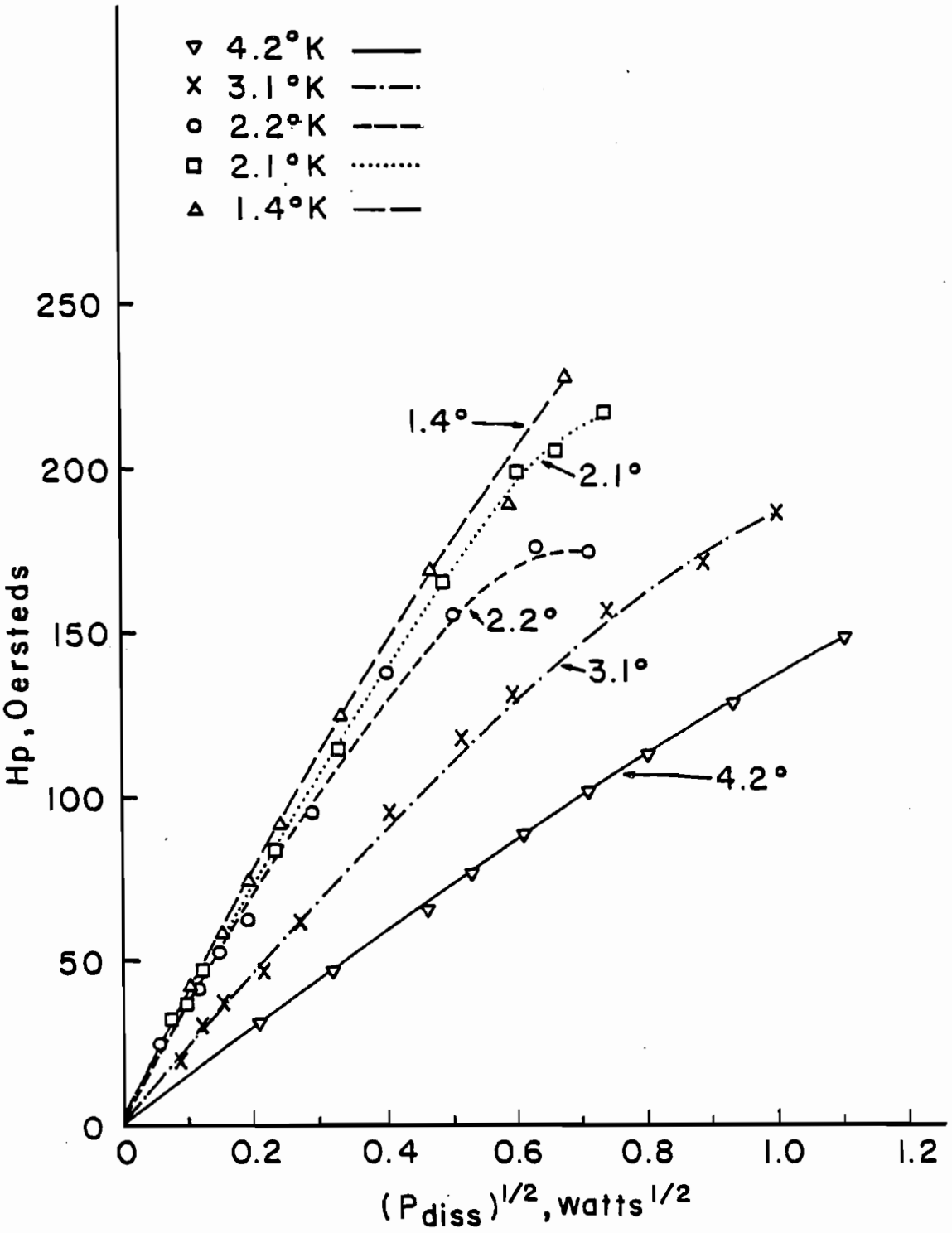

Figure 7.8 Microwave performance of annealed and engassed Nb cavity.

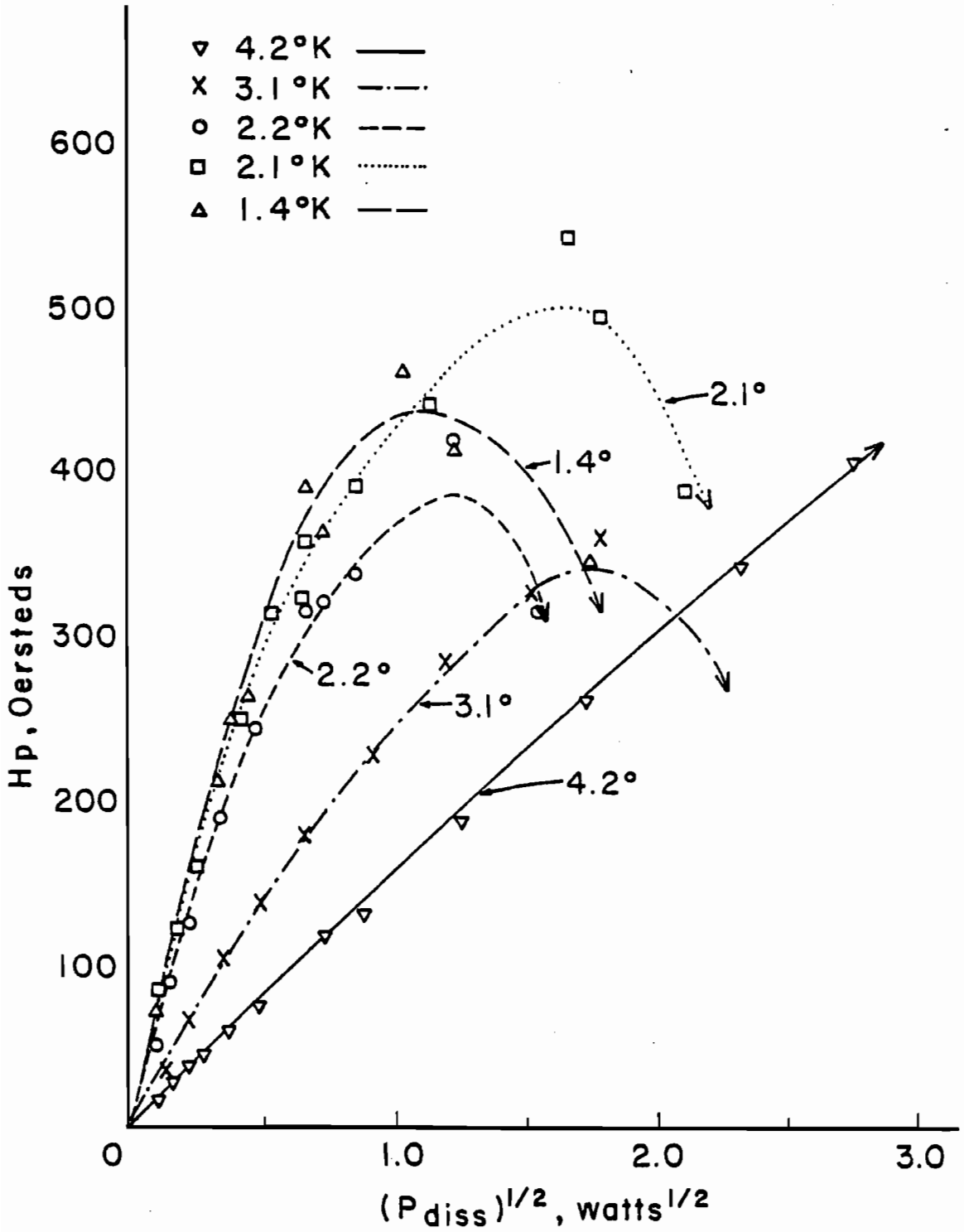

Figure 7.9 Microwave performance of outgassed Nb cavity.

Q_o is related to H_p and P_{diss} by $Q_o^{\frac{1}{2}} = 20.8 \times H_p / P_{diss}^{\frac{1}{2}}$.

The results shown in Figures 7.7-7.9 demonstrate the importance of the thermal conductivity of the Nb to the microwave performance of the cavity: the outgassed Nb cavity supported a magnetic field which was five times higher than that at which the unannealed Nb cavity breaks down; the outgassed Nb cavity also safely dissipated at least 100 times asmuch power as the unannealed Nb cavity. The annealed and engassed Nb cavity performed somewhat better than the unannealed Nb cavity; this was expected since the annealed and engassed Nb had a higher thermal conductivity than the unannealed Nb (refer to Figure 5.7).

The performance of all three types of Nb cavities was affected by the high residual surface resistance of the electrodeposited Nb. Figure 7.10 shows results for the surface resistance of the electrodeposited Nb against $1/T_{bath}$ (the surface resistance is related to Q_o by the geometry factor G; $G = R_{surface} \times Q_o = 233\Omega$ in this case [7.3]). The residual surface resistance was at least a factor of ten higher than that routinely achieved with X-band muffin-tin cavities that were fabricated from stamped sheet metal Nb and electropolished prior to testing [7.4]. Occasionally, the electrodeposited Nb cavies had lower residual surface resistances than those shown in Figure 7.10; however, after the high power measurements (for the outgassed cavities) the residual surface resistance had always increased to the values shown in Figure 7.10. The high residual surface resistance was almost certainly due to the deposition process. The thermometers on the outside of the cavity indicated that nearly every electrodeposited cavity was heating at the same location on the cavity surface during the microwave tests;

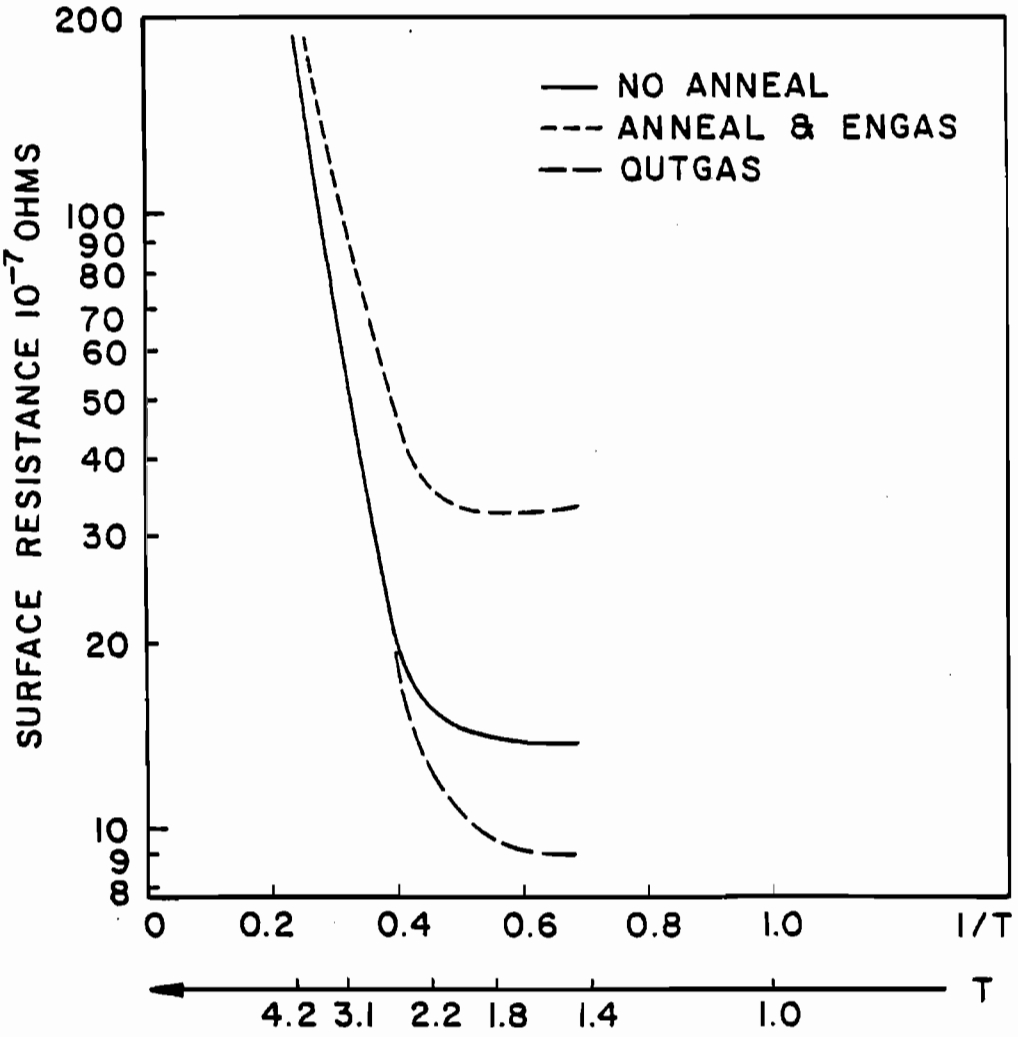

Figure 7.10 Surface resistance of electrodeposited Nb at 8.8 GHz.

this location was the short sidewall that plated most poorly and was pitted on the inside surface (refer to the discussion in Section 5.3). The only cavity that did not exhibit heating at this one short sidewall showed heating at the other short sidewall, which was also a location where the Nb deposition was poor. Clearly, the deposition process needs to be improved in order to improve the quality of the Nb surface and lower the residual surface resistance of the Nb.

Consider first the results expected for the unannealed Nb cavity. The performance of this cavity was expected to be dominated by the low thermal conductivity of the Nb; a large temperature gradient was expected at the location of a defect, leading to breakdown of the cavity; the overall temperature of the cavity was not expected to rise until breakdown occurred. The results shown in Figure 7.7 are consistent with these expectations; the cavity Q_0 remained essentially unchanged as the power dissipated in the cavity was raised to the breakdown level. Furthermore, the cavity could sustain more power at the higher bath temperatures before breaking down; this is consistent with the increase in the thermal conductivity of the unannealed Nb with temperature.

The annealed and engassed Nb cavity exhibited breakdown at higher fields than the unannealed Nb cavity; this was expected since the annealed and engassed Nb should have a higher thermal conductivity than the unannealed Nb. As may be seen in Figure 7.8, the cavity Q_0 decreased when the power dissipated in the cavity increased; this indicates that some non-localized heating was occurring. However, the cavity still exhibited a sharp breakdown as the field level was raised.

The typical performance of the outgassed cavities, shown in Figure

7.9, was quite different from the performance of the low thermal conductivity Nb cavities shown in Figures 7.7 and 7.8. First, the high thermal conductivity Nb cavities sustained much higher fields and dissipated powers than the low thermal conductivity cavities. In addition, the high thermal conductivity cavities did not exhibit breakdown at the power levels available for this experiment. Instead, the curve for H_p as a function of P_{diss} peaked and then fell as P_{diss} was increased; the cavity Q_o fell by up to a factor of ten as P_{diss} was raised to very high values. These results indicate that significant heating of the entire cavity surface was occurring at high powers; as the dissipated power reached very high values the thermal boundary resistance limited the transport of heat to the liquid helium; in particular, at power levels of several watts film boiling may occur and limit the transport of heat to the liquid helium. This heating was also observed experimentally at power levels above the level at which the peak fields were observed: in that case the power emitted by the cavity depended upon the generator on time; as the on time was increased $P_{emitted}$ decreased to some steady-state value. The time scale of this heating was of the same order as the calculated time constant for heat to propagate across the cavity surface; thus as the power dissipated in the cavity built up during the generator on time, the surface temperature and surface resistance rose and hence the field levels fell.

In summary, the high thermal conductivity Nb cavities did not exhibit thermal-magnetic breakdown due to localized heating; instead, their performance appeared to be limited by the thermal boundary resistance between the Nb and the liquid helium.

7.5 Interpretation of Results

The thermal transport processes responsible for the measured microwave performance of the electrodeposited Nb cavities may be examined using the HEAT program as described in Section 2.4. The calculations were performed for two disks, in order to account for the fact that one cavity consists of two halves; the dimensions of the two disks were the same as those shown in Figure 6.4 except for the thickness of the unannealed Nb, which was only 0.0508cm.

The heat source for these calculations was given by $Q/A = \frac{1}{2} \times R_s(T) \times H^2$. The formula used for the surface resistance of Nb was that suggested by P. B. Wilson [7.5], giving

$$R_s(T) = 1.61 \times 10^{-4} \frac{F_n^2}{T} \times \ln\left(\frac{16T}{F_n}\right) \times \exp^{\frac{-17.2}{T}\, g(T)}$$

where F_n is defined as $F_n = f/2.856$ GHz. The formula for $g(T)$ was taken to be that suggested by Sheahen [7.6], giving

$$g(T) = \left(\cos \frac{\pi}{2} \times (T/T_c)^2\right)^{\frac{1}{2}}.$$

This is in good agreement with the results shown in Figure 7.10 for the surface resistance of the electrodeposited Nb. A uniform magnetic field was assumed to be present at the surface of the center portion of the disk; the field was set to zero for $r \geq r^*$ in an attempt to account for the fact that the fields at the cavity surface were not uniform. The radius r^* was chosen by requiring that the calculated value for $H_p/P_{diss}^{\frac{1}{2}}$ agree with the experimental low power results at 4.2K, where the effect of the residual losses upon the dissipated power level was negligible. The radius r^* turned out to be about one half of the radius of the disk.

A defect was located at the center of one of the disks; the product

of the defect resistance and defect area were chosen by requiring that the calculated value for $H_p/P_{diss}^{\frac{1}{2}}$ agree with the experimental low power results at 1.4K, where the losses are dominated by the residual resistance. The size of the defect was generally chosen by having the defect occupy the center element when the disk was divided up into 40 rings for the calculations; however, the power dissipated at the defect would have remained unchanged if the defect resistance had been divided by a factor of four and the defect radius had been doubled, for example.

Finally, the functions used in the HEAT program for the thermal conductivity and thermal boundary resistance had to be chosen. The curves used for the thermal conductivity of each of the three types of electrodeposited Nb used in this investigation were those given in Figure 5.7; the curves were extended to higher temperatures by requiring that they have the same temperature dependence as similar published results, and otherwise be continuous with the results given in Figure 5.7. The functions for the thermal boundary resistance and film boiling limits were determined from the thermal transport measurements, as discussed in Chapter 6.

The HEAT program was used to study the expected microwave performance for each of the three types of cavities. Representative experimental and calculated results for the unannealed Nb cavity are shown in Figure 7.11 for bath temperatures of 4.2K and 2.1K, to demonstrate the results of the calculations both above and below the lambda point. The calculated curves in Figure 7.11 agree quite well with the experimental results at low power levels; however, the calculations indicate that breakdown should occur at peak magnetic

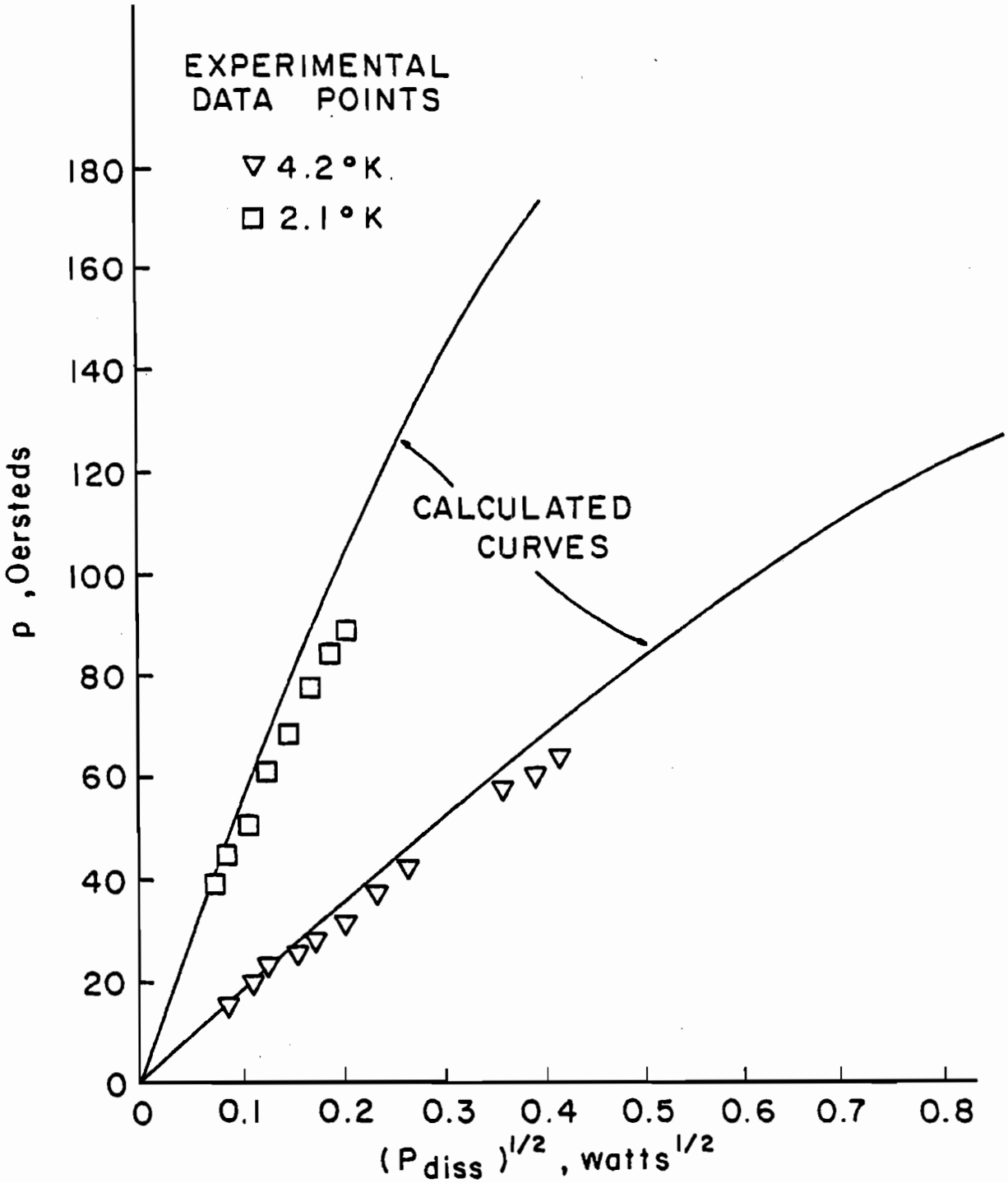

Figure 7.11 Calculated microwave performance for an unannealed Nb cavity.

fields that are about a factor of two higher than those observed experimentally. The calculations do confirm the expectation that thermal transport in the unannealed Nb cavity is governed by its low thermal conductivity and the consequent large temperature gradients near the defect. This is demonstrated in Figure 7.12, where the calculated inside surface temperature profiles are plotted against the distance from the center of the disk for a bath temperature of 2.1K.

The HEAT program was then used to study the effects of varying the size of the defect, the thermal boundary resistance, and the thermal conductivity upon the calculated curves shown in Figure 7.11. The calculated breakdown field level was not very sensitive to the size of the defect if the defect power was kept fixed; decreasing the area of the defect by a factor of four (and increasing its resistance by a factor of four) changed the breakdown field level by less than 10%; the temperature gradient near the defect remained essentially unchanged because the same quantity of heat still had to be conducted away from the defect. The calculated temperature profiles near the defect were not very sensitive to changes in the thermal boundary resistance or film boiling limit; since the power level at which breakdown occurred for this cavity was less than 0.2 watts, the thermal boundary resistance between the cavity and the helium bath was not expected to limit the microwave performance of this unannealed cavity. The calculated breakdown field levels were very sensitive to changes in the thermal conductivity of the Nb; decreasing the thermal conductivity by a factor of two caused the temperature next to the defect to rise by about 50% at a bath temperature of 2.1K; because of the increased temperature gradient near the defect the

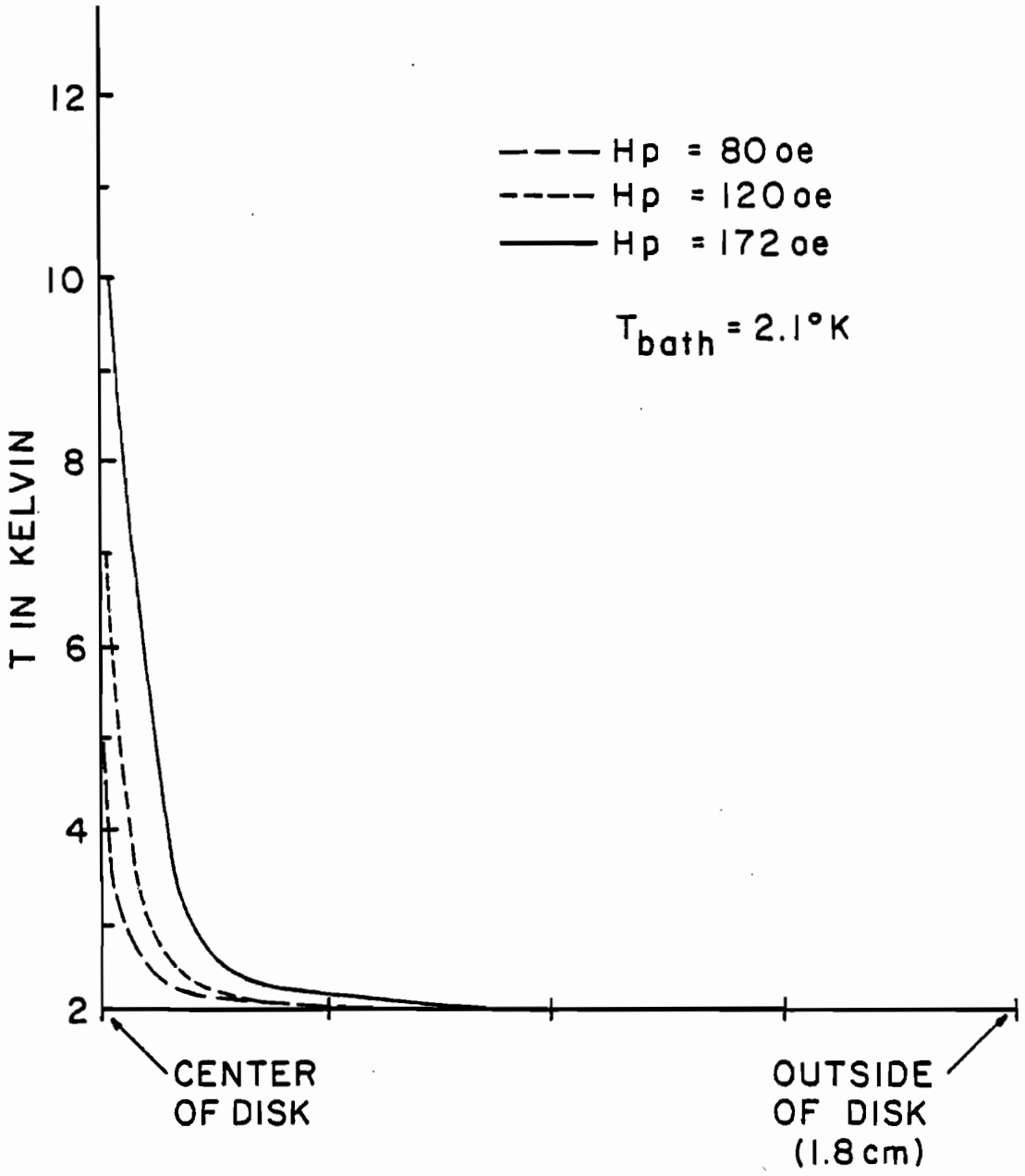

Figure 7.12 Calculated inside surface temperatures for unannealed Nb, as a function of distance from the defect.

surface temperatures more readily reached the regime above about 4K where the thermal conductivity of the Nb was increasing rapidly with increasing temperature; thus the calculated breakdown field level fell by only 25%. The discrepancies between the calculated and measured breakdown field levels are probably caused by incorrect values for the thermal conductivity of the unannealed Nb; since the cavity breakdown occurred at the short sidewall where the deposition was poor and the impurity concentrations were high, it seems probable that the thermal conductivity of the Nb at the breakdown location was lower than that given in Figure 5.7 for a test strip of unannealed Nb. In summary, the low thermal conductivity of the unannealed Nb cavity was the mechanism which limited the microwave performance of the cavity.

Next, the HEAT program was used to study the expected microwave performance for the annealed and engassed Nb cavity. A large temperature gradient was expected near the defect because of the relatively low thermal conductivity of this Nb; thus the function for the thermal conductivity appropriate for use in the calculations was that for the short sidewalls, where breakdown occurred; this function is given in Figure 5.7, for Nb engassed at 1935C in a partial pressure of O_2 of 3×10^{-6} torr. The calculations for the annealed and engassed cavity required a higher resistance defect than for the unannealed cavity because of the low Q_o of this cavity. Representative experimental and calculated results for the annealed and engassed Nb cavity are shown in Figure 7.13. The agreement between the calculations and the experimental data is remarkable. The calculated inside surface temperature profiles for a bath temperature of 2.1K are shown in Figure 7.14; the calculated temperature gradient near the defect is not as sharp for the annealed

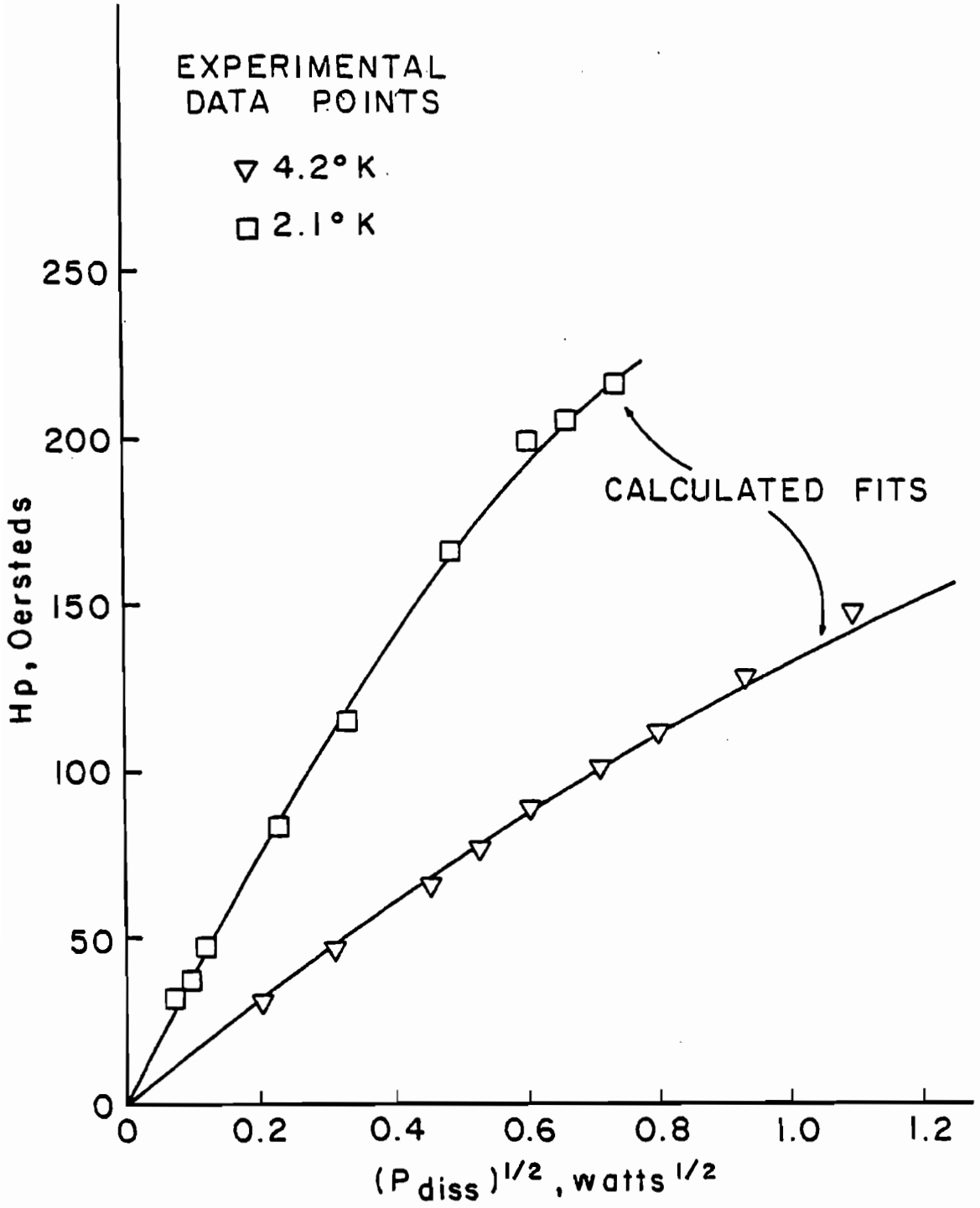

Figure 7.13 Calculated microwave performance for an annealed and engassed cavity.

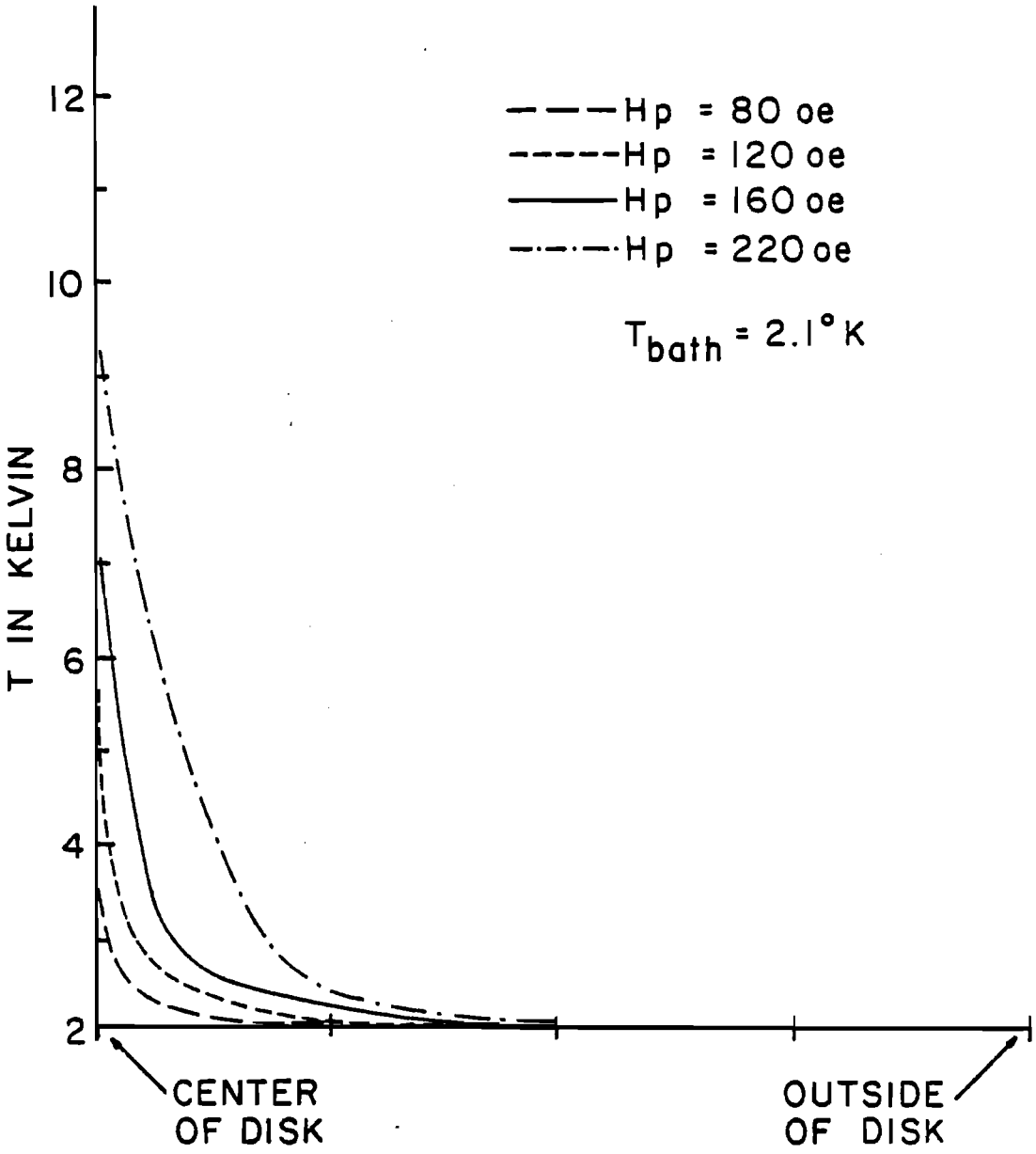

Figure 7.14 Calculated inside surface temperatures for annealed and engassed Nb, as a function of distance from the defect.

and engassed Nb cavity as for the unannealed Nb cavity (shown in Figure 7.12), because the high temperature thermal conductivity of the annealed and engassed Nb is about five times higher than that for the unannealed Nb.

The HEAT program was used to investigate the effects of varying the thermal boundary resistance and thermal conductivity upon the curves shown in Figure 7.13 for the calculated microwave performance of the annealed and engassed Nb cavity. The calculated results were fairly sensitive to changes in the film boiling limit at power levels of 0.5-1.2 watts; for example, at 2.1K and H_p = 220 Oe, doubling the film boiling limit significantly lowered the temperatures near the defect and caused a drop in P_{diss} of 20%. The calculated results were not very sensitive to changes in the function for the thermal boundary resistance. As expected, the calculated results were fairly sensitive to changes in the function used for the thermal conductivity. For example, lowering the thermal conductivity by a factor of two caused the temperature next to the defect to rise by about 50% and the breakdown field level to fall by 20%. The excellent agreement between the calculated and experimental results shown in Figure 7.13 for the annealed and engassed Nb cavity indicates that a good estimate was made for the thermal conductivity of the Nb in the vicinity of the defect. In conclusion, the HEAT program does appear to be quite useful in understanding the microwave performance of low thermal conductivity X-band muffin-tin cavities; when the heating is localized, then treating the cavity as if it were a round disk with a single isolated defect and a uniform magnetic field present at one quarter of its top surface seems to be a reasonable approximation.

The outgassed Nb cavity was found to have an entirely different behavior than either the unannealed Nb cavity or the annealed and engassed Nb cavity; this was expected because the high temperature thermal conductivity of the outgassed Nb was several hundred times higher than that of the unannealed Nb. Representative experimental and calculated results for the outgassed Nb cavity are shown in Figure 7.15. The function for the thermal conductivity used in these calculations was that given in Figure 5.7 for electrodeposited Nb outgassed at 1900C in a vacuum of 1×10^{-9} torr; this function corresponds to the thermal conductivity at the cup-bottom of the cavity and was chosen because the entire cavity surface was expected to heat up at high power levels. The calculated inside surface temperatures for the outgassed Nb cavity at 2.1K are shown in Figure 7.16; Figure 7.16 demonstrates clearly that the entire cavity surface heats up at high power levels.

The HEAT model was not expected to be a very good simulation for the actual case of an outgassed muffin-tin cavity, because the entire cavity surface heats up for the high thermal conductivity Nb: first, the model uses a disk for a cavity instead of a rectangular box with corners; the model also does not account for the variations in thermal conductivity across the surface of the cavity; in addition, the model does not correctly account for variations in the magnetic fields present at the surface of the muffin-tin cavity; finally, the model cannot account for the fact that the defect was located near the edge of the cavity.

In spite of these shortcomings, the HEAT model is useful in understanding the microwave performance of the high thermal conductivity Nb

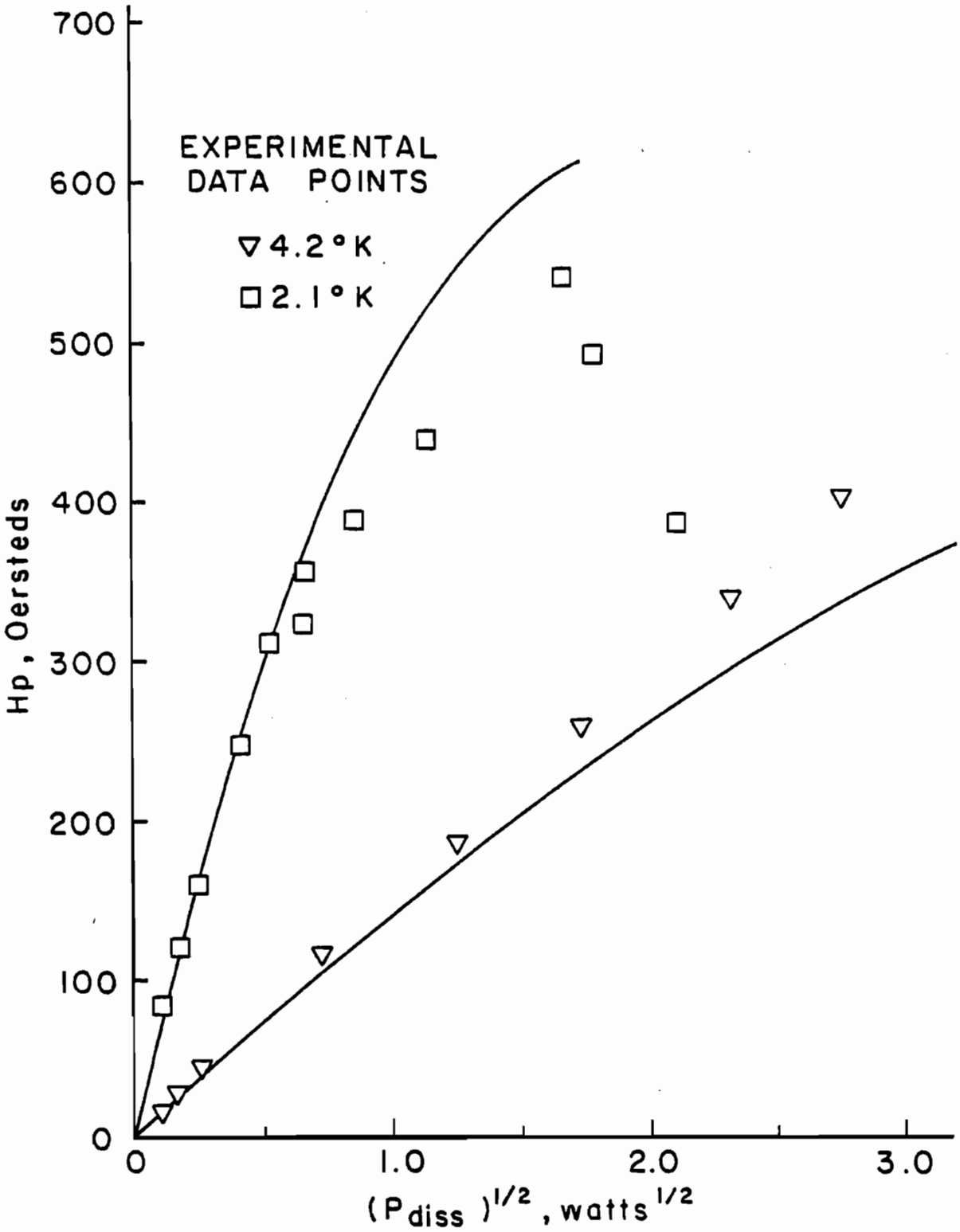

Figure 7.15 Calculated microwave performance for an outgassed Nb cavity.

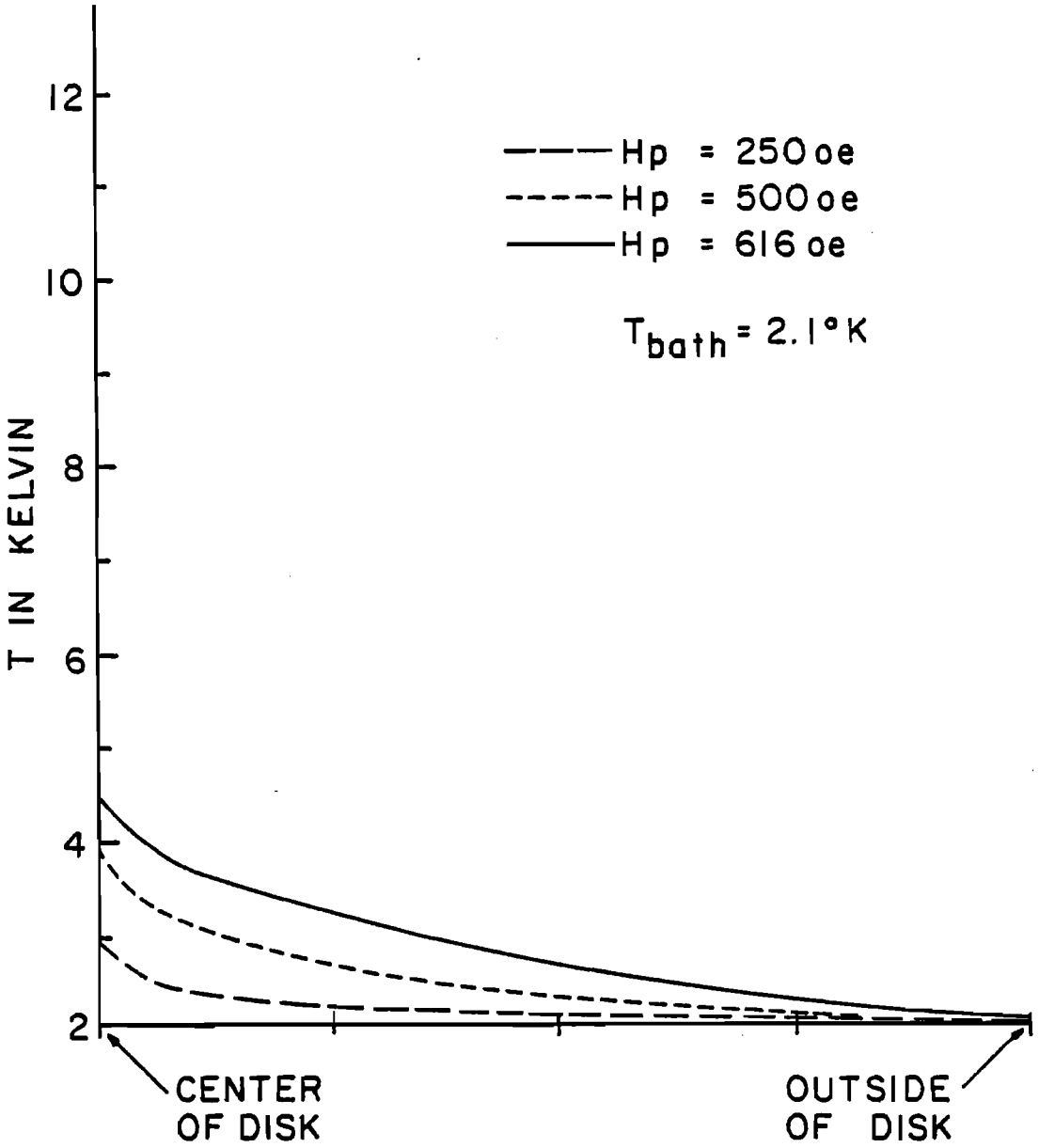

Figure 7.16 Calculated inside surface temperatures for outgassed Nb, as a function of distance from the defect.

cavity. Consider first the calculations for H_o versus $P_{diss}^{\frac{1}{2}}$ shown in Figure 7.15 for a bath temperature of 4.2K; the calculated results lie below the measured results because at high power levels the calculated performance was dominated by film boiling; at 364 Oersteds the calculated surface temperatures ranged from 5.46-4.78K, indicating that localized heating was not responsible for limiting the calculated microwave performance; however at 364 Oe the power dissipated in the disk averaged 0.48 watts/cm^2 which is very close to the film boiling limit used in the calculations; thus the calculations indicate that thermal transport from the Nb to the helium cooling bath is responsible for limiting the cavity performance in liquid He I.

Thermal transport to the helium bath also limits the calculated microwave performance of the outgassed Nb cavity for the case of superfluid He II. The thermal conductivity of the Nb at the lower bath temperatures was not found to significantly affect the calculated results; increasing the thermal conductivity of the Nb by a factor of two increased the maximum magnetic field by about 10% at a helium temperature of 2.1K; the dissipated power at the maximum field level was about the same in each case. The calculated results were not very sensitive to the magnitude of the function for the thermal boundary resistance; decreasing the function by a factor of 1.5 lowered the maximum field level at 2.1K by less than 5%. However, the calculated results were found to be sensitive to the magnitude of the film boiling limit; increasing the film boiling limit from 1 watt/cm^2 to 2 watt/cm^2 raised the maximum field level at 2.1K by over 15%; the dissipated power at the maximum field level increased by a factor of two. The calculations

thus indicate that the microwave performance of the high thermal conductivity Nb cavities is dominated by the thermal boundary resistance between the Nb and the helium cooling bath for superfluid He II as well as for liquid He I.

In conclusion, the HEAT calculations confirm the hypothesis that the performance of superconducting Nb cavities may be considerably improved by the use of high thermal conductivity Nb. The performance of the high thermal conductivity cavities was limited by the transport of heat to the liquid helium, whereas the performance of the low thermal conductivity cavities was limited by the high temperature gradients found at the defect location.

References for Chapter 7

[7.1] S. Ramo, J. R. Whinnery, and T. Van Duzer, Fields and Waves in Communication Electronics, John Wiley and Sons, Inc., NY, 1965.

[7.2] E. L. Ginzton, Microwave Measurements, McGraw-Hill, NY, 1957.

[7.3] H. Padamsee, J. Kirchgessner, M. Tigner, R. Sundelin, M. Banner, J. Stimmell, and H. L. Phillips, Report No. CLNS-340, Laboratory of Nuclear Studies, Cornell University (Aug. 1976).

[7.4] H. Padamsee, M. Banner, J. Kirchgessner, M. Tigner, and R. Sundelin, IEEE Trans. Mag-15, 602 (1979).

[7.5] P. Wilson, Report No. SLAC-TN-70-35, Stanford Linear Accelerator Center, Stanford, California (Dec. 1970).

[7.6] J. P. Sheahen, Phys. Rev. 149, 368 (1966).

Chapter 8

CONCLUSIONS AND SUGGESTIONS FOR FUTURE RESEARCH

The goal of much research into the fundamental properties of superconducting cavities is to routinely achieve surface magnetic fields at the level of the critical fields of the superconductor with low power dissipation in the cavity walls. This systematic investigation of thermal transport in superconducting Nb cavities is therefore of importance because thermal transport processes are a key factor in determining the field and power levels that may be sustained in such a cavity.

This investigation has shown that thermal transport in superconducting cavities is determined by the interplay of the temperature dependent functions for the surface resistance, thermal conductivity, and the metal to liquid helium boundary resistance; values for all three of these functions must be established in order to make predictions about thermal transport in a superconducting cavity.

This investigation has also shown that the use of high thermal conductivity Nb results in substantial improvements in the field levels that may be maintained in X-band muffin-tin Nb cavities; the high thermal conductivity Nb does indeed stabilize the cavity surface against localized heating in the vicinity of an isolated defect. For low thermal conductivity Nb, the analysis performed in Section 7.5 demonstrated that the transport of heat away from the defect limited the fields that could be obtained without breakdown occurring. For high thermal conductivity Nb the analysis performed in Section 7.5 showed that the transport of heat across the Nb to liquid helium interface was crucial in determining the maximum

fields that could be sustained in the cavity.

The ultimate field levels that may be sustained in a cavity may be calculated by assuming that no significant temperature gradients are present within the cavity walls. The surface magnetic field for such a cavity is given by equating $Q/A = \frac{1}{2} \times R_s(T) \times H^2$ to the heat flux across the metal to liquid helium interface. For the cavity system studied here, heat transport to He II was described by the function $Q/A = 0.011 \times (T_s^4 - T_b^4)$ watt/cm^2-K^4. For a defect-free X-band cavity with a uniform surface magnetic field then at T_b = 1.4K the maximum magnetic field is 1050 Oersteds, with a corresponding surface temperature of 1.6K and a heat flux of 0.03 watt/cm^2. In a cavity with non-uniform fields then this calculation shows that the maximum value for $\langle H^2 \rangle$ is (1050 Oersteds)^2; the peak field could easily reach the critical fields of Nb in this case. The peak field increases as T_b is lowered below 1.4K since R_s depends exponentially upon T_s. The peak field in an ideal defect-free cavity also increases as the frequency is lowered; however, at lower frequencies the residual losses become more important and should be included in the calculation. The conclusion to be drawn from these calculations is that the use of high thermal conductivity Nb cavities offers real potential for reaching peak surface magnetic fields at the level of the critical fields of the superconductor with low power dissipation in the cavity walls, provided that the residual losses in the cavity are low.

The use of the electrodeposited Nb was essential in obtaining the high purity and hence high thermal conductivity Nb for this investigation, since the metallic impurity concentrations in commercially available Nb are fairly high. For example, approximately 1000 atomic ppm Ta is found

in commercial Nb; this would limit the thermal conductivity of the Nb after outgassing to about a factor of ten below that achieved in the high thermal conductivity Nb cavities used in this investigation.

A major drawback to the use of the electrodeposited Nb in superconducting cavities appears to be that the poor surface finish leads to high residual losses; the results of this investigation and experiments by Halama [8.1] indicate that the Nb surface is pitted, especially at corners; other experiments with electrodeposited Nb cavities have not given particularly good results [8.2-8.4]. Clearly, experimentation with the electrodeposition process is necessary in order to improve the quality of the cavity surface.

The electrodeposition process is also of interest because large multi-cell structures could be plated without welds in the field region. Currently, the deposition at inside corners is very thin; the deposition at corners would have to be considerably improved in order to successfully plate large structures. Another problem that limits the practical use of electrodeposited Nb cavities is the high cost of the electrodeposited Nb; McAshan, Turneaure and colleagues discontinued their experiments with multi-cell L-band (1.5GHz) and S-band electrodeposited Nb cavities in part because of the high cost of the cavities [8.4].

For the future, further study of the mechanisms involved in thermal transport in superconducting cavities would be possible if defects of known characteristics were located on the cavity surface; for instance, microwave measurements could be made with a cavity that had a small spot of a normal conducting metal evaporated on the cavity surface.

In addition, the HEAT program may be used to study thermal transport

for other cavity systems operating at different frequencies or with different surface properties. Padamsee has used the HEAT program to study thermal-magnetic breakdown in S-band (3GHz) Nb cavities [8.5]; defect heating was very important at 3GHz since the BCS surface resistance scales approximately as ω^2; Padamsee found that the calculated breakdown fields depended strongly upon the defect size and resistance as well as the thermal conductivity of the Nb.

Finally, an understanding of the characteristics of the localized lossy areas or defects is necessary in order to routinely achieve low residual losses in superconducting cavities. Significant lowering of the residual losses has resulted from the use of careful surface treatment and cleanliness during assembly of the cavities. Strongin et al. [8.6] and others have performed investigations of the surface conditions for superconducting Nb cavities; the use of surface physics techniques such as LEED, Auger spectroscopy, Rutherford backscattering, etc., should prove to be useful in further characterizing the nature of lossy regions on the surface of a superconducting cavity.

References for Chapter 8

[8.1] H. J. Halama, IEEE Trans. NS-18, 350 (1971).

[8.2] H. Diepers, B. Hillenbrand, H. Martens, O. Schmidt, K. Schnitzke, Y. Uzel, and K. Wohlleben, Report No. BMBW-FB NT 124, Siemens Aktiengesellschaft (Erlangen, Sept. 1973).

[8.3] R. W. Meyerhoff, J. Appl. Phys. 40, 2011 (1969).

[8.4] M. McAshan and J. P. Turneaure, High Energy Physics Laboratory, Stanford University, private communication.

[8.5] H. Padamsee, Report No. CERN/EF/RF 82-5 (July 1982); also see the proceedings of the Applied Superconductivity Conference (Knoxville, Nov. 1982).

[8.6] M. Strongin, H. H. Farrell, H. J. Halama, O. F. Kammerer, C. Varmazis and J. M. Dickey, Particle Accelerators 3, 209 (1972).

Appendix A

RADIATION SENSITIVITY OF ALLEN-BRADLEY CARBON COMPOSITION RESISTANCE THERMOMETERS

The thermometers used in the thermal conductivity measurements reported in Chapter 5 and the thermal transport measurements reported in Chapter 6 proved to be extremely sensitive to long wavelength blackbody radiation. Stray radiation had been previously observed to affect the value of the measured dc resistance of these thermometers [A.1]. A radiation shield had to be located in both of the experimental apparatus below the liquid helium level; otherwise the radiation down the vacuum pipe from room temperature caused the thermometers to read about 3K above the liquid helium temperature. Furthermore, it proved to be impossible to locate a heater on the inside cavity surface for the thermal transport measurements discussed in Chapter 6; radiation from the heat source caused an apparent temperature rise in the thermometers that overwhelmed the surface temperature rise.

The radiation sensitivity of the thermometers was investigated by placing several of these thermometers inside a vacuum pipe that was then immersed in liquid helium. Variable currents were applied to one of the thermometers in order to heat it up to temperatures between the bath temperature and 300K; by monitoring the voltage across the heater its resistance could be computed; the heater temperature was computed according to the procedure given by Clement, Dolecek, and Logan [A.2] who found that the relationship between the resistance and temperature of carbon composition thermometers was described by one universal scaling function for temperatures from 0.3K to 300K. The apparent

temperatures of the remaining thermometers in the presence of the radiation were measured using the procedure described in Section 5.6. For heater temperature rises of less than 10K the apparent temperature rise of the thermometers varied linearly with the heater temperature. This indicates that the thermometers are sensitive to long wavelength radiation, since the blackbody radiation spectral density is linear in temperature for $\lambda >> hc/kT$ [5.40].

The physical mechanisms responsible for the radiation response of these thermometers are not understood. The response is apparently not caused by a simple rectification process, because the measured resistance of the thermometers was independent of the magnitude and direction of the measuring current. The following discussion demonstrates that the response cannot be explained by Joule heating either. The rise in temperature due to thermometer self-heating of 1×10^{-5} watts was 0.3K, as measured with 100 μA of current through the thermometer. Suppose that ALL of the radiated power from the heater is absorbed by one thermometer. Then the maximum thermometer temperature rise expected from the blackbody radiation is

$$T_{thermometer} - T_{bath} = \frac{0.3K}{1\times10^{-5}\,watts} \times 0.5\,cm^2 \times 0.57\times10^{-11} (T^4_{heater} - T^4_{bath}) \frac{watts}{cm^2\text{-}K^4}$$

$$= 9\times10^{-8} (T^4_{heater} - T^4_{bath}) \frac{watts}{K^4}$$

(using the Stefan-Boltzmann law [5.40] for blackbody radiation for a 0.5 cm^2 source). The thermometer temperature rise calculated from this formula with a heater temperature of 10K is less than 1% of the measured temperature rise. Therefore even if the thermometers absorbed ALL the

radiation their temperature rise cannot be explained in terms of Joule heating. In conclusion, although the thermometers are extremely sensitive to blackbody radiation the physical mechanism by which the radiation is absorbed cannot be simply understood in terms of either rectification or Joule heating.

Experimentally, the radiation sensitivity of the thermometers made it impossible to locate a heater inside the cavity for the thermal transport measurements described in Chapter 6. An example will demonstrate the magnitude of the problem: for a heater power of 10 mW, radiation caused the apparent temperature of the thermometers on the cavity surface to rise by 1.4K; the actual surface temperature rise was found to be 0.016K. Thus the radiation caused an apparent temperature rise in the thermometers of approximately 100 times the effect that was to be measured. Several schemes to shield the thermometers from the heater radiation were inadequate; this is not surprising given that over 99.9% of the radiation had to be blocked in order to achieve a signal to noise ratio of 10:1. Moreover, a design for a "cooler" dc heat source would be very difficult as the heater temperature rise would need to be kept a factor of 1000 times lower than that found for carbon resistors placed in Apiezon N grease.

References for Appendix A

[A.1] E. Ambler and H. Plumb, Rev. Sci. Instr. 31, 656 (1960).

[A.2] J. R. Clement, R. L. Dolecek, and J. K. Logan, Adv. Cryogenic Engineering 2, 104 (1956).

Appendix B

EQUIVALENT CIRCUIT FOR THE TRANSMISSION LINE AND ERROR ANALYSIS

The systematic error in the microwave measurements due to reflections in the transmission line will be discussed in this appendix. General formulas will be derived for the estimated error in terms of the S-parameters of the transmission line; the formulas will be applied to the specific case of the X-band transmission line used for the microwave measurements presented in Chapter 7.

In the center of Figure B.1 the so-called S-parameters, or scattering coefficients, are defined; the S-parameters are frequently used in microwave circuit analysis (see Reference [7.2] for example). The S-parameters for the circuit model shown at the top of Figure B.1 are given in the lower half of Figure B.1. S_{11}, for example, is calculated by solving for V_1/V_0 with $V_7 = 0$.

The reflections in the X-band transmission line (shown in Figures 7.2 and 7.3) may be analyzed in terms of the model shown in the top of Figure B.1. Two possible reflections are included as complex reactances 1/X and 1/Y (both normalized to Z_0); physically, Y results from reflections at the feedthrough; X is included to allow for reflections at any cables or connectors between the feedthrough and the dual directional coupler, where the forward and reflected powers are actually measured. The factors A1F1 and A2F2 account for the attenuation and phase shift for each section of transmission line; the phase shift is given by $\exp(i \cdot \frac{2\pi}{c} f \cdot L)$, where f is the frequency and L is the length of each section of the transmission line.

Equivalent circuit for the transmission line:

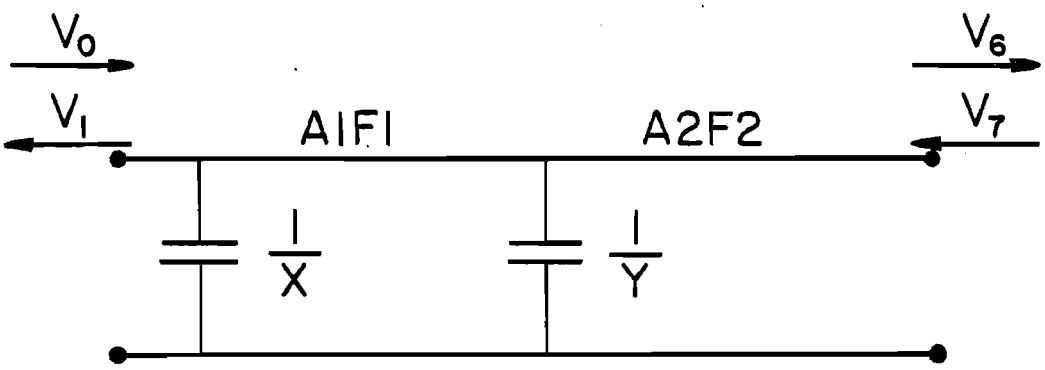

Definition of the S-parameters:

$$\begin{pmatrix} V_1 \\ V_6 \end{pmatrix} = \begin{pmatrix} S_{11} & S_{12} \\ S_{12} & S_{22} \end{pmatrix} \begin{pmatrix} V_0 \\ V_7 \end{pmatrix}$$

S-parameters for the equivalent circuit above:

$$S_{11} = \frac{-2(A1F1)^2Y - X(2 + Y - (A1F1)^2Y)}{2(A1F1)^2Y + (2 + Y - (A1F1)^2Y)\cdot(2 + X)}$$

$$S_{12} = \frac{(A2F2)}{2(A1F1)} \{(2 + X - (A1F1)^2X)S_{11} + (X - (A1F1)^2 X + 2(A1F1)^2\}$$

$$S_{22} = (A2F2)^2 \cdot \frac{\{-(A1F1)^2X - Y(1 + X/2) + (A1F1)^2\cdot Y\cdot X/2\}}{(2 + Y)(1 + X/2) - (A1F1)^2\cdot Y\cdot X/2}$$

Figure B.1 Equivalent circuit and S-parameters for the transmission line.

The parameters X, Y, etc., in the model are chosen to fit the experimental curves for the ratio of reflected to forward power, P_{refl}/P_{inc}, measured at the dual directional coupler when the cavity is off resonance; in terms of the model P_{refl}/P_{inc} is calculated from V_1/V_0 with $V_6 = V_7$. Figure B.2 shows experimental curves (solid lines) for P_{refl}/P_{inc} as well as calculated fits with the model (dashed lines) for three different configurations of the transmission line. The striking differences between the three cases may be understood in terms of the calculatedfits to the curves. Case I (at the top of the figure) was measured with a cable between the feedthrough and the dual directional coupler; the calculated fit was quite good when two reactances were included in the model. Case II was measured without the cable; only one reactance (Y) was necessary to fit the data with the model. The final curve, Case III, was measured after adding a small tuning step in the outer conductor of the transmission line near the feedthrough; the reflection at the feedthrough was considerably reduced between 8.5 and 9.0 GHz. The microwave measurements reported on in this investigation were all conducted between 8.76-8.81 GHz using the transmission line with the tuning step; however, larger reflections in the transmission line were easily produced if any of the connections in the transmission line were loose.

The estimated errors in P_{diss}, Q_o, and E_{acc} due to reflections in the transmission line will be calculated in terms of the S-parameters. The specific case to be considered in this appendix is that in which the coupling was adjusted close to unity; in that case, the measured power levels were described by $P_{inc} \approx P_{emitted}$ and $P_{refl} \approx 0$. All of

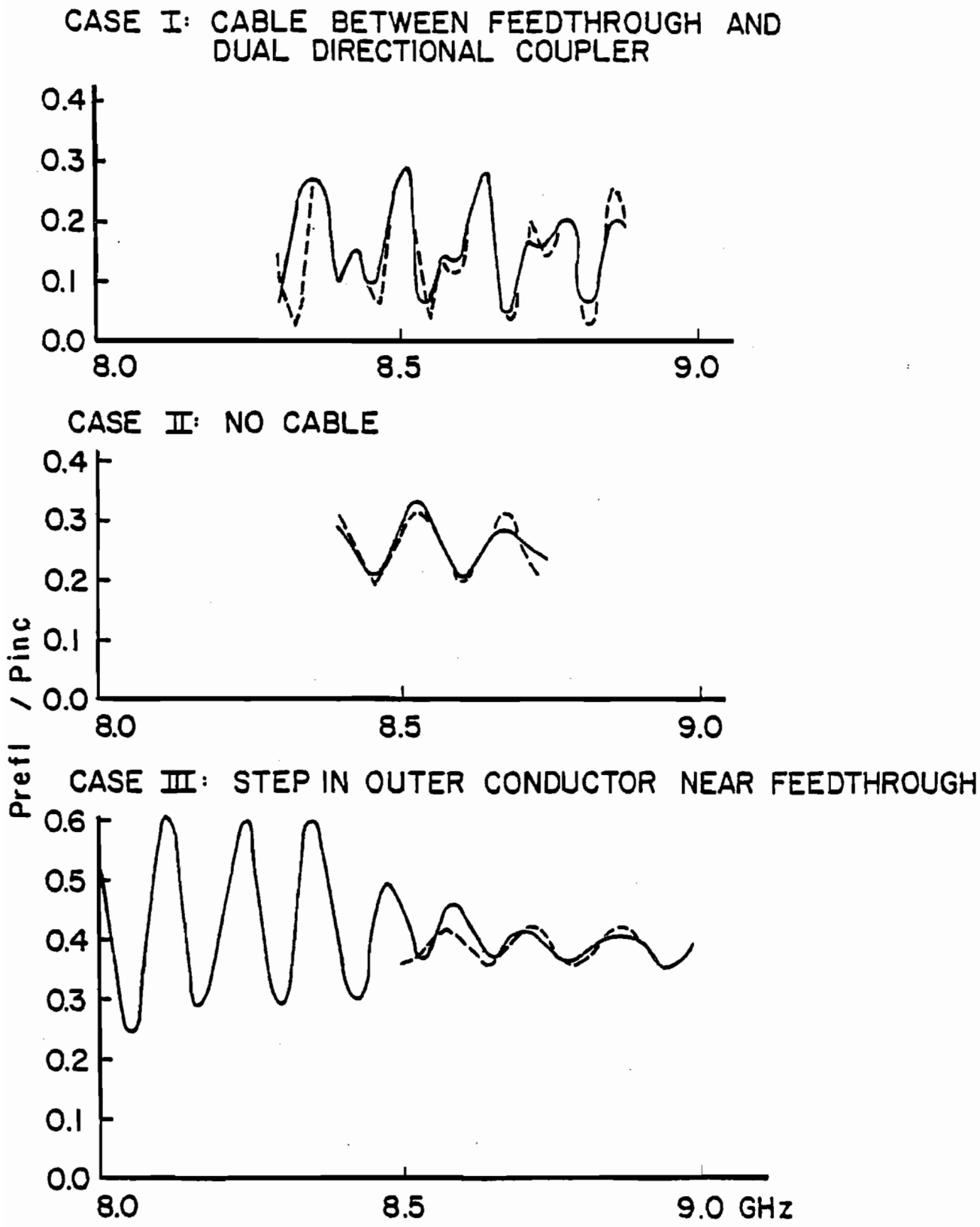

Figure B.2 P_{refl}/P_{inc} at dual directional coupler: —— measured curve, --- calculated fit using equivalent circuit.

these power levels were measured at the top of the transmission line, and were thus affected by the reflections in the transmission line; the correct power levels to use in the formulas for P_{diss}, Q_o, and E_{acc} given in Chapter 7 are those measured at the bottom of the transmission line, before the reflections occur.

First, consider the correction to the calculated value for P_{diss}. The correct dissipated power may be estimated from the model by assuming that P_{refl} is identically zero. With $V_1 = 0$ in Figure B.1 then the power actually dissipated in the cavity is given by

$$\frac{P_{diss}}{P_{inc}} = \left|\frac{V_6}{V_0}\right|^2 - \left|\frac{V_7}{V_0}\right|^2 = \frac{|S_{12}^2 - S_{11}S_{22}|^2 - |S_{11}|^2}{|S_{12}|^2} \quad . \tag{B.1}$$

Furthermore, the coupling constant, defined by (Reference [7.2], Eq. 4.63)

$$\frac{V_7}{V_6} = \frac{Z_c - Z}{Z_c + Z} = \frac{1-\beta}{1+\beta} \quad ,$$

where Z is the impedance of the transmission line, is given by

$$\beta = \frac{S_{12}^2 - S_{11}S_{22} + S_{11}}{S_{12}^2 - S_{11}S_{22} - S_{11}} \quad . \tag{B.2}$$

The power actually emitted by the cavity at the instant the incident power is switched off is calculated by requiring that current be conserved at the coupling port. The current is taken to be

$$I_c = (\text{Re } \beta \cdot P_{diss})^{\frac{1}{2}} \quad .$$

Then

$$P_{emitted} = \left|\frac{V_7}{V_0}\right|^2 - \left|\frac{V_6}{V_0}\right|^2 = \text{Re } \beta \cdot P_{diss} \cdot \frac{1 - |S_{22}|^2}{|1 - S_{22}|^2} \quad , \tag{B.3}$$

where β and P_{diss} are given by Equations (B.1) and (B.2).

Equations (B.1)-(B.3) may also be used to estimate the error in Q_o due to reflections in the transmission line. If the reflections were not present, then the coupling would be given by

$$\beta_{true} = \frac{P_{emitted}(Z_o)}{P_{diss}} ,$$

where $P_{emitted}(Z_o)$ is the power that would be emitted by the cavity into an ideal transmission line; the decay time with an ideal transmission line would be given by

$$\tau_{true} = \frac{U}{P_{diss} + P_{emitted}(Z_o)} ,$$

where U is the stored energy in the cavity. The actual decay time is given by

$$\tau_{actual} = \frac{U}{P_{diss} + P_{emitted}(actual)} .$$

Thus the ratio between the true value of Q_o and the calculated value is

$$\frac{Q_o(true)}{Q_o(calculated)} = \frac{1+\beta_{true}}{1+1} \times \frac{\tau_{true}}{\tau_{actual}} = \frac{1}{2}\left\{1 + \frac{P_{emitted}(actual)}{P_{diss}}\right\} . \quad (B.4)$$

Finally, the estimated error in the calculated electric and magnetic fields may be computed directly from Eq. (B.2)-(B.4) since $E^2 \propto P_{diss} \times Q_o$.

Equations (B.2)-(B.4) may be used to estimate the systematic error in the calculated values for P_{diss}, Q_o, and E_{acc} in terms of the S-parameters for the transmission line. The correction for any particular frequency will not be very reliable for two reasons. First, the accuracy of the S-parameters for the transmission line is limited

by the accuracy of the model; the fits to the measured curves for P_{refl}/P_{inc} in Figure B.2 were respectable but not perfect, indicating that the calculated S-parameters did not include the effects of other reflections in the transmission line. Attempts to actually measure the S-parameters were unsuccessful; the measurements were not reproducible because the X-band transmission line is very sensitive to the minor perturbations that invariably occurred during the course of measuring the S-parameters. The other source of uncertainty in the calculated corrections lies in the fact that several assumptions were made in the course of deriving Eq. (B.2)-(B.4); for instance, Eq. (B.2) for P_{diss} was based upon the assumption that $V_1 \equiv 0$. Although the corrections for any particular frequency are thus in doubt, the range of corrections for different frequencies should provide a good estimate of the overall uncertainty in the calculated values for P_{diss}, Q_o, and E_{acc} due to reflections in the transmission line. Alternatively, this model provides a means to estimate the magnitude of the reflections in the transmission line that may be tolerated to achieve a given level of precision in the results calculated from experimental measurements.

Finally, the corrections for the three cases in Figure B.2 will be presented to illustrate the magnitude of the errors in the measurements due to reflections in the transmission line. Correction factors due to the reflections are defined as follows: first, the correct values for P_{diss}, Q_o, and E_{acc} are computed from Eqs. (B.2)-(B.4) using the same model parameters as those used to generate the curves for P_{refl}/P_{inc} shown in Figure B.2 (dashed lines); these values were then divided by the values computed for a reflection-free transmission line with the

same attenuation (i.e., X = Y = 0 in the latter case). The range of correction factors for each case are included in the following table.

Table B.1 Estimated Correction Factors for the Transmission Line

	Frequency Range	P_{diss}	Q_o	E_{acc}
Case I	8.3-8.9 GHz	0.72-1.01	0.64-1.97	0.68-1.22
Case II	8.4-8.7	0.99	0.89-1.13	0.94-1.06
Case III	8.5-9.0	0.999	0.96-1.04	0.98-1.02

These correction factors demonstrate the importance of minimizing the reflections in the transmission line in order to obtain a reasonable degree of accuracy in the experimental results.